

---

**First Measurement of  
Charged Current Cross Sections  
with Longitudinally  
Polarised Positrons at HERA**

---

Dissertation  
an der Fakultät für Physik  
der Ludwig-Maximilians-Universität München

vergelegt von  
**Ringailė Plačakytė**  
aus Litauen

---

München, den 05. Juli 2006

1. Gutachter: Prof. Dr. Christian Kiesling

2. Gutachter: Prof. Dr. Martin Faessler

Tag der mündlichen Prüfung: 28. September 2006

## Abstract

The analysis presented in this thesis concerns the  $e^+p$  deep inelastic charged current scattering cross sections measured with the H1 detector at HERA. The analysed data were taken in the years 2003-04 at a centre-of-mass energy  $\sqrt{s} = 319 \text{ GeV}$  and comprise two periods of positron beams with positive and negative longitudinal polarisation, corresponding to an integrated luminosity of  $26.9 \text{ pb}^{-1}$  and  $20.7 \text{ pb}^{-1}$ , respectively. The cross sections are measured in a kinematic region of four-momentum transfer squared  $Q^2 \geq 300 \text{ GeV}^2$  and inelasticity  $y \leq 0.9$ .

From the analysed data the polarisation dependence of the total charged current cross section is determined for the first time at high  $Q^2$ . The results are compared with predictions of the Standard Model and found to be in agreement, i.e. possible contributions from non-standard right-handed currents are consistent with zero.

## Kurzfassung

Diese Arbeit beschreibt die Bestimmung der Wirkungsquerschnitte für tiefinelastische Streuung mittels geladener Ströme von Positronen an Protonen mit dem H1 Detektor am Speicherring HERA. Die hier analysierten Daten wurden in den Jahren 2003-04 bei einer Schwerpunktsenergie von  $\sqrt{s} = 319 \text{ GeV}$  aufgenommen. Sie setzen sich aus zwei Perioden mit positiver und negativer longitudinaler Polarisation des Positronenstrahls mit integrierten Luminositäten von  $26.9 \text{ pb}^{-1}$  und  $20.7 \text{ pb}^{-1}$  zusammen. Die Wirkungsquerschnitte wurden in der kinematischen Region  $Q^2 \geq 300 \text{ GeV}^2$  (Quadrat des Viererimpulsübertrags) und  $y \leq 0.9$  (Inelastizität) bestimmt.

Die Abhängigkeit des totalen Wirkungsquerschnitts von der Polarisation wurde erstmalig bei hohem  $Q^2$  gemessen. Die Resultate werden verglichen mit den Vorhersagen des Standardmodells. Sie stimmen mit diesem überein, insbesondere sind die Beiträge von rechthändigen Strömen verträglich mit Null.



# Contents

<b>Introduction</b>	<b>i</b>
<b>1 Theoretical Overview</b>	<b>1</b>
1.1 Deep Inelastic Scattering (DIS) . . . . .	1
1.1.1 Kinematics of DIS Processes . . . . .	2
1.1.2 Basics of the Cross Section Calculations . . . . .	3
1.1.3 Quark Parton Model (QPM) . . . . .	4
1.1.4 Quantum Chromodynamics (QCD) . . . . .	5
1.1.5 Theoretical Aspects of Electroweak Interactions . . . . .	9
1.2 Neutral and Charged Current Cross Sections . . . . .	15
1.2.1 Unpolarised Lepton-Proton DIS Cross Sections . . . . .	15
1.2.2 DIS Cross Sections with Polarised Leptons . . . . .	19
1.2.3 Radiative Corrections . . . . .	19
1.3 Background Processes to Charged Current . . . . .	21
1.3.1 Photoproduction . . . . .	21
1.3.2 Lepton-Pair Production . . . . .	22
1.3.3 W Production . . . . .	23
1.4 Monte Carlo (MC) event generators . . . . .	24
<b>2 The H1 experiment at HERA</b>	<b>27</b>
2.1 HERA Accelerator . . . . .	27
2.1.1 Longitudinal $e$ Beam Polarisation at HERA II . . . . .	30
2.2 H1 Detector . . . . .	36
2.2.1 Tracking System . . . . .	38
2.2.2 Calorimetry . . . . .	40
2.2.3 Luminosity System . . . . .	43
2.2.4 Time of Flight System (ToF) . . . . .	44
2.3 H1 Trigger System . . . . .	44
2.3.1 The First Trigger Level (L1) . . . . .	46
2.3.2 The Second Trigger Level (L2) . . . . .	48
2.3.3 The Third Trigger Level (L3) . . . . .	48
2.3.4 The Fourth/Fifth Trigger Levels (L4/5) . . . . .	48
2.4 Neural Networks for DIS Inclusive Event Triggering . . . . .	49

2.4.1	Introduction to Neural Networks . . . . .	49
2.4.2	H1 Level 2 Neural Network Trigger (L2NN) . . . . .	51
2.4.3	Training of Neural Networks and their Performance . . . . .	53
<b>3</b>	<b>Reconstruction of Kinematic Quantities</b>	<b>59</b>
<b>4</b>	<b>Neutral Current Events for the Charged Current Analysis</b>	<b>63</b>
4.1	Hadronic Energy Calibration . . . . .	64
4.2	Interaction Vertex Reweighting for Simulated Events . . . . .	69
4.3	Pseudo Charged Current Events (PSCC) . . . . .	70
<b>5</b>	<b>Charged Current Data</b>	<b>73</b>
5.1	Charged Current Selection . . . . .	74
5.1.1	Run Selection . . . . .	74
5.1.2	Loose Pre-Selection . . . . .	76
5.1.3	Final Selection . . . . .	77
5.2	Efficiency Estimation Using PSCC Events . . . . .	94
5.2.1	Trigger Efficiency . . . . .	95
5.2.2	Vertex Requirement Efficiency . . . . .	97
5.2.3	$ep$ Background Rejection Efficiency . . . . .	103
5.2.4	Non- $ep$ Background Rejection Efficiency . . . . .	105
5.3	Final Charged Current Event Samples . . . . .	109
<b>6</b>	<b>Charged Current Cross Section Measurement</b>	<b>113</b>
6.1	Definition of $(x, Q^2)$ Bins . . . . .	113
6.2	Cross Section Calculation . . . . .	117
6.3	Systematic Uncertainties . . . . .	118
<b>7</b>	<b>Results</b>	<b>121</b>
7.1	Polarised CC Cross Sections . . . . .	121
7.1.1	Polarisation Dependence of the Total CC Cross Section	122
7.1.2	The $Q^2$ Dependence of the Polarised CC Cross Section	126
7.1.3	The $x$ Dependence of the Polarised CC Cross Section	127
7.1.4	Polarised Double Different Cross Section . . . . .	128
7.2	Unpolarised CC Cross Sections . . . . .	128
7.2.1	The $Q^2$ Dependence of the CC Cross Section . . . . .	130
7.2.2	The $x$ Dependence of the CC Cross Section . . . . .	132
7.2.3	Unpolarised Double Different Cross Section . . . . .	133
<b>8</b>	<b>Summary and Outlook</b>	<b>137</b>
<b>A</b>	<b>Tables of Results</b>	<b>139</b>
<b>B</b>	<b>Kinematic Extrapolation Factors</b>	<b>145</b>

# Introduction

The understanding of the structure of matter, its properties and interactions is one of the fundamental questions in physics and, consequently, a driving force for particle research.

The experiments of particle scattering, where the result of two body interaction is examined, for a long time have been successfully used as a tool to probe the structure of matter. The idea of such experiments was born by the classical Rutherford experiments [1] where a beam of  $\alpha$  particles was fired onto a thin gold foil as target. The observed rare large deflections of the scattered particles served as evidence for the substructure of the gold atoms, leading to the discovery of the atomic nucleus.

There are four known types of interactions in nature, gravitational<sup>1</sup>, electromagnetic, weak and strong. In the first experiments where the *elastic* scattering of the electron on stationary targets was analysed (e.g. Hofstadter [2] in the late 50's), the electromagnetic force was used to measure the charge distributions of the nucleus and of the proton. With the increase of achievable energies for the beam particles the first *inelastic* scattering experiments, with large four-momentum transfer squared  $Q^2$  between the incoming and outgoing electron, became possible. This led to extended studies of the substructure of the proton. In 70's the electron-proton scattering experiments at SLAC (Stanford Linear Accelerator Center) for the first time showed the so-called 'scaling' behavior, i.e. independence of  $Q^2$ , of the proton structure functions [3, 4]. According to Bjorken [5], 'scaling' is expected when the electrons scatter elastically on point-like charged spin 1/2 partons inside the proton, today known as quarks. The Bjorken 'scaling' is a basic idea of the parton model (*Quark Parton Model, QPM*) introduced by Feynman [6] in the 60's. The interactions of quarks are mediated by 'color' field quanta, the gluons, and are described within the framework of the theory of strong interactions (*Quantum Chromodynamics, QCD*).

---

<sup>1</sup>The gravitational force is too weak to notice its influence to elementary particles.

The development of weak interaction phenomenology started in the early 30's with Fermi, who suggested a 4-fermion model for neutron  $\beta$  decay [7]. The great success of the electroweak unification theory developed by Glashow [8], Weinberg [9] and Salam [10] (GWS model) was celebrated in 1983 with the discovery of the predicted heavy  $W^\pm$  and  $Z$  particles in  $p\bar{p}$  experiments at CERN [11, 12].

Quantum Chromodynamics together with the theory of electroweak interactions composes the Standard Model of elementary particle physics.

A unique possibility to explore the structure of the proton and, at the same time to probe the theory of electroweak interactions, has been initiated by the electron<sup>2</sup>-proton collider HERA (Hadron Elektron Ring Anlage) at DESY (Deutsches Elektronen-Synchrotron) in 1992. HERA extended the kinematic regime in  $Q^2$  by more than two orders of magnitude of the one achievable by the experiments which use stationary targets (e.g. SLAC).

The results of HERA physics with data taken until the end of the year 2000 ("HERA I") involve tests of the electro-weak and QCD theories, investigations of perturbative QCD and diffractive scattering, photo-production, QCD analyses of jet and searches for new particles.

The possibility to collide protons with a longitudinally polarised electron beam, as well as a significant increase of the instantaneous luminosity, was provided with the upgrade of HERA in 2003 ("HERA II"). This allows to extend the studies of HERA I for such rare physics processes as charged current interactions ( $e^\pm p \rightarrow (\bar{\nu}) X$ ) and to perform precise tests of the electroweak sector of the Standard Model.

Weak charged current processes with  $W$  exchange measured with the H1 detector at HERA are studied in this thesis. The data taken in 2003-04 with positive and negative longitudinal polarisation for the positron beam are used to measure various cross sections for charged current interactions. The polarisation dependence of the total charged current cross section was measured for the first time at high momentum transfer  $Q^2$ . The results of this thesis have been published [13] in December 2005.

The thesis consists of eight chapters. General theory aspects of Deep Inelastic Scattering are discussed in the first chapter. The HERA  $ep$  collider and the H1 experiment are described next. A short introduction to Neural Networks and their usage for the triggering of inclusive DIS events (e.g. charged currents) which are of particular importance for the HERA II running, are

---

<sup>2</sup>The "electron" here generally refers to electrons and positrons unless explicitly stated otherwise.



also discussed in chapter 2. The reconstruction of the event kinematics is the topic of chapter 3. Relevant aspects of the neutral current measurement ( $e^\pm p \rightarrow e^\pm X$ ) used in the charged current analysis are given in chapter 4. The selection of charged current events and the cross section extraction are topics of chapters 5 and 6. The results of the charged current measurement and the summary are given in chapters 7 and 8.



# Chapter 1

## Theoretical Overview

This analysis concerns the study of the charged current deep inelastic scattering (DIS) processes measured at HERA with the H1 detector. In this chapter the deep inelastic scattering, DIS kinematics and the cross sections of DIS processes are explained. The basic DIS theory aspects, i.e. the quark parton model (QPM), the theory of strong interactions (QCD) and the electroweak sector of the Standard Model are introduced here as well. The exhaustive theory description can be reviewed in other sources like [14].

### 1.1 Deep Inelastic Scattering (DIS)

Deep inelastic scattering (DIS) at HERA is the electron scattering on protons where the electron has sufficient energy to interact with a charged constituent of the proton (quark) and, as a result, a multihadronic final state is produced. There are two deep inelastic electron-proton scattering processes measured at HERA: neutral current (NC),  $ep \rightarrow eX$ , and charged current (CC),  $ep \rightarrow \nu X$ . The exchanged particles between the electron and the quark in neutral current reactions are the photon ( $\gamma$ ) and the boson  $Z$  (Figure 1.1 left). In the charged current scattering process a charged boson  $W^\pm$  is exchanged (Figure 1.1 right). Photons are interacting electromagnetically, the bosons  $Z$  and  $W^\pm$  are mediators of the weak force. The scattered (anti)neutrino ( $\bar{\nu}$ ) in the CC process is not detected and results in an apparent missing transverse momentum. However, the missing transverse momentum can be measured and is a typical signature of charged current reactions.

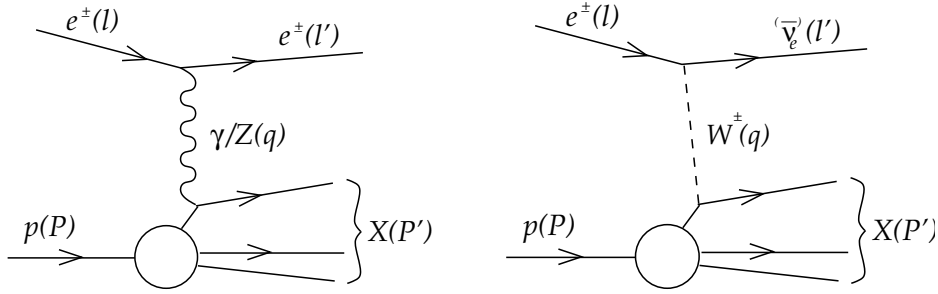


Figure 1.1: *Diagrams of neutral NC (left) and charged CC (right) current deep inelastic scattering processes. The symbols denote the particles, the four-momenta of the particles are given in brackets. The label "X" denotes the hadronic final state.*

### 1.1.1 Kinematics of DIS Processes

The four-vectors of particles involved in the scattering process (see Figure 1.1) are:

- $l$  - the four-vector of incoming electron,
- $P$  - the four-vector of the incoming proton,
- $l'$  - the four-vector of the outgoing electron,
- $P'$  - the four-vector of the hadronic final state  $X$ ,
- $q = l - l'$  is the four-momentum carried by the exchanged boson.

The variables commonly used to determine the DIS kinematics are:

- the four-momentum transfer squared  $q^2$ :

$$q^2 = (l - l')^2$$

$q^2$  is a measure of the virtuality of the exchanged boson, usually used as the positive quantity  $Q^2$ :

$$Q^2 = -q^2 \tag{1.1}$$

- the inelasticity  $y$ , which is the fractional electron energy transfer by the exchanged boson to the proton:

$$y = \frac{P \cdot q}{P \cdot l} \tag{1.2}$$

In the proton rest frame where  $P = (M, 0, 0, 0)$ ,  $y = (E_e - E'_e)/E_e$  as calculated from  $P \cdot q = P(l - l') = M(E_e - E'_e)$  and  $P \cdot l = ME_e$ .

- the Bjorken scaling variable  $x$ :

$$x = \frac{Q^2}{2P \cdot q} \quad (1.3)$$

In the "infinite momentum frame" (where the transverse momentum of the interacting, i.e. struck quark of the proton can be neglected)  $x$  is the (longitudinal) proton momentum fraction carried by the struck quark. This frame represents the basic idea of the *Quark Parton Model* (QPM), i.e. the assumption that the proton is made out of point-like constituents or "partons".

All variables introduced are related with the electron-proton center-of-mass energy squared,  $s = (P + l)^2$ :

$$Q^2 = sxy \quad (1.4)$$

As will be explained later, in QPM the DIS process is viewed as elastic scattering of the electron with a parton, therefore any of two of the variables  $x$ ,  $y$  and  $Q^2$  are sufficient to describe the DIS kinematics at fixed  $ep$  center of mass energy  $\sqrt{s}$ .

### 1.1.2 Basics of the Cross Section Calculations

In QED, the one-photon exchange amplitude is dominating in the lowest-order DIS process. The cross section of inelastic lepton-nucleon scattering thus can be factorised into a leptonic ( $L_{\mu\nu}$ ) and a hadronic ( $W^{\mu\nu}$ ) tensor (see, e.g. [14]):

$$d\sigma \sim L_{\mu\nu} W^{\mu\nu} \quad (1.5)$$

$L_{\mu\nu}$  is well known in QED. It is associated with the coupling of the exchanged photon to the lepton line and depends only on the four-momenta of the incoming and outgoing lepton (see Figure 1.1):

$$L_{\mu\nu} = 2[l_\mu l'_\nu + l_\nu l'_\mu + (q^2/2)g_{\mu\nu}] \quad (1.6)$$

Here,  $g^{\mu\nu}$  is the metric tensor.

The tensor  $W^{\mu\nu}$  describes the nucleon vertex and has the general form

$$W^{\mu\nu} = -W_1 \left( g^{\mu\nu} - \frac{q^\mu q^\nu}{q^2} \right) + \frac{W_2}{M^2} \left( p^\mu - \frac{(P \cdot q)q^\mu}{q^2} \right) \left( p^\nu - \frac{(P \cdot q)q^\nu}{q^2} \right) \quad (1.7)$$

$W_1$  and  $W_2$  represent the structure of the hadron as it is 'seen' by the virtual interacting photon.

In 70's the electron-proton scattering experiments at SLAC (Stanford Linear Accelerator Center) [3, 4] showed that at high  $Q^2$  ( $Q^2 \approx 5 \text{ GeV}^2$ ) the dependence of the inelastic proton functions on  $Q^2$  vanishes and become functions of  $x$  alone. This represents the *scaling behavior* of the proton functions which was successfully explained by Bjorken [5] and lead to the parton model as explained in the next section. Often the functions  $W_1$  and  $W_2$  are expressed in terms of the "structure functions"  $F_1(x)$  and  $F_2(x)$  in the following way:

$$MW_1(x, Q^2) \rightarrow F_1(x) \quad (1.8)$$

$$W_2(x, Q^2) \frac{P \cdot q}{M} \rightarrow F_2(x) \quad (1.9)$$

Assuming that the proton constituents participating in the scattering are spin  $\frac{1}{2}$  particles, Callan and Gross showed [15]:

$$F_2(x) = 2xF_1(x). \quad (1.10)$$

This relation was confirmed experimentally [17] for low values of  $Q^2$  (and  $\sqrt{s}$ ) and reflects the fact that the charged partons inside the proton carry spin  $\frac{1}{2}$ . Using the notations in (1.8) and (1.9), the double differential cross section for inelastic scattering can be expressed as:

$$\frac{d^2\sigma}{dx dQ^2} = \frac{4\pi\alpha^2}{xQ^4} \left[ \frac{y^2}{2} 2xF_1(x) + (1-y)F_2(x) \right] \quad (1.11)$$

With 1.10 one can obtain that the cross section for inelastic scattering (1.11) can be written as:

$$\frac{d^2\sigma}{dx dQ^2} = \frac{2\pi\alpha^2}{xQ^4} \left[ (1 + (1-y)^2) F_2(x) \right] \quad (1.12)$$

where the term  $1 + (1-y)^2$  is called the helicity factor  $Y_+$ .

### 1.1.3 Quark Parton Model (QPM)

The main idea of *Quark Parton Model* is based on *Bjorken scaling* and its interpretation by Feynman [6]: Deep inelastic lepton-proton scattering is the sum of incoherent elastic lepton-parton scattering processes. The corresponding cross section of the whole process is the sum of all lepton-parton cross sections. As discussed in previous section, this scenario predicts scale invariance of the proton structure functions, i.e. their independence on the kinematic scale ( $Q^2$ ).

The assumption that all hadrons consist of quasi-free point-like particles soon was shown to be inconsistent with the lepton and nucleon scattering experiments [17]. According to QPM, the proton is made of two *up* and one *down* quark. The proton structure function  $F_2(x)$  then is written as the sum of the quark distribution functions [16]:

$$F_2(x) = \sum_i e_i^2 x q_i(x) = x \left\{ e_u^2 u(x) + e_d^2 d(x) \right\}$$

Here,  $e_i$  is the charge of the quark  $i$ .

However, it was determined experimentally [17] that the average total momentum carried by quarks inside the proton is:

$$\int_0^1 xu(x)dx + \int_0^1 xd(x)dx \approx 0.36 + 0.18 = 0.54$$

This result clearly suggested that about half of the proton momentum is carried by electrically neutral constituents (the other half is carried by the charged quarks). In addition, the interpretation of quarks as the only proton constituents had to be revised by the experimentally observed *scaling violations*. The scaling violation of the  $F_2$  proton structure function measured experimentally by H1 and some fixed target experiments as function of  $Q^2$  is presented in Figure 1.2.

Nowadays the neutral proton constituents are known as *gluons*. The theory describing the interactions between the proton constituents is called *Quantum Chromodynamics* (QCD). As will be shown in the next section, the scaling violations are explained within the framework of QCD via interactions of the quarks and gluons.

#### 1.1.4 Quantum Chromodynamics (QCD)

Quantum Chromodynamics (QCD) is an important part of the Standard Model which describes the strong interaction, one of the four fundamental forces of nature. It assumes quarks to be elementary fields interacting via massless spin 1 bosons, known as gluons. Gluons carry the quantum number color which has three values (*red, blue, green*) and is described by  $SU(3)_C$ . Quarks do not exist free but are bound in color-singlets (quark-antiquark pairs, mesons, and three-quark states, baryons) states (**confinement**).

Interactions between quarks and gluons in QCD are described by relativistic quantum field theory with a non-Abelian gauge group  $SU(3)_C$ . This means, that the gluons themselves carry color charge, i.e. are self-interacting. QCD thus has an important difference compared to quantum electrodynamics (QED) where photons are electrically neutral and do not self-interact.

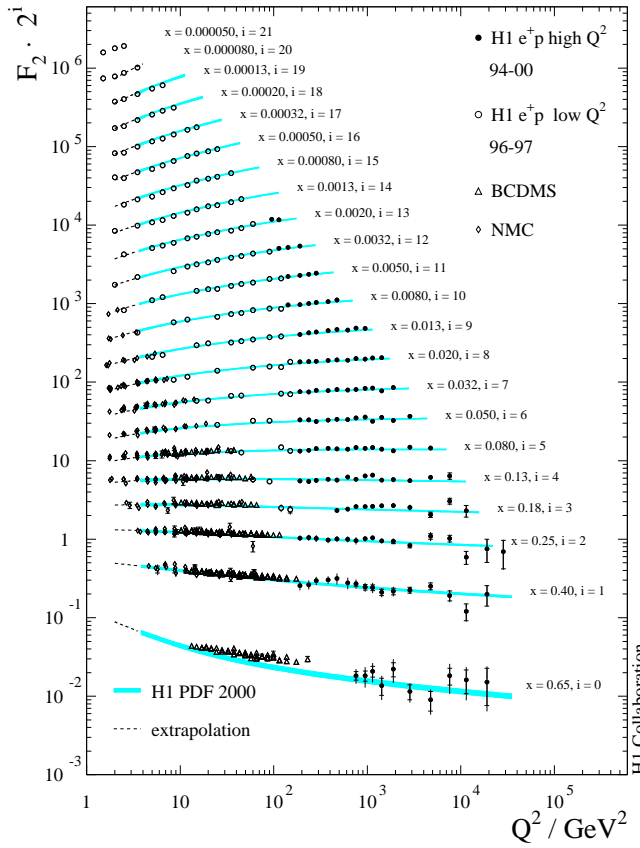


Figure 1.2: Structure function  $F_2$  as function of  $Q^2$  for different  $x$  regions. The points represent H1 measurements which are compared with the H1 fit for the proton density functions [18] (band). The measurements of two fixed target experiments (BCDMC [19] and NMC [20]) are also included in the graph.

## Renormalisation and the running strong coupling constant

In QED, the effective electromagnetic coupling constant  $\alpha$  depends on the momentum transfer  $Q^2$  carried by the mediating photon and increases with the increase of  $Q^2$ . This is a consequence of "vacuum polarisation", where virtual  $e^+e^-$  pairs partially screen the charge, similar to a dielectric medium which screens the electric charge.

In analogy to QED, the coupling strength  $\alpha_s$  in QCD depends on  $Q^2$  carried by the mediating boson. The leading order graph in QCD of the gluon line corrected to vacuum polarisation (Figure 1.3 (a)) represents this idea where the quark-antiquark loop leads to a screening of the color charge. The unique gluon self coupling results from the virtual gluon loop as shown in



Figure 1.3 (b). It has been shown [21, 22], that gluon loops work as "anti-screening": With the increase of  $Q^2$  the second term "overcomes" the color screening and results in a *decrease* of the coupling constant with increasing of  $Q^2$  ("running strong coupling constant"). This is the origin of **asymptotic freedom**.

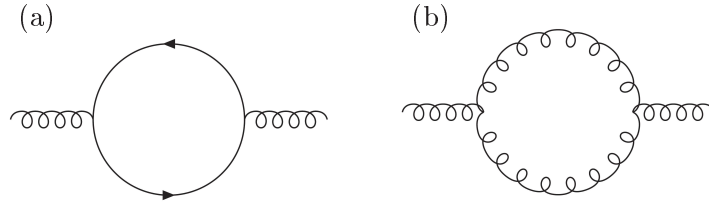


Figure 1.3: Contribution of the  $q\bar{q}$  loop to vacuum polarisation (a), gluon loop contribution to vacuum polarisation (b).

The running of the coupling constant  $\alpha_s$  between a reference scale  $\mu$  and a given  $Q^2$  can be written [14] as:

$$\alpha_s(Q^2) = \alpha_s(\mu^2) \left[ 1 - \frac{\alpha_s(\mu^2)}{12\pi} (33 - 2f) \ln \left( \frac{Q^2}{\mu^2} \right) + \dots \right] \quad (1.13)$$

Here, the number 33 arises from the gluon loop,  $f$  is the number of quark flavours and  $-2f$  is the contribution from the quark pair loops. From the equation 1.13 it can be seen, that the running of  $\alpha_s$  depends on the number of quark flavours  $f$ , i.e. as long as  $f \leq 16$   $\alpha_s$  will decrease with increasing  $Q^2$ . Since the known number of quark flavours is 6,  $\alpha_s$  is expected to fall with the increase of  $Q^2$ .

At sufficiently low  $Q^2$ , the effective coupling will become large. It is customary to denote the  $Q^2$  scale at which this happens by  $\Lambda_{QCD}^2$ . The strong coupling  $\alpha_s(Q^2)$  can be written as:

$$\alpha_s(Q^2) = \frac{12\pi}{(33 - 2f) \ln(Q^2/\Lambda_{QCD}^2)} \quad (1.14)$$

For 6 quark flavours  $\Lambda_{QCD}$  is approximately equal to 300-500 MeV.

At large energy scales (equivalent to large  $Q^2$ ) where the distance between the partons are small owing to the uncertainty principle,  $\alpha_s$  becomes small and the partons can move "freely" inside the proton. This property is called **asymptotic freedom**. Similarly, at small  $Q^2$ , i.e. large distances, the coupling between the partons increases and results in **confinement**, where quarks and gluons are bound in hadronic states.

### Factorisation

Applications of QCD as discussed up to now, are limited to the *short-distance* region (perturbative QCD or pQCD<sup>1</sup>). Due to higher order corrections at *long range* (**infrared divergences**, i.e. radiation of soft gluons off partons, for example) it is impossible to calculate DIS cross section. The **factorisation theorem** factorises the cross section into a "short distance" component (i.e. elastic electron-parton scattering), which is calculable within pQCD, and a non-perturbative "long distance" component (parton distributions), which has to be determined experimentally. As a result, the inclusive lepton-proton DIS cross section is calculable in pQCD with empirically parameterised parton densities (at a given reference scale) inside the proton. The parton densities are called *parton distribution functions* (PDF).

Although the parton distribution functions cannot be calculated, their  $Q^2$  dependence is calculable in pQCD as described by the DGLAP (Dokshitzer-Gribov-Lipatov-Altarelli-Parisi) evolution equations [23]:

$$\frac{\partial q(x, t)}{\partial t} = \frac{\alpha(t)}{2\pi} \int_x^1 \frac{dy}{y} \left[ q(y, t) P_{qq} \left( \frac{x}{y} \right) + g(y, t) P_{qg} \left( \frac{x}{y} \right) \right] \quad (1.15)$$

$$\frac{\partial g(x, t)}{\partial t} = \frac{\alpha(t)}{2\pi} \int_x^1 \frac{dy}{y} \left[ q(y, t) P_{gq} \left( \frac{x}{y} \right) + g(y, t) P_{gg} \left( \frac{x}{y} \right) \right] \quad (1.16)$$

Here,  $t = \ln(Q^2/\Lambda_{QCD}^2)$ ,  $P_{ij}$  are the so-called *splitting functions*.  $P_{ij}$  describe the probability of parton  $j$  with momentum fraction  $y$  to produce a parton  $i$  with momentum fraction  $x$ , when the  $Q^2$  scale changes from  $Q^2$  to  $Q^2 + dQ^2$ . Figure 1.4 shows four Feynman diagrams for each of these elementary processes.

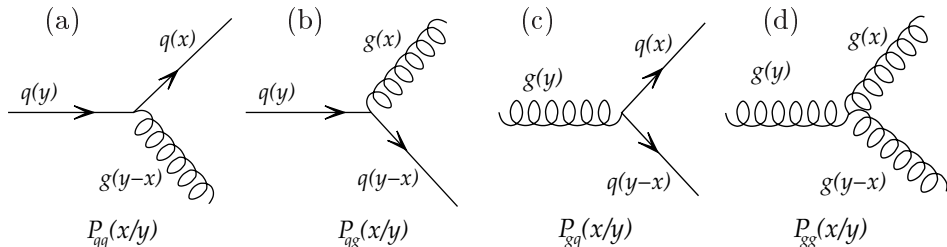


Figure 1.4: *Feynman diagrams for each of the four splitting functions  $P_{ij}$  and the corresponding elementary processes: (a)-(b) gluon emission by a quark, (c) quark-antiquark creation, (d) gluon emission by a gluon.*

<sup>1</sup>Perturbative QCD is the study of the theory of QCD in energy regimes where the strong coupling constant  $\alpha_s$  is small, allowing perturbation theory to be applied.

The electron-proton scattering process can be viewed as an interaction where the electron acts as a source of virtual photons, i.e.  $\gamma^* p \rightarrow X$ . The exchanged virtual photon ( $q^2 \neq 0$ ) can be either transversely or longitudinally polarised. In the QPM model, due to conservation of the helicity and angular momentum, the interaction of an electron and a longitudinally polarised virtual photon is not possible. In QCD, due to additional particles at the hadronic vertex (the quark can radiate a gluon or a gluon can split into a quark-antiquark pair, as shown in Figure 1.4), there is no longer difficulty to conserve the helicity and angular momentum with a longitudinally polarised virtual photon. The Callan-Gross relation (1.10) is no longer valid and the difference of the two structure functions  $F_2(x)$  and  $F_1(x)$  is connected to a non-zero longitudinal structure function  $F_L$ :

$$F_L(x) = F_2(x) - 2xF_1(x) \quad (1.17)$$

In QPM, the longitudinal structure function  $F_L = 0$ .

### 1.1.5 Theoretical Aspects of Electroweak Interactions

First attempts to understand weak interactions started in 1933 when Fermi formulated the 4-fermion model to describe the neutron  $\beta$  decay:

$$n \rightarrow p + e^- + \bar{\nu}_e$$

Fermi proposed a point interaction Lagrangian as follows:

$$\mathcal{L}_F = \frac{G_F}{\sqrt{2}} J_\mu(np) J^\mu(e\bar{\nu}) = \frac{G_F}{\sqrt{2}} [\bar{\psi}(p)\gamma_\mu\psi(n)] [\bar{\psi}(e)\gamma^\mu\psi(\bar{\nu})] \quad (1.18)$$

where the first current is associated with the transition of  $n$  to  $p$  (hadronic current), the second term corresponds to the  $(e\bar{\nu})$  pair (leptonic current). These currents are coupled with the coupling constant  $G_F$  ("Fermi constant") which is equal to  $1.16 \cdot 10^{-5} \text{ GeV}^2$  [24].

However, the violation of parity (non-invariance of interactions under space coordinate inversion, or mirror reflection) which nowadays is a well known property of the weak interactions, was clearly not built into Fermi's vector-vector theory. An example of a quantity illustrating parity violation (changing sign under space coordinate inversion) is *helicity*. Helicity is a projection of particle's spin along its direction of motion, as shown in Figure 1.5.

The violation of parity was initially proposed by T.D. Lee and C.N. Yang (1956) [26] in  $K$  meson decay (then known as the  $\theta - \tau$  puzzle). One year later parity violation was established in nuclear  $\beta$  decay (Wu [27]).



Figure 1.5: *Schematic presentation of different helicity states. Helicity is the projection of the particle spin to the direction of motion:  $h = \vec{s} \cdot \vec{p} / |\vec{s} \cdot \vec{p}|$ . For spin  $\frac{1}{2}$  particles helicity can either be positive ( $+\frac{\hbar}{2}$ ) - the particle is then "right-handed" (right), or negative ( $-\frac{\hbar}{2}$ ) - the particle is then "left-handed" (left).*

A generalisation of the Fermi's vector theory to include parity violation was independently proposed in 1958 by Feynman and Gell-Mann [28] and Sudarshan and Marshak [29]. They suggested a  $(V - A)$  Lagrangian for weak interactions. The notation  $(V - A)$  means that both vector and axial vector parts are contained in the weak current  $J_\mu$ . The purely left-handed nature of the neutrino, violating parity in a maximal way, is introduced by the  $\frac{1}{2}(1 - \gamma_5)$  operator. Thus the expression for the hadronic weak current at the quark level is

$$J_\mu(h) = \bar{u}\gamma_\mu \frac{1 - \gamma_5}{2} d_C + \dots \quad (1.19)$$

Here, the factor  $\gamma_\mu$  yields a vector coupling whereas  $\gamma_\mu\gamma_5$  gives the axial vector,  $\bar{u}$  is the Dirac spinor of the  $u$  quark, and  $d_C$  is the Cabibbo-rotated quark field with charge  $-1/3$  introduced by Cabibbo [30] in 1963: When the quarks are grouped into families (according to their charges and masses), the quark transitions in the weak decays (e.g.  $d \rightarrow u$  in neutron  $\beta$  decay) are occurring not only within a family, but (to lesser degree) from one family to another. The weak force thus couples not to the quark pairs but rather to linear combinations of the physical quarks, written as the sine and cosine of the so-called Cabibbo angle  $\theta_C$ :

$$d_C = d \cos \theta_C + s \sin \theta_C \quad (1.20)$$

The two component quark spinor with incorporated Cabibbo structure of the charged currents usually is denoted as:

$$q = \begin{pmatrix} u \\ d_C \end{pmatrix}_L$$

The symbol  $L$  indicates that only the left-handed parts of the wave functions enter into the weak transitions.

All three generations of quarks known today can be expressed via the  $3 \times 3$  *Cabibbo-Kobayashi-Maskawa matrix* [16] which is an extension of the original Cabibbo matrix, formulated by Kobayashi and Maskawa in 1973:

$$\begin{pmatrix} d' \\ s' \\ b' \end{pmatrix} = \begin{pmatrix} U_{ud} & U_{us} & U_{ub} \\ U_{cd} & U_{cs} & U_{cb} \\ U_{td} & U_{ts} & U_{tb} \end{pmatrix} \begin{pmatrix} d \\ s \\ b \end{pmatrix} \quad (1.21)$$

The probability for a transition of a quark  $q$  to a quark  $q'$  is proportional to the square of the magnitude of the matrix element  $|U_{qq'}|^2$ .

The combined Feynman, Gell-Mann and Cabibbo theories showed a good description of the experimentally measured charged-current interactions within first-order perturbation theory. However, at energies of order  $1/\sqrt{G_F}$  (corresponding to  $\approx 300 \text{ GeV}$ ) violation of the unitarity, i.e. conservation of probability, is encountered.

Unitarity was saved (in lowest order) by introducing a new field quantum, the intermediate vector boson  $W$ . In contrast to the electromagnetic field quantum (photon),  $W$  has to be charged as the weak currents involve a change of charge (by one unit) and also has to be massive (according to the Yukawa-Wick argument [33] that the range of a force is inversely proportional to the mass of the exchanged field quantum). In the approximation of  $Q^2 \ll M_W^2$  (here  $M_W$  is the mass of the  $W$ ), the coupling strength  $G_F$  is proportional to the weak couplings constant  $g$ :

$$\frac{G_F}{\sqrt{2}} = \frac{g^2}{8M_W^2} \quad (1.22)$$

However, even with  $W$  exchange it can be shown that unitarity in weak interactions is not saved at higher orders: The theory turned out as non-renormalisable (due to the non-vanishing mass of  $W$ ).

Developing the theory of weak interactions, in 1958 Bludman [34] suggested the existence of *neutral weak interactions* with a chargeless mediator, nowadays known as the  $Z$  boson. The first experimental evidence of the neutral weak interactions was revealed in 1973 at CERN [35].

The properties of the  $Z$  boson are described in the framework of *electroweak interaction*, established by Glashow in 1961, Weinberg in 1967 and Salam in 1968 (GWS model) where the electromagnetic and weak interactions are understood as two aspects of the same interaction. The theory incorporates a new quantum number, *weak isospin*  $I$ , in analogy to isospin of the strong interactions. As discussed above, each family of quarks (and leptons) form so-called weak doublets of left-handed fermions which can transform into each other by the exchange of a  $W$ . The electric charge  $e_f$  of the fermions in the same family differs by one unit. Being a doublet, the weak isospin is  $I = 1/2$  and the third component is  $I_3 = \pm 1/2$ . The right-handed fermions do not couple to the  $W$  and are described as singlets with  $I = I_3 = 0$ . The whole list of weak multiplets of fermions is given in Table 1.1.

leptons					
$\begin{pmatrix} \nu_e \\ e \end{pmatrix}_L, \begin{pmatrix} \nu_\mu \\ \mu \end{pmatrix}_L, \begin{pmatrix} \nu_\tau \\ \tau \end{pmatrix}_L$	$e_f = \begin{cases} 0 \\ -1 \end{cases}$	$I = \frac{1}{2}$	$I_3 = \begin{cases} +\frac{1}{2} \\ -\frac{1}{2} \end{cases}$		
$e_R, \mu_R, \tau_R$	$e_f = -1$	$I = 0$	$I_3 = 0$		
quarks					
$\begin{pmatrix} u \\ d' \end{pmatrix}_L, \begin{pmatrix} c \\ s' \end{pmatrix}_L, \begin{pmatrix} t \\ b' \end{pmatrix}_L$	$e_f = \begin{cases} +\frac{2}{3} \\ -\frac{1}{3} \end{cases}$	$I = \frac{1}{2}$	$I_3 = \begin{cases} +\frac{1}{2} \\ -\frac{1}{2} \end{cases}$		
$u_R, c_R, t_R$	$e_f = +2/3$	$I = 0$	$I_3 = 0$		
$d_R, s_R, b_R$	$e_f = -1/3$	$I = 0$	$I_3 = 0$		

Table 1.1: Weak multiplets of leptons and quarks.  $e_f$  is the electric charge,  $I$  is the weak isospin, and  $I_3$  its third component.

Conservation of  $I$  in weak reactions requires three states of  $I_3$  ( $-1, 0, +1$ ), i.e. three bosons. These states could be assigned to  $W^+$ ,  $W^-$  and a third neutral field quantum  $W^0$ , also with a purely left-handed coupling. In addition, one could postulate a state  $B^0$ , a singlet of the weak isospin  $I = I_3 = 0$ . Its coupling strength ( $g'$ ) to the weak neutral current does not have to be equal of the one for  $W^\pm$  and  $W^0$  ( $g$ ). The new fields  $B^0$  and  $W^0$  were assumed to carry mass.

Electroweak unification was suggested by Glashow, introducing the weak analog to hypercharge<sup>2</sup>  $Y_W$ , using the Gell-Mann-Nishijima formula [14]:

$$e_f = I_3 + \frac{1}{2}Y_W \quad (1.23)$$

Here, the electric charge  $e_f$  is in units of  $e$ . The lepton doublets in this case have  $Y_W = -1$  while quark doublets have  $Y_W = +1/3$ .

The basic idea of the *electroweak unification* is to describe the neutral current mediators (photon and a hypothetical  $Z$ ) as linear combinations of  $B^0$  and  $W^0$  such that one state, the photon, remains massless. This mixing is expressed as a rotation through the weak mixing angle, or *Weinberg angle*<sup>3</sup>,  $\theta_W$ :

<sup>2</sup>Hypercharge  $Y = B + S$  where  $B$  is the baryon number and  $S$  is the strangeness.

<sup>3</sup>There is no theoretical prediction for  $\theta_W$ . Therefore its value has to be determined experimentally. The present best estimate of  $\sin^2 \theta_W$  in the  $\overline{MS}$  scheme is 0.2312 [24].

$$|\gamma\rangle = \sin\theta_W|W^0\rangle + \cos\theta_W|B^0\rangle \quad (1.24)$$

$$|Z\rangle = \cos\theta_W|W^0\rangle - \sin\theta_W|B^0\rangle \quad (1.25)$$

The relation between the Weinberg angle  $\theta_W$  and the weak couplings  $g, g'$ :

$$\tan\theta_W = \frac{g'}{g}. \quad (1.26)$$

Unification is explicitly expressed by relating the weak coupling  $g$  with the electric charge  $e$ :

$$g \sin\theta_W = e \quad (1.27)$$

The combination of a new Abelian group  $U(1)$  associated with "weak hypercharge" and the  $SU(2)$  group associated with "weak isospin" resulted into the  $SU(2)\times U(1)$  group of electroweak interactions. Thus the unification of the weak and electromagnetic forces was established. However, the masses of the weak bosons  $W^\pm$  and  $Z$  still have to be accommodated within the theory.

The  $W$  boson couples to left-handed leptons and quarks with equal strength, irrespective of their charge. In the coupling of  $Z$  the electric charges play a role as well. The coupling strength of  $Z$  to a fermion  $f$  is given by

$$C(f) = \frac{ie}{\sin\theta_W \cos\theta_W} c(f), \quad (1.28)$$

$$c(f) = I_3 - e_f \sin^2\theta_W \quad (1.29)$$

Apart from the neutrino, the neutral current couplings, in contrast to the charged currents (see equation 1.19) are not pure  $V-A$  type, e.g.:

$$J_\mu^{neutr}(h) = \bar{u} \frac{1}{2} \gamma_\mu (c_L(1 - \gamma_5) + c_R(1 + \gamma_5)) u + \dots \quad (1.30)$$

Here, the coefficients  $c_L$  and  $c_R$  are the left handed and right handed chiral couplings corresponding to  $c(f)$  in equation 1.29.

The masses of the mediator bosons  $W^\pm$  and  $Z$  are acquired via the *Higgs mechanism*. As has been shown by Peter Higgs in 1964 [36], it is possible to generate masses for bosons (and fermions) without destroying gauge invariance (i.e. the renormalisability of the theory) by introducing a complex scalar field, called the Higgs field. The main assumption of this mechanism is a non-zero vacuum expectation value  $v$  for the Higgs field  $\phi$ . With a non-zero vacuum expectation value it is possible to generate screening currents to give mass to the weak gauge bosons.

The masses of the weak bosons  $W^\pm$  and  $Z$  are related to the vacuum expectation value  $v$  and couplings  $g$  and  $g'$  via:

$$M_W = \frac{g}{2}v \quad M_Z = \frac{\sqrt{g^2 + g'^2}}{2}v$$

Using 1.26,  $M_W$  and  $M_Z$  are related by the Weinberg angle:

$$\cos \theta_W = \frac{M_W}{M_Z} \quad (1.31)$$

The experimentally determined masses of the  $W^\pm$  and  $Z$  bosons are [24]:

$$M_{W^\pm} = 80.425 \pm 0.038 \text{ GeV} \quad M_Z = 91.188 \pm 0.002 \text{ GeV}$$

The vector and axial vector terms ( $\gamma_\mu$  and  $\gamma_\mu\gamma_5$ ) in 1.30 lead to the definitions of vector and axial vector charges (constants)  $v_f$  and  $a_f$  for fermions (Table 1.2). The relations of  $v_f$  and  $a_f$  to  $c_L$  and  $c_R$  are given by:

$$v_f = 2(c_L(i) + c_R(i))$$

$$a_f = 2(c_L(i) - c_R(i))$$

	$\nu_e, \nu_\mu, \nu_\tau$	$e, \mu, \tau$	$u, c, t$	$d, s, b$
$e_f$	0	-1	+2/3	-1/3
$c_L$	1/2	$-1/2 + \sin^2 \theta_W$	$1/2 - 2/3 \sin^2 \theta_W$	$-1/2 + 1/3 \sin^2 \theta_W$
$c_R$	0	$\sin^2 \theta_W$	$-2/3 \sin^2 \theta_W$	$1/3 \sin^2 \theta_W$
$v_f$	1	$-1 + 4 \sin^2 \theta_W$	$1 - 8/3 \sin^2 \theta_W$	$-1 + 4/3 \sin^2 \theta_W$
$a_f$	1	-1	1	-1

Table 1.2: Coupling constants of leptons and quarks to the  $Z$  boson.  $e_f$  is the electric charge of the fermion (is in units of  $e$ ).



## 1.2 Neutral and Charged Current Cross Sections

### 1.2.1 Unpolarised Lepton-Proton DIS Cross Sections

Including the weak neutral current ( $Z$  exchange), the neutral current differential cross section for unpolarised interacting particles is given as [14]:

$$\frac{d^2\sigma_{NC}^{e^\pm p}}{dx dQ^2} = \frac{2\pi\alpha^2}{xQ^4} \Phi_{NC}^{e^\pm p} \quad (1.32)$$

with the *reduced NC cross section* term

$$\Phi_{NC}^{e^\pm p} = Y_+ \tilde{F}_2^\pm \mp Y_- x \tilde{F}_3^\pm - y^2 \tilde{F}_L^\pm \quad (1.33)$$

Here,  $Y_\pm = 1 \pm (1-y)^2$  is the helicity factor (see equation 1.12),  $\tilde{F}_2^\pm$ ,  $\tilde{F}_3^\pm$  and the  $\tilde{F}_L^\pm$  are generalised structure functions.  $\tilde{F}_L^\pm$  is the longitudinal structure function with a contribution to the cross section proportional to  $y^2$ , therefore only important in the very high  $y$  region (in addition,  $\tilde{F}_L^\pm$  is small in the large  $Q^2$  range considered in this thesis). The  $\tilde{F}_L^\pm$  term will not be discussed further in this thesis.

$\tilde{F}_2^\pm$  and  $\tilde{F}_3^\pm$  can be expressed in terms of five structure functions describing the contributions from pure photon exchange,  $\gamma Z$  interference and pure  $Z$  exchange:

$$\tilde{F}_2^\pm = F_2 - v_e \left( \frac{\kappa_W Q^2}{Q^2 + M_Z^2} \right) F_2^{\gamma Z} + (v_e^2 + a_e^2) \left( \frac{\kappa_W Q^2}{Q^2 + M_Z^2} \right)^2 F_2^Z \quad (1.34)$$

$$x \tilde{F}_3^\pm = \pm a_e \left( \frac{\kappa_W Q^2}{Q^2 + M_Z^2} \right) x F_3^{\gamma Z} \mp 2a_e v_e \left( \frac{\kappa_W Q^2}{Q^2 + M_Z^2} \right)^2 x F_3^Z \quad (1.35)$$

Here, the pure photon exchange is described by  $F_2$ , pure  $Z$  exchange by  $F_2^Z$  and  $x F_3^Z$ , and  $\gamma Z$  interference by  $F_2^{\gamma Z}$  and  $x F_3^{\gamma Z}$ .  $v_e$  is the weak vector and  $a_e$  the weak axial-vector coupling of the electron to the  $Z$  (see equation 1.29) and are given in Table 1.2. The Weinberg angle  $\theta_W$  (see equation 1.27) enters the quantity  $\kappa_W$  in the following way:

$$\kappa_W = \frac{1}{4 \sin^2 \theta_W \cos^2 \theta_W}$$

In the Quark Parton Model (see section 1.1.3) the structure functions are expressed via quark and anti-quark densities:

$$[F_2, F_2^{\gamma Z}, F_2^Z] = x \sum_q [e_q^2, 2e_q v_q, v_q^2 + a_q^2] \{q(x, Q^2) + \bar{q}(x, Q^2)\} \quad (1.36)$$

$$[xF_3^{\gamma Z}, xF_3^Z] = x \sum_q [e_q^2 a_q, 2v_q a_q] \{q(x, Q^2) - \bar{q}(x, Q^2)\} \quad (1.37)$$

The sums run over all quark flavors  $q$ . Due to the limited kinematic range at HERA the sum runs over five quark flavors, i.e. the center of mass energy  $\sqrt{s}$  is not sufficient to produce a top quark.

The Charged Current cross section can be presented in a form similar to the one of NC reactions [14]:

$$\frac{d^2 \sigma_{CC}^{e^\pm p}}{dx dQ^2} = \frac{G_F^2}{2\pi x} \left( \frac{M_W^2}{Q^2 + M_W^2} \right)^2 \Phi_{CC}^{e^\pm p} \quad (1.38)$$

with the *reduced CC cross section* term  $\Phi_{CC}^{e^\pm p}$ , also often denoted as  $\tilde{\sigma}_{CC}$ :

$$\Phi_{CC}^{e^\pm p} = \tilde{\sigma}_{CC} = Y_+ \tilde{W}_2^\pm + y^2 \tilde{W}_L^\pm \mp Y_- x \tilde{W}_3^\pm \quad (1.39)$$

Here,  $G_F$  is the Fermi constant which is related to the weak coupling  $g$  and electromagnetic coupling  $e$  (see eq 1.27):

$$G_F = \frac{g^2}{4\sqrt{2}M_W^2} = \frac{e^2}{4\sqrt{2}\sin^2\theta_W M_W^2} \quad (1.40)$$

$\tilde{W}_2^\pm$ ,  $\tilde{W}_L^\pm$  and  $\tilde{W}_3^\pm$  are structure functions analogous to the Neutral Current case (see eq. 1.33). Since the Charged Current interactions are purely weak processes,  $W_2^\pm$ ,  $W_L^\pm$  and  $W_3^\pm$  do not contain electromagnetic and interference terms. The generalised CC structure functions for unpolarised interacting particles can be expressed [37] as:

$$\tilde{W}_2^\pm = \frac{1}{2} W_2^\pm \quad (1.41)$$

$$x \tilde{W}_3^\pm = \mp \frac{1}{2} x W_3^\pm \quad (1.42)$$

In the Quark Parton Model  $W_2^\pm$  and  $W_3^\pm$  ( $W_L^\pm = 0$ ) are sensitive to differences of quark and anti-quark distributions and are given by:

$$\begin{aligned} e^+ : \quad & W_2^+ = 2x(d + s + \bar{u} + \bar{c}), & xW_3^+ &= 2x(d + s - [\bar{u} + \bar{c}]) \\ e^- : \quad & W_2^- = 2x(u + c + \bar{d} + \bar{s}), & xW_3^- &= 2x(u + c - [\bar{d} + \bar{s}]) \end{aligned} \quad (1.43)$$

The  $b$  and  $t$  quarks do not contribute to  $W_2^\pm$  and  $xW_3^\pm$  because of two reasons: First, the  $t$  quark is too massive to be produced in the HERA kinematic range, secondly, the probability of the  $u \rightarrow b$  transition according to the Cabibbo-Kobayashi-Maskawa matrix is very small ( $U_{ub}$ , see equation 1.21).

According to 1.43, the structure function term  $\tilde{\sigma}_{CC}$  is related to the quark densities via

$$\begin{aligned} e^+ : \quad \tilde{\sigma}_{CC}^{e^+p} &= x[\bar{u} + \bar{c}] + (1-y)^2 x[d + s] \\ e^- : \quad \tilde{\sigma}_{CC}^{e^-p} &= x[u + c] + (1-y)^2 x[\bar{d} + \bar{s}] \end{aligned} \tag{1.44}$$

### Electro-weak Unification

Unpolarised neutral and charged current cross sections measured with the H1 detector at HERA I as function of  $Q^2$  are shown in Figure 1.6. As seen in the picture, NC and CC cross sections become about equal in magnitude at  $Q^2 \gtrsim 10^4 \text{ GeV}^2$ . This follows from the propagator term  $(1/Q^2)^2$  for NC and  $(1/Q^2 + M_W^2)^2$  for CC interactions introducing a  $Q^2$  dependence which is different for NC and CC until  $Q^2 \lesssim M_{Z(W)}^2$ .

This so-called *electro-weak unification* region is predicted by the electroweak sector of Standard Model as was described in section 1.1.5 (see also equation 1.40).

### $e^+p$ and $e^-p$ Charged Current Cross Sections

The differences between  $e^+p$  and  $e^-p$  charged current cross sections (see Figure 1.6) arise due to the following factors:

- the proton is composed of two  $u$  and one  $d$  valence quark,  $e^+$  probes the  $d$  quark while  $e^-$  probes the  $u$  quark (see eq. 1.43, 1.44). Since the coupling strength of the  $W$  is the same for all fermions, this implies a factor of two in the electron-quark charged current interactions;
- conservation of angular momentum implies a  $(1 - \cos\theta)^2$  dependence of the scattered  $\bar{\nu}$  for  $e^+p$  interactions in the center of mass (CM) frame (backscattering is not allowed). The distribution of the angular momentum is flat for  $\nu$  in  $e^-p$  reactions (see Figure 1.7). Conservation of angular momentum brings another factor of three difference in the  $e^+p$  and  $e^-p$  cross sections;
- at high four momentum transfer squared  $Q^2$ , the  $d$  quark distribution as function of  $x$  falls off faster at large  $x$  than the one of the  $u$  quark [18].

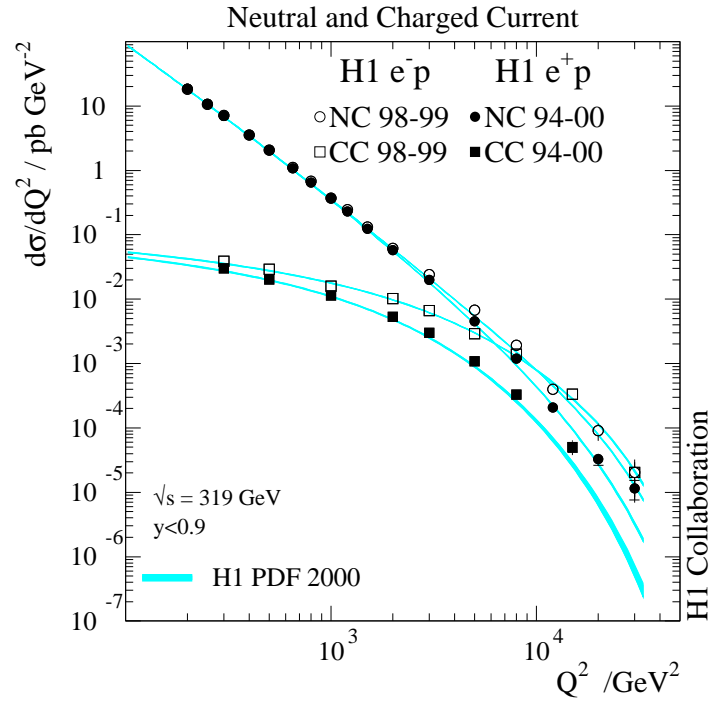


Figure 1.6: Cross sections of unpolarised neutral (circles) and charged current (boxes) deep inelastic scattering processes as function of  $Q^2$ , measured with the H1 detector. The  $e^+p$  collisions are shown as full symbols,  $e^-p$  as open symbols. The results are compared to the Standard Model expectations using a NLO QCD fit (band). From [18].



Figure 1.7: Illustration of the angular dependence in charged current reactions (in the CM frame, assuming the  $z$  direction along the  $e^\pm$  motion and  $\theta$  being the scattering angle of the  $\nu$ ): (left) the angular momentum component  $J_z$  is not conserved if the  $\bar{\nu}$  is scattered backwards, i.e. the interaction amplitude is proportional to  $(1 - \cos \theta)$ ; (right) the interaction amplitude does not depend on  $\theta$  because  $J_z = 0$ .

### 1.2.2 DIS Cross Sections with Polarised Leptons

After the upgrade of HERA in the year 2000 (details of the upgrade will be discussed in chapter 2), HERA has the capability to longitudinally polarise the lepton beam. The polarisation of the lepton beam  $P_e$  (electron or positron) is defined as:

$$P_e = \frac{N_R - N_L}{N_R + N_L}. \quad (1.45)$$

Here,  $N_R$  ( $N_L$ ) is the number of right (left) handed leptons in the beam. In an unpolarised beam, the number of left and right handed leptons is the same. The charged current cross section of polarised leptons with unpolarised protons is predicted by the Standard Model to have a linear dependence on the lepton polarisation  $P_e$  (all variables as explained in eq. 1.38):

$$\frac{d^2\sigma_{CC}^{e^\pm p}}{dx dQ^2} = (1 \pm P_e) \frac{G_F^2}{2\pi x} \left( \frac{M_W^2}{Q^2 + M_W^2} \right)^2 \tilde{\sigma}_{CC}^{e^\pm p} \quad (1.46)$$

As seen in the equation above, the total CC cross section thus is equal to zero for "left-handed" (see Figure 1.5) positrons as well as for "right-handed" electrons.

Unlike for charged currents, the cross section for neutral current reactions is influenced by the longitudinal lepton polarisation only at high  $Q^2$ . This dependence appears via the  $Z$  exchange and can be expressed in the following way:

$$\frac{d^2\sigma_{NC}^{e^\pm p}}{dx dQ^2} = \frac{2\pi\alpha^2}{xQ^4} \left[ \Phi_{NC}^{e^\pm p} + P_e \Phi_{NCpol}^{e^\pm p} \right] \quad (1.47)$$

Here,  $\Phi_{NCpol}^{e^\pm p}$  is similar to  $\Phi_{NC}^{e^\pm p}$  but involves polarised structure functions. More detailed description can be found in [38].

### 1.2.3 Radiative Corrections

The cross sections presented in the last two sections are calculated at the leading-order (LO or Born approximation,  $\mathcal{O}(\alpha^2)$ ). The main contribution to higher order processes comes from additional photon lines, either internal (virtual) or external (real). The emission of the real photon can change the  $ep$  centre-of-mass energy and thus the event kinematics is also changed. Therefore the measured cross sections have to be corrected for higher order radiative effects (typically of order few percents) denoted by the correction term  $\delta^{rc}$  [39]:

$$\frac{d^2\sigma}{dx dQ^2} = \frac{d^2\sigma}{dx dQ^2} \Big|_{Born} \frac{1}{1 + \delta^{rc}} \quad (1.48)$$

More generally, the radiative corrections can be separated into two contributions: The ones rising from the electromagnetic and those from the weak processes:

$$1 + \delta^{rc} = (1 + \delta^{QED})(1 + \delta^{weak}) \quad (1.49)$$

The calculation of the radiative corrections for the NC cross sections involves a set of Feynman diagrams, each being a gauge invariant [39]. A detailed discussion about the radiative correction for the NC scattering is given in [39]. The separation of the QED - weak contributions for the CC radiative corrections is described in [40] and will be shortly discussed in this section.

#### *Radiative corrections for CC scattering*

The four leading Feynman diagrams for radiative CC scattering (i.e. with additional photons) are shown in Figure 1.8: The emission of a photon from the incoming electron (a), from the incoming and outgoing quark (b, c) and from the  $W$  (d). Similarly to the real corrections shown in Figure 1.8, the virtual electroweak one-loop diagrams (corrections to the  $e\nu W$  and  $qq'W$  vertices, self-energy corrections of the involved particles) also give rise to infrared divergences. After combining real and virtual corrections, the infrared divergences cancel each other and the resulting QED corrections on the CC cross section can be expressed in the following way [40]:

$$\frac{d^2\sigma}{dx dQ^2} = \frac{d^2\sigma}{dx dQ^2} \Big|_{Born} (1 + e_l^2 J_{lep} + e_l e_f J_{int} + e_f^2 J_{qua}) \quad (1.50)$$

Here,  $J_{lep}$ ,  $J_{int}$  and  $J_{qua}$  are the "leptonic", "interference" and "quarkonic" contributions, each being gauge invariant;  $e_l$  and  $e_f$  are charges of the electron and the incoming quark, respectively.

The terms  $J_{int}$  and  $J_{qua}$  in the numerical programs for the calculation of DIS cross sections are usually neglected (the results for the individual contributions are available in [41], [42]). However, it is important to notice (for the studies presented in section 5.2.2) that the leptonic contribution  $J_{lep}$  involves terms containing the photon radiation of the incoming electron (Figure 1.8 (a)), as well as the terms involving the outgoing quark radiation (Figure 1.8 (c)).

As mentioned above, the CC radiative corrections also contain purely weak contributions. They arise mostly due to  $W$  self-energy terms. The influence of the weak radiative corrections are small and are discussed in [43].

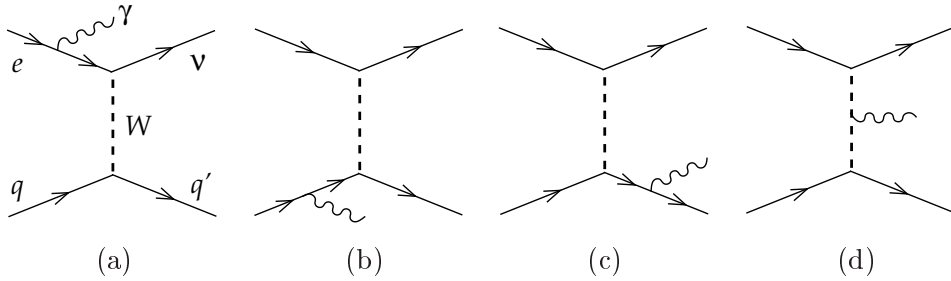


Figure 1.8: *Feynman diagrams for radiative charged current scattering with the emission of the photon from the incoming electron (a), from the incoming and outgoing quark (b,c), from W (d).*

The photon radiation of the incoming electron is common for both, CC and NC, and is usually called Initial State Radiation (ISR). The photon radiation of the outgoing electron exists only in NC events and is called Final State Radiation (FSR).

### 1.3 Background Processes to Charged Current

The typical signature of charged current events is missing transverse momentum originating from the escaping neutrino. Therefore, the background to charged current interactions are  $ep$  events with an apparent transverse momentum imbalance usually caused by imperfect detection of the final state particles. There are two reasons why a missing momentum can be measured in transversely balanced events: Part of the event final state may escape detection, or the measurement of the final state was inaccurate (resolution effects).

The possible background processes to CC are photoproduction, neutral current events, lepton pair and real  $W$  production. In the following these background classes are described<sup>4</sup>.

#### 1.3.1 Photoproduction

Photoproduction ( $\gamma p$ ) is a processes where a quasi-real (i.e. almost on the mass shell) photon, emitted by the electron, is interacting with the proton. The cross section of events with photon exchange depends on the four-momentum transfer as  $1/Q^4$  (see 1.32). Therefore, photoproduction is the dominant process as  $Q^2 \rightarrow 0$  (events with  $Q^2 \gtrsim \text{few } GeV^2$  are considered as DIS NC events).

<sup>4</sup>The contribution of NC events to CC background and their rejection methods are discussed in section 5.1.3.

Two examples of photoproduction processes are presented in Figure 1.9. The reaction on the left side of the Figure 1.9 usually is called the *direct* process (the whole photon takes part in the hard subprocess with a parton from the proton), while the reaction on the right side represents a *resolved* process (the photon acts as a source of partons, one of which takes part in the hard subprocess). The hadronic final state in the photoproduction process consists of two (or more) jets.

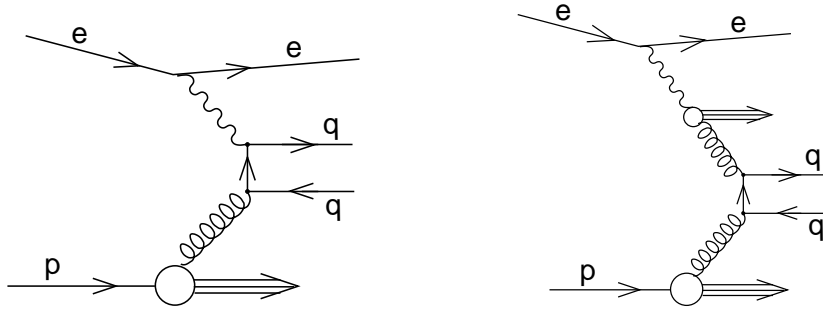


Figure 1.9: *Feynman diagrams for direct (left) and resolved (right) photoproduction processes.*

The photoproduction events can "obtain" a missing transverse momentum in the detector (i.e. become background to CC) when some hadronic final state particles (e.g.  $\nu$ 's) escape detection, and (or) by imperfect measurement of the hadronic final state due to limited detector acceptance.

Photoproduction interactions are the main background to CC events (at low  $Q^2$  the rate of  $\gamma p$  events is a few hundred times larger than the CC rate).

### 1.3.2 Lepton-Pair Production

The dominant process for lepton-pair production at HERA is  $ep \rightarrow epl^+l^-$  or  $ep \rightarrow eXl^+l^-$  (the pair of leptons mainly originate from photon-photon interactions, photons being radiated by the electron and the proton). If the lepton pair in the final state is  $\mu^+\mu^-$  (Figure 1.10), the event may look like the CC event because muons do not contribute much to the calorimetric energy. If the lepton pair consist of electrons, they will be measured in the detector and will usually not cause any missing transverse momentum. The typical rate of the lepton-pair event production process is about 8 events per  $1 pb^{-1}$  of luminosity (the CC event rate is about 40 events per  $1 pb^{-1}$ ).



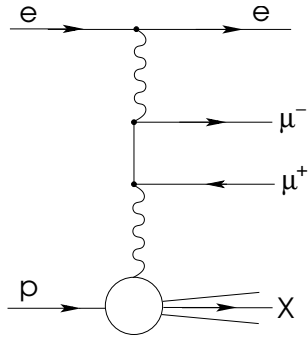


Figure 1.10: *Feynman diagram of the lepton pair production:  $ep \rightarrow e\mu^+\mu^-X$ .*

### 1.3.3 W Production

Another rare process is real  $W^\pm$  production. The  $W^\pm$  is produced in  $ep \rightarrow eWX$  or  $ep \rightarrow \nu WX$  reactions. When the boson decays leptonically, the event final state may mimic a charged current reaction due to the produced  $\nu$ . An example diagram where the  $W^-$  decays into  $\mu^-\nu_\mu$  is shown in Figure 1.11. The real boson production process has a very small cross section at HERA [44] (typically about one event is expected per  $2 \text{ pb}^{-1}$  of luminosity).

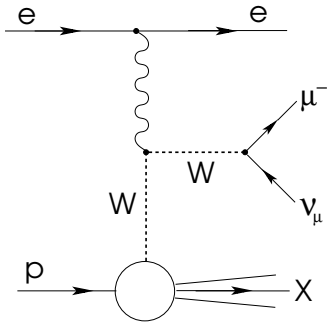


Figure 1.11: *Feynman diagram for real  $W^\pm$  production:  $ep \rightarrow eWX$ .*

## 1.4 Monte Carlo (MC) event generators

Monte Carlo event generators are programs to simulate particle reactions in the detector. MC's are used in various physics analyses as a powerful tool to estimate detector effects, which cannot be determined from the data. The main reasons for simulating specific physics processes in this analysis are:

- the determination of the detector acceptance,
- the contribution of the background processes,
- the determination of the efficiency of selection cuts,
- the estimation of radiative effects.

All these points will be discussed in the further chapters.

The main steps to produce Monte Carlo simulated specific physics processes are shortly described below.

### Generation of the Specific Physics Processes

Event generators contain the Born level QCD matrix elements of hard processes. The first step to produce MC simulated processes is the random event generation initialised according to these matrix elements specific for the physics process. The next step is simulation of parton showering and hadronisation processes.

#### *Parton Showering and Hadronisation*

The creation of hadronic states from the initial partons involves two distinct processes, *parton showering* and *hadronisation*. Higher order QCD radiation is represented by leading logarithmic parton showers. In this stage the high energy primary partons lose their energy radiating secondary partons which, in turn, produce others and so on. These branchings of partons are done according the splitting functions as described in section 1.1.4 (Figure 1.4). The process stops when the energies of the partons become too small, i.e. below  $\sim 1 \text{ GeV}$ . At such small energies the strong coupling,  $\alpha_s$ , is too large and the showering processes cannot be described anymore by perturbative QCD. At this stage, the final state consists of many "free" partons, i.e. quarks and gluons. Then *hadronisation* takes place which employs empirical models to describe the formation of the hadronic final state. Here, colored partons are bound into colorless hadrons.

A schematic view of the  $e^\pm p$  scattering process illustrating parton showering and hadronisation is given in Figure 1.12.

There are several different algorithms to generate parton showering and hadro-

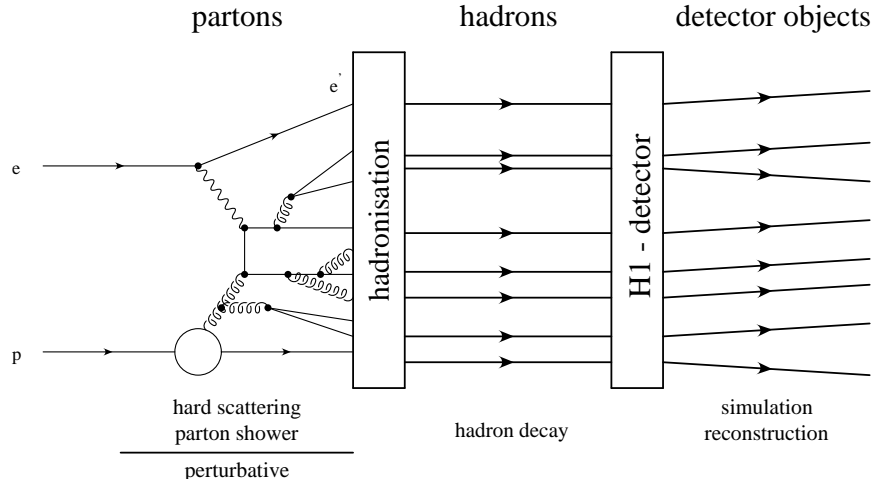


Figure 1.12: *Schematic illustration of the  $ep$  scattering process over perturbative (hard scattering) and non-perturbative processes including the simulation of particles and their reconstruction (reconstruction is described in chapter 3).*

nisation processes. Often used (in this analysis as well) are the *Colour Dipole Model* (CDM) [46] for the parton showering and the *Lund String Fragmentation* [47] for hadronisation. As a result of the generation a list of the final state particles, characterised by their four-vectors, is created.

#### *Generators used in the present analysis*

Charged and neutral current events were generated with DJANGO 1.2 [48]. The lepton-proton scattering in DJANGO is based on LEPTO [49] including leading order QED corrections with the HERACLES [50] program. The parton showering is generated according to ARIADNE [51] using the Colour Dipole Model. JETSET [52] is used to simulate the hadronisation process with the Lund String Fragmentation model. The parametrisation of MRSH [53] is used for the proton PDF and at the analysis level is corrected to the parametrisation of H1 PDF 2000 [18].

Photoproduction processes are generated with PYTHIA [54]. The leading order parametrisation CTEQ [55] is used for the proton PDF and GRV [56] for the photon PDF.

Lepton pair production processes were generated with GRAPE [57].

Real  $W^\pm$  production mechanisms were generated with the EPVEC [44] program.

In this analysis 100 000 of generated charged current events were used, almost 1 million of NC events,  $\sim 3$  million of photoproduction events and more than 400 000 of lepton-pair and  $W$  production events.

### **Detector Simulation**

In this step, which is the same for all MC generators, the interactions of the generated particles with the detector material are simulated. This is done by propagating the generated final state particles using their four-vector information and simulating random interactions with the different detector components. The simulation of electromagnetic and hadronic showers in the calorimeters is done with a fast parametrisation program H1FAST [58]. The detector response is calculated from the simulated interactions, ionisations and energy deposits.

In the H1 experiment a full detector simulation is created with the H1SIM [59] software using the GEANT [60] program.

### **Particle Reconstruction**

The simulated events are subjected to the same reconstruction and analysis chain as the data. The relevant particle reconstruction methods for this analysis (same for data and MC) are described in chapter 3.

### **MC to Data Correction**

After the simulation and reconstruction steps, some detector effects may not be fully modelled in the MC events. Therefore, it is important at the analysis level to ensure that the MC simulation correctly models the detector response and describes the data in every analysis aspect. As will be described in detail in chapters 4-6, in case of observed discrepancies, the simulation is corrected to describe the data.

## Chapter 2

# The H1 experiment at HERA

The HERA ("Hadron Elektron Ring Anlage") accelerator is the only machine world-wide colliding electrons with protons. Two detectors to register  $ep$  collisions were designed and built in the end of the eighties with the major task is to study the structure of the proton. The kinematic range of HERA is more than two orders of magnitude larger than the range accessible so far in fixed target experiments (see Figure 2.1).

In this chapter a short description of the HERA accelerator and the H1 detector is given. Emphasis is put on the H1 trigger system and the studies performed to reduce the DIS event trigger rates using the second level neural network trigger (L2NN).

### 2.1 HERA Accelerator

The HERA accelerator (Figure 2.2) is located at DESY (Deutsches Elektronen Synchrotron), Hamburg. It has the circumference of 6.3  $km$  and separate storage rings for electrons and protons. Electrons are accelerated to 27.6  $GeV$  and protons to 920  $GeV$  (820  $GeV$  before 1998). The energy of the electron beam energy is limited by synchrotron radiation while the  $p$  beam is limited in energy by the strength of the magnetic field of the superconducting dipole magnets.

The collisions at the center-of-mass energy  $\sqrt{s} = 318 GeV$  (301  $GeV$  before 1998) take place in two interaction regions surrounded by two large multipurpose detectors, H1 [61] and ZEUS [62]. In addition, there is one operational fixed-target experiment, HERMES [63], where the electron beam is brought into collision with polarised gas targets in order to study the spin structure of the proton. The second fixed-target experiment, HERA-B [64], where the proton beam was used to produce final states with  $b$  quarks, has been completed.

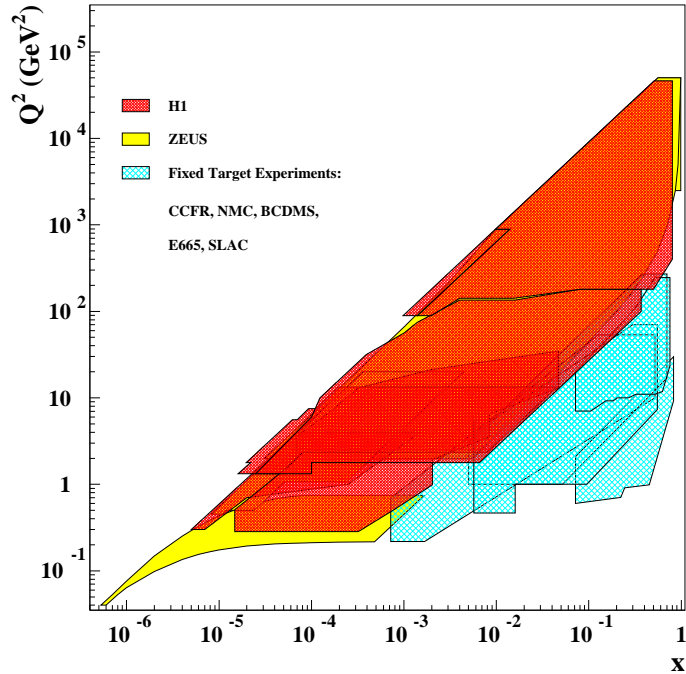


Figure 2.1: Kinematic plane  $(x, Q^2)$  of HERA and comparison with some fixed target experiments.

The accelerator rings can store up to 210 particle bunches for each of the electron and proton beams (due to limitations of the injection system only 180 colliding bunches are stored routinely). Each bunch contains approximately  $10^{11}$  particles and are separated by 96 ns time intervals. In addition to the colliding bunches, there are usually about 10 bunches in each beam without colliding partners (*pilot bunches*). Measuring reactions induced by such electron or proton pilot bunches enables studying non- $ep$  induced background (for example, beam-gas events originating from proton collisions with the remaining gas nuclei in the beam).

HERA was successfully running from the year 1992 until the end of 2000 ("HERA I"). After a long shutdown (lasting from the years 2001 and 2002), the second, "HERA II", period was started. Two major improvements have been achieved during the shutdown. New focussing magnets were installed inside the detectors, leading to significant increase of the instantaneous luminosity  $\mathcal{L}$ , which is defined as:

$$\mathcal{L} = \frac{f N_e N_p}{4\pi \sigma_x \sigma_y} \left[ \frac{1}{\text{cm}^2 \text{s}} \right] \quad (2.1)$$

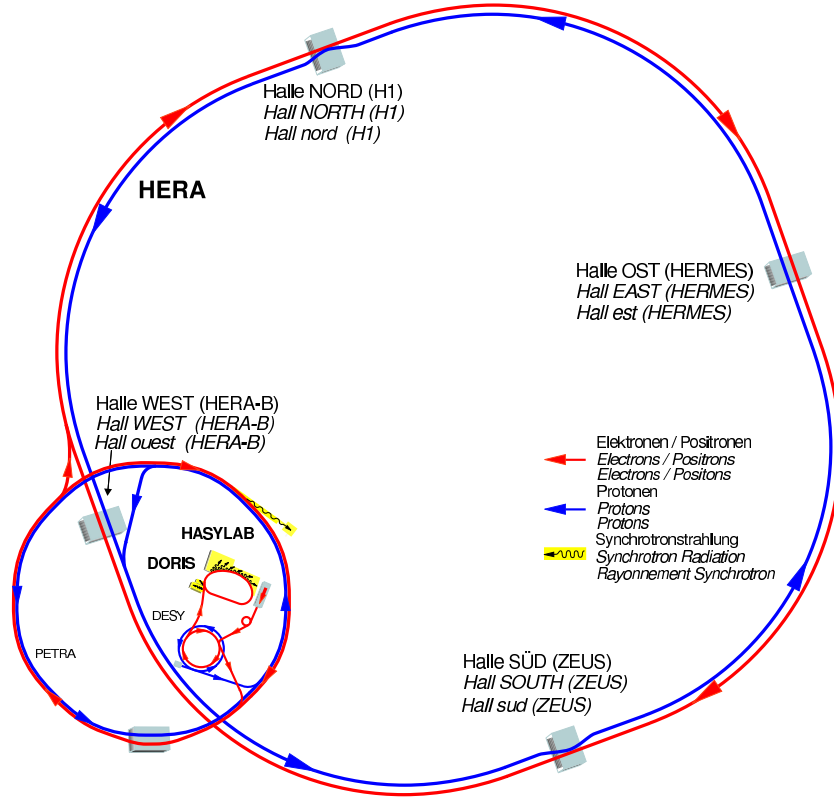


Figure 2.2: Schematic view of the HERA accelerator.

Here,  $f$  is the bunch crossing frequency,  $N_e$  and  $N_p$  are the number of electrons and protons in each bunch, and  $\sigma_x$  and  $\sigma_y$  are the Gaussian transverse beam profiles in the  $x$  and  $y$  directions at the interaction point.

Any physical cross section is related with the number of observed events  $N$  and the integrated luminosity  $L$  as:

$$\sigma = \frac{N}{L}$$

The integrated luminosity in the equation above is given as  $L = \int \mathcal{L} dt$ . The integrated luminosity collected by H1 for the HERA I and HERA II periods (until the end of 2005) versus time is shown in Figure 2.3. From the figure one can see that the installation of the focussing system has improved the instantaneous luminosity by about a factor of three.

The second improvement of HERA II is the possibility to longitudinally polarise the electron beam (for physics explanations and consequences of longitudinally polarised leptons to DIS reactions, see section 1.2.2). The longitudinal electron beam polarisation is achieved installing spin rotators around the interaction regions in the HERA ring.

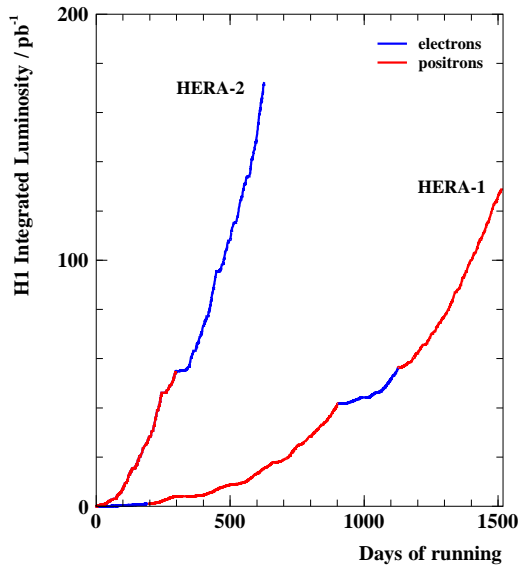


Figure 2.3: *H1 integrated luminosity as function of time for HERA I and HERA II periods, up to the end of the year 2005.*

### 2.1.1 Longitudinal $e$ Beam Polarisation at HERA II

The electrons at HERA become transversely polarised through the emission of synchrotron radiation (the Sokolov-Ternov effect [65]): When electrons move in closed orbits guided by the magnetic dipole fields of a storage ring, they emit synchrotron radiation; a very small fraction of the emitted photons will cause a spin-flip between "up" and "down" quantum states of the electron spin. Since the probabilities of the "up-to-down" and "down-to-up" spin states are different, the initially unpolarised electron beam becomes polarised with time according to:

$$P(t) = P_{max}(1 - e^{-t/\tau}) \quad (2.2)$$

Here,  $P_{max}$  is a theoretical limit for the maximal polarisation and is  $\simeq 0.93$  (not taking into account possible depolarisation effects);  $\tau$  is the build-up time. For a storage ring with radius  $R$  and electron energy  $E_e$ ,  $\tau \sim R^2/E_e^5$  which amounts to  $\approx 40 \text{ min}$  at HERA.

To achieve longitudinal electron polarisation for the  $ep$  interactions the vertical polarisation is rotated into longitudinal just before the interaction point and, in order to maintain stable beam polarisation, it must be rotated back to vertical immediately after. At HERA II, the chains of special magnets, so-called *spin rotators* [66] were installed near the H1 and ZEUS detectors



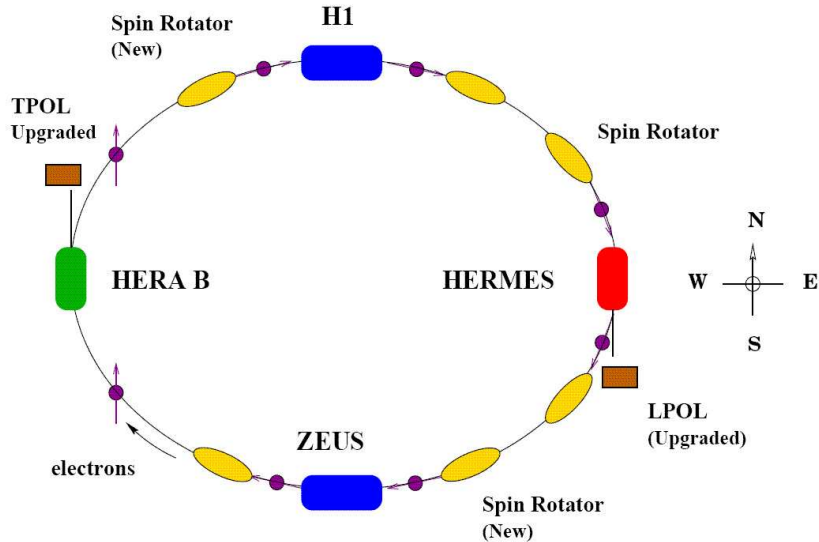


Figure 2.4: Schematic view of the HERA ring after the upgrade.

(the HERMES experiment already had such spin rotators during the HERA I period. The schematic representation of the HERA ring after the upgrade with installed spin rotators is shown in Figure 2.4.

The achievable degree of longitudinal electron polarisation is limited by many factors which have to be taken into account building up and maintaining the polarisation in the storage ring. For example, the so-called "spin matched" rotator optics is influenced by the magnet alignment and positioning precision, field errors and orbit corrections, number of beam position monitors, etc. The technique used for optimising the polarisation in the HERA ring is called *harmonic closed orbit spin matching* and is described in [67, 68].

The typical degree of polarisation achieved at HERA II is  $\approx 40\%$ , as shown in Figure 2.5.

### Polarisation Measurement

There are two techniques to measure the polarisation in electron scattering: Möller scattering,  $ee \rightarrow ee$ , and Compton scattering,  $\gamma e \rightarrow \gamma e$ . The first method is experimentally simple, but limited to beam currents  $I_e \leq 5\mu A$ . The second method is more complicated to implement but is fast and accurate, and is therefore routinely used in experiments operating with high beam currents.

Both longitudinal and transverse electron polarisation measurements at HERA rely on the same physical principle: Spin dependent Compton scattering of circularly polarised laser light (photons) off polarised beam electrons.

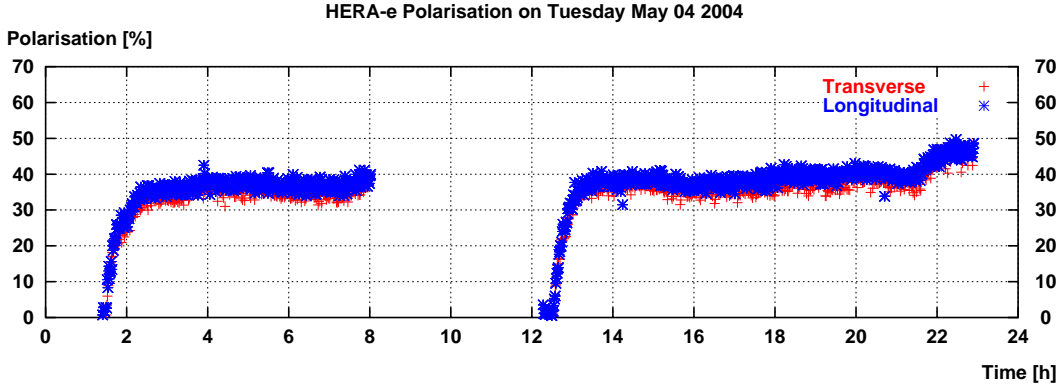


Figure 2.5: Typical HERA II longitudinal and transverse polarisation as function of time.

The cross section for the Compton scattering process,  $\gamma e \rightarrow \gamma e$ , is a well known QED process, expressed as [69, 70]:

$$\frac{d^2\sigma}{dEd\phi} = \Sigma_0(E) + S_1\Sigma_1(E) \cos 2\phi + S_3 [P_Y\Sigma_{2Y}(E) \sin \phi + P_Z\Sigma_{2Z}(E)] \quad (2.3)$$

$S_1$  and  $S_3$  are the linear and circular components of the photon beam polarisation<sup>1</sup>,  $P_Y$  and  $P_Z$  are the transverse and longitudinal components of the electron beam polarisation,  $\Sigma_i$  are calculable terms depending on the photon energy. From the equation above one can see that

- a measurement of the polarisation can be performed by switching the sign of  $S_3$  (maximising the circular polarisation  $S_3 \rightarrow \pm 1$  and thus minimising the linear terms  $\sqrt{S_1^2 + S_2^2} \rightarrow 0$ ). This results in an asymmetry which is proportional to  $P_Z$ ;
- if the polarisation of the laser beam is known, the longitudinal polarisation of the electrons can be determined from the azimuth photon energy distribution; to determine the transverse polarisation, in addition to the energy distribution, the azimuthal distribution of the photon has to be measured.

There are two polarimeters which independently measure the degree of transverse and longitudinal polarisation at HERA: The Transverse Polarimeter (TPOL [71]) and the Longitudinal Polarimeter (LPOL [72, 73]). TPOL measures the *spatial energy asymmetry* (including the azimuthal information), LPOL measures the *energy asymmetry*. As the spin rotator system does not change the degree of lepton beam polarisation, the measurements of TPOL and LPOL must be consistent in magnitude.

<sup>1</sup>Generally, to describe light polarisation the Stokes vector  $S$  is used. For the polarised light  $S = \sqrt{S_1^2 + S_2^2 + S_3^2}$ ,  $S_3$  here refers to the degree of circular polarisation.

### The Transverse Polarimeter

The transverse polarisation is determined by measuring the *spatial* vertical "up-down" *asymmetry* of the energy distribution of single back scattered Compton photons. The photons are produced in a 10W Ar laser and are circularly polarised. The Compton photons are detected in a vertically segmented calorimeter which measures their energies in the upper ( $E_{up}$ ) and lower ( $E_{down}$ ) halves. The experimentally measured energy asymmetry  $A_{exp}$  is equal to:

$$A_{exp} = \frac{\langle E_{up} \rangle - \langle E_{down} \rangle}{\langle E_{up} \rangle + \langle E_{down} \rangle} \quad (2.4)$$

The longitudinal component of the electron beam polarisation  $P_z$  can be obtained through the difference of the mean values of  $\langle A_{exp} \rangle$  switching the laser light between two circular polarisation states,  $L$  and  $R$ :

$$\Delta A_{exp} = \frac{\langle A_{exp} \rangle_L - \langle A_{exp} \rangle_R}{2} = \Delta S_3 P_z A_{\text{TPOLE}}(E_\gamma) \quad (2.5)$$

$A_{\text{TPOLE}}(E_\gamma)$  is the so-called analysing power which has to be checked through calibration and formally is given by:

$$A_{\text{TPOLE}} = \frac{\int \rho \sigma_1(\rho) R(\rho) d\rho}{\int \rho \sigma_0(\rho) R(\rho) d\rho} \quad (2.6)$$

Here,  $\rho = E_\gamma / E_{\gamma, \text{max}}$  is the ratio of the scattered photon energy to its maximum value and  $R(\rho)$  is the detector response function. The Compton cross section is given by  $\sigma_c(\rho) = \sigma_0(\rho) \pm \sigma_1(\rho)$  where the upper sign corresponds to the total spin 3/2 of the electron-photon configuration (initial spins of  $e$  and  $\gamma$  are aligned), the lower sign corresponds to the total spin 1/2 (initial spins are anti-aligned).

The polarimeter is calibrated in parallel to the actual measurement using the Compton edge in the energy spectrum<sup>2</sup>.

The relative uncertainty of the polarisation measurements using TPOLE was determined to be 3.5% [74].

### The Longitudinal Polarimeter

The measurement of the longitudinal electron polarisation is based on the energy asymmetry of the backscattered photons. The photons are delivered by the high intensity Nd:YAG laser (Figure 2.6). The energy weighted cross sections of the backscattered photons are used to obtain  $P_z$ . The energy weighted asymmetry  $A_{exp}$  is given by:

<sup>2</sup>The "Compton edge" is the maximum back-scattered photon energy and is given by  $E'_{\gamma, \text{max}} \sim 4yE_\gamma\gamma^2$ . Here,  $E_\gamma$  is the incident photon energy,  $y = [1 + 4E_e E_\gamma / m_e^2]$  and  $E_e$  is the incident electron energy.

$$A_{exp} = \frac{\langle E \rangle_L - \langle E \rangle_R}{\langle E \rangle_L + \langle E \rangle_R} = \Delta S_3 P_z A_{LPOL}(E_\gamma) \quad (2.7)$$

Here,  $\langle E \rangle_L$  and  $\langle E \rangle_R$  are the means of the measured photon energies belonging to the different photon polarisation states,  $A_{LPOL}$  is the analysing power of LPOL.

LPOL is designed to operate in two<sup>3</sup> modes: *single-photon mode* (number of scattered photons per bunch  $n_\gamma \approx 0.001$ ) and *multi-photon mode* ( $n_\gamma \approx 1000$ ). In the single photon mode the energy of each individual photon is analysed, therefore, the high measurement accuracy can be achieved. The simulated photon energy distribution with  $P_z = 0.5$  using HERA electron beam parameters is shown in Figure 2.7. The disadvantage of this method is low statistics and high bremsstrahlung background which originates from collisions of the electron beam with the residual gas in the beam pipe. Therefore the single photon mode is used for the test and diagnosis purposes only.

In the multi-photon mode, the total energy of all deposited photons in the calorimeter is measured. The advantage of this mode is small background as there is enough statistics per single bunch to overcome the bremsstrahlung background. The asymmetry is formed by the measured average photon energy sums  $I_{1/2}$  and  $I_{3/2}$ , correspond to the total spin 1/2 and 3/2 of the electron-photon configurations (Figure 2.8). This mode is used as the standard LPOL operation.

The relative uncertainty of the polarisation measurements of LPOL for the years 2003-04 was determined to be 1.6% [75].

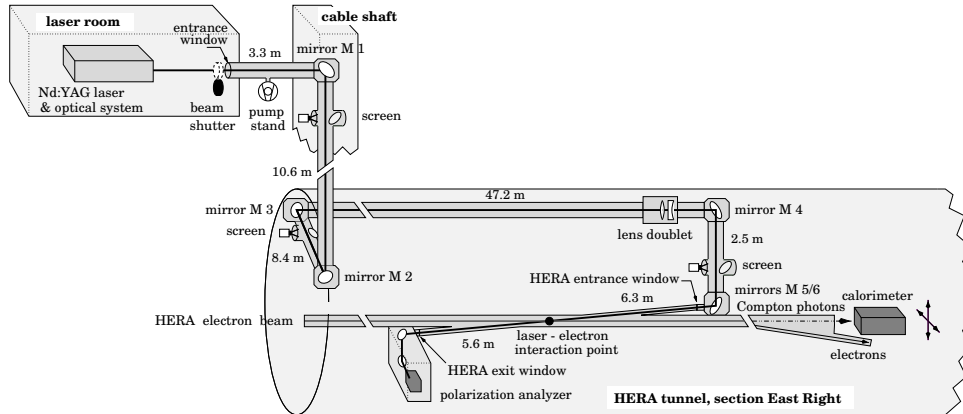


Figure 2.6: Layout of the longitudinal polarimeter (LPOL) at HERA.

<sup>3</sup>The possibility of an additional *few-photon* ( $n_\gamma \approx 1$ ) mode which was never considered in other experiments has been analysed for LPOL. The details of this study are given in [69].

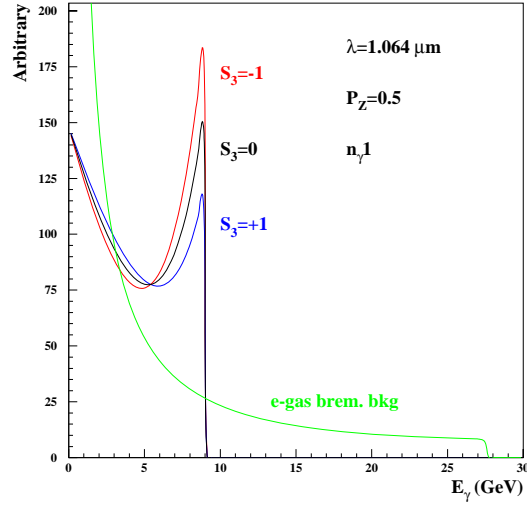


Figure 2.7: *Simulated backscattered Compton photon energy spectra collected in the single photon mode [69] for different values of circular polarisation ( $S_3 = 0, +1, -1$ ). The bremsstrahlung background (the normalisation to the Compton spectra is arbitrary but largely suppressed in scale) is also shown.*

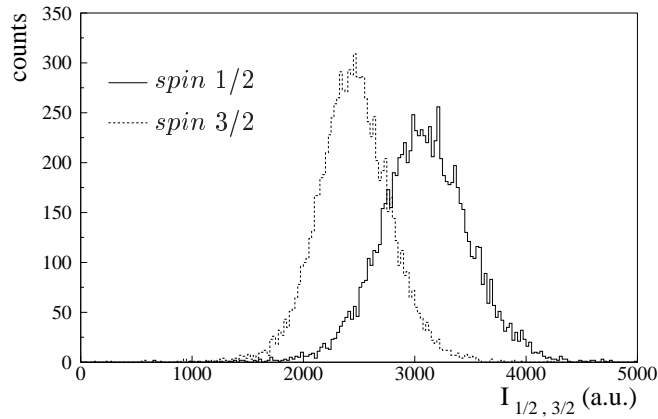


Figure 2.8: *Experimentally measured backscattered Compton photon energy spectra collected in the multi-photon mode for  $S_3 = +1$  (corresponding to the total spin  $3/2$  electron-photon configuration in the plot) and  $S_3 = -1$  (total spin  $1/2$ ). From [75].*

## 2.2 H1 Detector

The H1 detector [76] was designed and built as a general purpose detector to study  $ep$  interactions at HERA. The design of the detector is similar to most of the colliding experiment detectors with the exception of its longitudinal asymmetry. The "forward" part of the detector, defined as the direction of the incident proton (positive  $z$  in the H1 coordinate system) and the "backward" part (negative  $z$  direction) are optimised for the detection of the proton remnant and the scattered electron, respectively.

A schematic view of the detector is shown in Figure 2.9. Starting from the interaction vertex, the H1 detector is composed of a central [2] and a forward [3] tracking system followed by an electromagnetic [4] and a hadronic [5] Liquid Argon (LAr) calorimeter covering most of the solid angle, and a "warm" calorimeter constructed of scintillating fibers (Spaghetti Calorimeter, SpaCal) covering the backward region. The LAr calorimeter is surrounded by a superconducting cylindrical 6 m diameter coil [6] which provides a uniform magnetic field of 1.15 T. Finally, the entire detector is surrounded by the Iron yoke [10] made from iron plates which return the magnetic flux and house streamer tubes for muon identification.

In order to enlarge the geometrical acceptance of particle reconstruction scattered at small angles, several additional independent detectors have been constructed around the main H1 detector. In the forward direction there are: The Very Forward Proton Spectrometer [77] (VFPS), the Forward Proton Spectrometer [78] (FPS), the Proton Remnant Tagger [79] (PRT) and the Forward Neutron Calorimeter [80] (FNC). The energy measurements of the scattered electrons in the backward direction are performed by two Electron Taggers ( $ET6$  and  $ET40$ ) located at  $z_{ET6} = -5.4$  m and  $z_{ET40} = -40$  m<sup>4</sup>. A Photon Detector (PD) is installed at ( $z_{PD} = -101.8$  m). PD measures Bethe-Heitler processes,  $ep \rightarrow ep\gamma$ , which in coincidence with  $ET40$  is used to determine the luminosity (for details see 2.2.3 section).

In the following, only those H1 detector components which are relevant for the present charged current analysis will be described: The tracking system for the measurement of the charged particles tracks (section 2.2.1), the Liquid Argon Calorimeter for the hadronic shower energy measurement (section 2.2.2), the luminosity system (the luminosity directly enters the calculation of any physics cross section, section 2.2.3), and the Time of Flight System for the background rejection (section 2.2.4).

---

<sup>4</sup>During HERA I period there were three Electron Taggers ( $ET8$ ,  $ET33$  and  $ET44$  with locations  $z_{ET8} = -8$  m,  $z_{ET33} = -33$  m and  $z_{ET44} = -44$  m, respectively). In HERA II they have been replaced by the  $ET6$  and  $ET40$ .

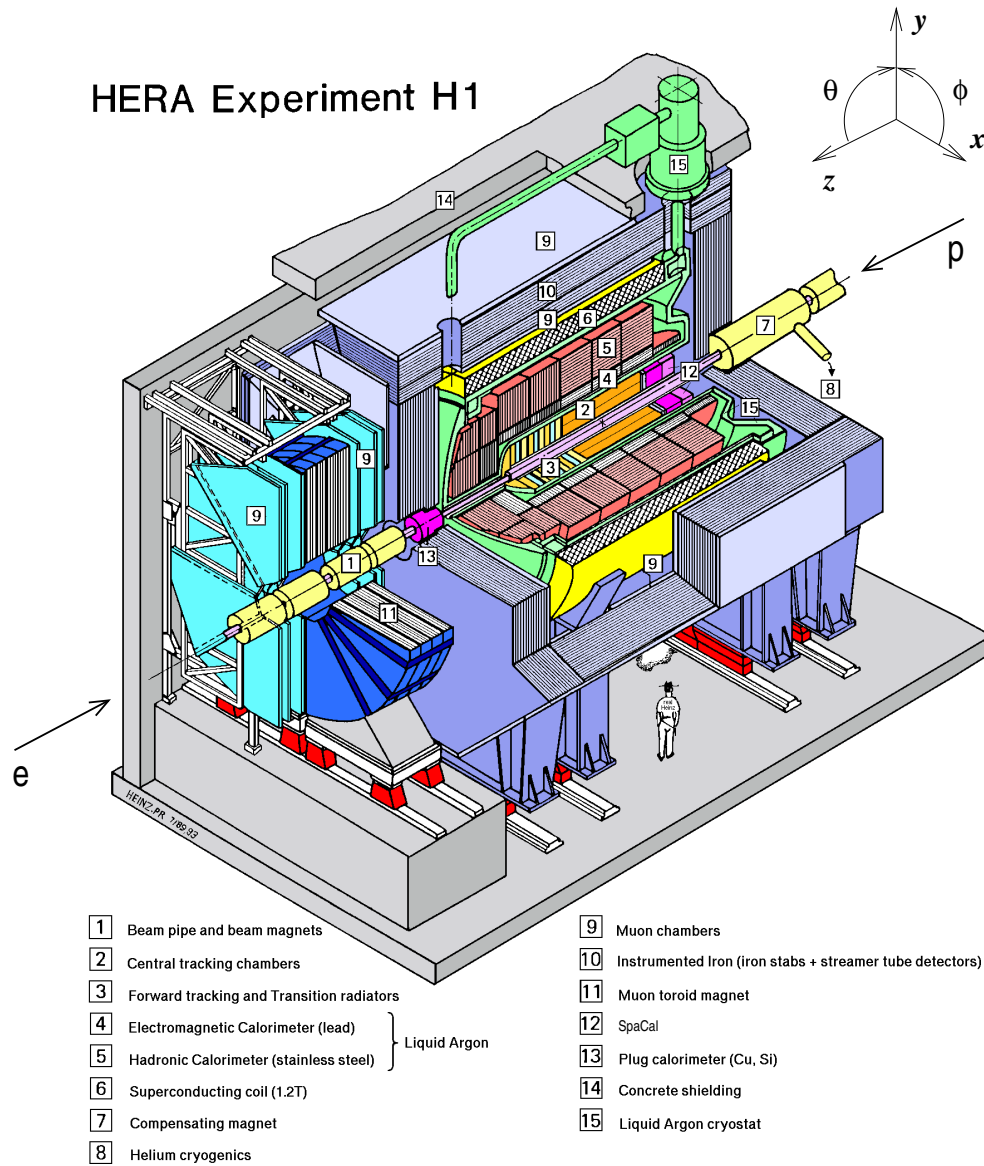


Figure 2.9: The cut-away view of the H1 detector.

### 2.2.1 Tracking System

The aim of the tracking system is to provide a precise measurement of momentum and angles of charged particles (accurate track reconstruction) and to contribute a trigger signal. For these purposes the H1 tracking system consists of various tracking devices based on the different detector technologies. The basic overview of the H1 tracking system together with its main parameters is given in Table 2.1. The side view of the system is displayed in Figure 2.10.

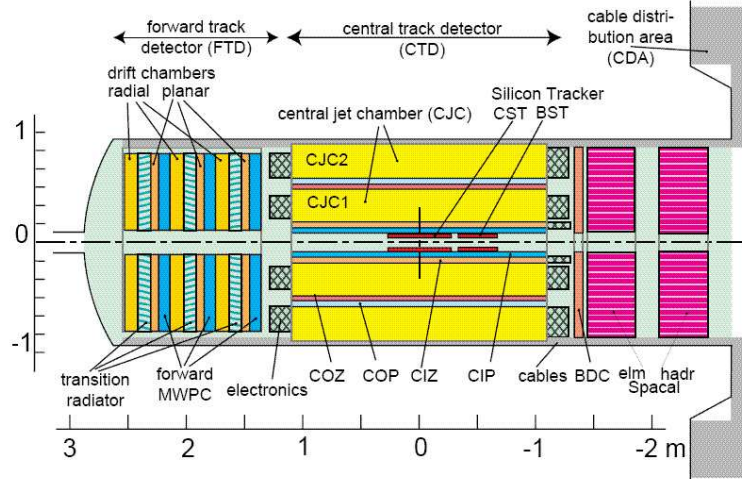


Figure 2.10: The side view of the H1 tracking system. For HERA II, CIZ and part of the CIP chamber are replaced by CIP2k.

A short description of the central and silicon tracking devices is given below, the Backward Track Detector (BTD) and Forward Track Detector (FTD) were not used in the present analysis.

#### Central Track Detector (CTD)

The CTD is an ensemble of five subdetectors each for a different particle detection purpose (see Figure 2.11). Two coaxial cylindrical jet chambers, CJC1 and CJC2, contain 30 and 60 drift cells each, with 56 sense wires in total and provide precise particle angle and momentum measurement. The wire planes are inclined with respect to the radial direction by about  $30^\circ$  which approximately corresponds to the Lorentz angle, i.e. the drift angle by which charged particles are deflected in an electric field due to the effect of the magnetic field from solenoid. As a result of the wire inclination, the ionisation produced by the charged primary particles will drift perpendicular to the wire plane, thus achieving a better track resolution.



Central Track Detector: CTD		
	angular coverage	spatial resolution
CIP2k (Central Inner Proportional Chamber)	$15^\circ < \theta < 165^\circ$	$\sigma_\phi = 5 \text{ mrad}$ $\sigma_z = 1.5 \text{ cm}$
CJC (Central Jet Chamber)		$\sigma_{r\phi} = 170 \mu\text{m}$
COP (Central Outer Proportional Chamber)		
COZ (Central Outer Z-Chamber)		$\sigma_z = 350 \mu\text{m}$
CST (Central Silicon Tracker)	$30^\circ < \theta < 150^\circ$	$\sigma_{r\phi} = 14 \mu\text{m}$
Forward Track Detector: FTD		
	angular coverage	spatial resolution
planar and radial drift chambers	$5^\circ < \theta < 25^\circ$	$\sigma_{xy} = 1 \text{ mm}$
FST (Forward Silicon Tracker)	$8^\circ < \theta < 16^\circ$	$\sigma_r = 16 \mu\text{m}$
Backward Track Detector: BTD		
	angular coverage	spatial resolution
BDC (Backward Drift Chamber)	$153^\circ < \theta < 177^\circ$	$\sigma_r < 400 \mu\text{m}$
BST (Backward Silicon Tracker)	$162^\circ < \theta < 176^\circ$	$\sigma_r = 16 \mu\text{m}$

Table 2.1: The overview of the tracking detectors composing the H1 tracking system and their main parameters.

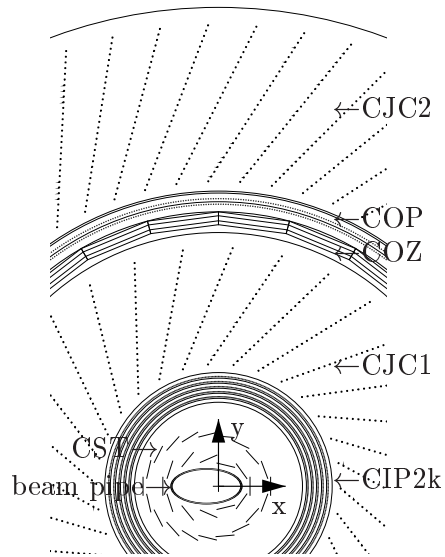


Figure 2.11: The radial view of the Central Track Detector.

The Central Inner Proportional Chamber [81], CIP2k, is a replacement of the HERA I Central Inner  $z$ -chamber (CIZ) and part of the original CIP drift chamber. CIP2k is a cylindrical multi-wire proportional chamber with a diameter  $\approx 40 \text{ cm}$  and consists of five radial layers. The chamber is positioned

between the Central Silicon Tracker (CST, see below) and the central drift chambers (Figure 2.11). The CIP2k allows fast ( $\sim 2 \mu s$ )  $z$  vertex position determination and thus efficient background rejection.

The Central Outer  $z$ -chamber, COZ, is a thin drift chamber designed to improve the track reconstruction in the  $r - z$  plane, i.e. provides a polar angle measurement. The chamber contains 4 layers of sense wires with 16 and 24 rings around the beam axis.

COP is a Multi-wire Proportional Chamber used to provide a fast trigger timing signal of the vertex position. For this purpose the chamber has a higher segmentation in the  $z$  direction with respect to the direction in  $\phi$  (60 sectors in the  $z$  direction and 8 in  $\phi$ ).

### Silicon Trackers (FST,CST,BST)

The Central Silicon Tracker [83] (CST) consists of two concentric cylindrical silicon sensor layers with 12 and 20 modules at radii of 5.75  $cm$  and 9.75  $cm$ , respectively. Each module contains six silicon sensors. Both CST layers have 35.6  $cm$  active length in the  $z$  coordinate.

CST is the closest detector to the beam pipe. The spatial resolution of CST is an order of magnitude better than the central tracker chambers (see Table 2.1). Therefore it is used to complement and improve the CTD measurement.

The Forward and Backward Silicon Trackers were not used in the present analysis.

#### *Resolution of Tracking Devices*

The momentum resolution of the tracking devices decreases with increase of the transverse momentum ( $\sigma_{p_T}/p_T \approx 0.003 p_T [GeV]$  [61]), therefore the low momentum charged particles usually are measured with a high precision.

### 2.2.2 Calorimetry

The Liquid Argon Calorimeter (LAr) covers the central and forward part of the H1 detector within the angular range of  $4^\circ \lesssim \theta \lesssim 154^\circ$ . LAr is the main detector component to measure the energy of electromagnetic and hadronic showers. The Lead-Fiber Calorimeter (SpaCal) in the present analysis is only used to complement the ToF system which sets veto conditions (described in section 2.2.4). The other two H1 detector calorimeters - Plug calorimeter ( $0.7^\circ \lesssim \theta \lesssim 3.4^\circ$ ) and the Tail Catcher (instrumented in the Iron Yoke as a part of the muon system) - are not relevant for charged current analysis and will not be described.

## Liquid Argon Calorimeter (LAr)

The liquid argon technique was chosen for the main H1 detector calorimeter due to good system stability, ease of calibration, homogeneity of response and high granularity.

The LAr calorimeter is made of wheels, each being divided in two parts<sup>5</sup>, inner electromagnetic (EM) and outer hadronic (HAD) stacks (Figure 2.12). The structure of the wheels is the following: The Backward Barrel (BBE), the Central Barrels (CB1, CB2, CB3), two Forward Barrels (FB1, FB2), the Inner Forward (IF) and the Outer Forward (OF) modules. All wheels are segmented into 8 equal octants.

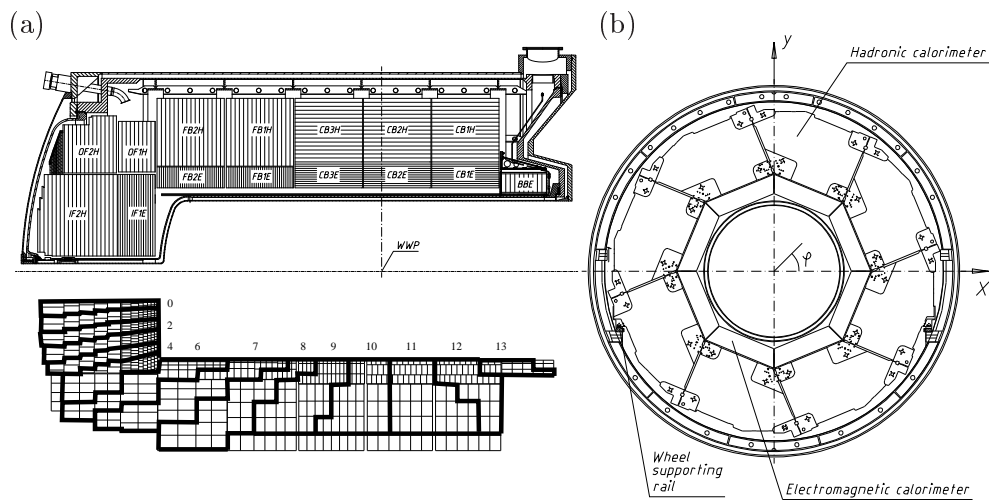


Figure 2.12: *The Liquid Argon Calorimeter: (a) longitudinal and (b) radial view.*

In order to ensure a good spatial resolution, both electromagnetic and hadronic parts of the LAr calorimeter are highly segmented, resulting in a total of 45000 read-out cells. Because electromagnetic showers are more compact than hadronic ones, the EM section has a four-fold higher segmentation than the HAD section.

LAr has a typical "sampling" calorimeter structure, i.e. EM and HAD stacks are made of "passive" absorber material and an "active" sampling medium. The EM part is made of 2.4 mm Pb absorber and 2.35 mm liquid argon as active material. The HAD cells consist of 19 mm stainless steel and a double gap of 2.4 mm liquid argon.

<sup>5</sup>All wheels except BBE have electromagnetic and hadronic parts. BBE has only an electromagnetic part.

It is typical to describe the depth of the electromagnetic (hadronic) particle shower development in the absorber material by the radiation length  $X_0$  (interaction length  $\lambda$ )<sup>6</sup>. In order to handle full shower containment ( $\sim 95\%$ ), the longitudinal segmentation of the EM part is  $20 - 30 X_0$  and  $5 - 8 \lambda$  for the HAD section.

The calorimeter is *non-compensating*, i.e. electromagnetic and hadronic showers have different energy responses (about 30% smaller for hadronic showers). To obtain the proper hadronic energy measurement (essential for charged current analyses) a special software technique [84] is used to correct for this difference.

The energy resolution of the calorimeter has been determined in test measurements and holds the values:

$$\begin{aligned} \text{for electrons and photons [85]:} \quad & \sigma_{em}/E = 12\%/\sqrt{E[\text{GeV}]}, \\ \text{for hadrons [86]:} \quad & \sigma_{had}/E = 50\%/\sqrt{E[\text{GeV}]} \end{aligned}$$

It is important to notice that the relative energy resolution of calorimeters improves with increasing energy  $E$  of the incident particle (as shown above,  $\sigma_E/E \sim 1/\sqrt{E}$ ).

#### *Noise suppression*

All measurements relying on the LAr calorimeter are strongly affected by noise originating from the electronics for signal amplification [87, 88]. In a simplified model ("white noise model", see [87]) the electronic noise  $\sigma_n$  has a linear dependence on the calorimeter cell capacity  $C_D$ :  $\sigma_n \sim C_D$ . As the electromagnetic calorimeter cells have higher capacities they suffer more from noise than the hadronic ones. There is also a clear dependence on the calorimeter region: In the high capacity (big cells) CB region the noise is higher than in the low capacity (small cells) IF region for example.

The noise level in the LAr calorimeter is measured for each of the 65000 electronic channel during electronic calibration (due to a double transmission system used in H1 there are more read-out channels than calorimeter cells, for details see [61]). The noise varies between 15 and 30 MeV per channel, depending on the calorimeter region. Cells with an energy deposit greater than  $+2 \sigma$  above the average noise level (estimated by random triggers) are removed. On the reconstruction level noise is further suppressed as described in [61] including corrections for the dead material<sup>7</sup>. On the analysis level,

<sup>6</sup>  $\lambda$  is typically an order of magnitude large than  $X_0$  for most materials. For example, for Pb  $\lambda = 193 \text{ g/cm}^2$  and  $X_0 = 6.3 \text{ g/cm}^2$ , for Fe  $\lambda = 132 \text{ g/cm}^2$  and  $X_0 = 13.8 \text{ g/cm}^2$ .

<sup>7</sup> The correction parameters due to energy loss in dead material located in front of the calorimeter (beam pipe, trackers and the inner cryostat wall) are derived from Monte Carlo simulations.

complementary noise suppression algorithms [89] and a calibration to the reconstructed energies on the particle level are applied (described in chapter 4).

In the Monte Carlo events noise is added on top of the simulated energy and the full noise suppression procedure is applied as in the real data.

### Spaghetti Calorimeter (SpaCal)

The purpose of the SpaCal calorimeter is to detect electrons scattered at low angles. In the present analysis the trigger elements provided by SpaCal are used to set veto conditions (see section 2.2.4).

SpaCal is located in the backward region of the H1 detector (see Figure 2.10), covering the region  $153^\circ \lesssim \theta \lesssim 174^\circ$  (at HERA II). Like LAr, SpaCal is a non-compensating sampling calorimeter and has electromagnetic and hadronic sections. The calorimeter is made of long thin fibers (the fiber association with spaghetti gave the name to this type of calorimeter). The incident particle is detected by the scintillation light emitted by the fibers. The detailed detector description is given in [90, 91].

### 2.2.3 Luminosity System

As mentioned in section 2.2.1, the luminosity system consists of two independent calorimeters, the Photon detector (PD) and the Electron Tagger (ET40). PD is situated at  $z_{PD} = -101.8 \text{ m}$  and measures the rate of bremsstrahlung photons from the Bethe-Heitler process [92],  $ep \rightarrow ep\gamma$ . ET40 is located at  $z_{ET40} = -40 \text{ m}$  and is used to detect scattered electrons which are deflected by the magnetic field of the HERA focussing magnets. Besides the luminosity measurement, ET is also used to study photoproduction processes (see section 1.3.1) with a limited acceptance of  $Q^2 < 0.01 \text{ GeV}^2$  and  $0.4 < y < 0.85$ .

The luminosity is determined using both detectors simultaneously, measuring the final state electron and photon produced in the Bethe-Heitler process,  $ep \rightarrow ep\gamma$  (the proton usually escapes undetected through the beam pipe). The luminosity  $L$  is calculated from the total rate of bremsstrahlung events,  $R_{total}$ , corrected for the rate in the non colliding, i.e. pilot bunches,  $R_0$  (typically 10 out of 180 bunches) [61]:

$$L = \frac{R_{total} - (I_{total}/I_0)R_0}{\sigma_{visible}}$$

Here,  $I_{total}$  and  $I_0$  are the electron beam currents in the colliding and pilot bunches, and  $\sigma_{visible}$  is the visible part of the  $ep \rightarrow ep\gamma$  process cross section (which is known theoretically with 0.5% precision).

Further details of the luminosity measurement are given in [93].

### 2.2.4 Time of Flight System (ToF)

A very efficient way of rejecting the beam associated background is to use the event time of flight. For this purpose the Time-of-Flight system (ToF) is designed. ToF is composed out of several high time resolution scintillator detectors connected to photomultipliers.

The ToF system [94] is a set of the following devices (see Figure 2.13):

<b>FToF</b>	( $z \approx 7.0$ m)	Forward ToF installed within the forward muon system,
<b>PToF</b>	( $z \approx 5.3$ m)	ToF installed behind the Plug calorimeter,
<b>FIT</b>	( $z \approx 2.7$ m)	Forward Interaction Timing system mounted behind the forward tracker,
<b>SToF</b>	( $z \approx -2.4$ m)	installed just before the hadronic SpaCal section,
<b>BToF</b>	( $z \approx -3.3$ m)	Backward ToF mounted after SpaCal,
<b>VETOWALL</b>	( $z \approx -(6.5 \div 8.1)$ m)	several small veto counters mounted close to the beam pipe.

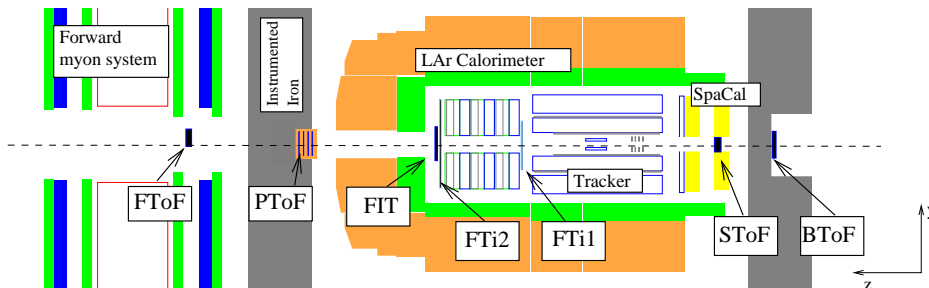


Figure 2.13: Schematic view showing the various locations of the ToF sub-detectors. VETOWALL is outside of the visible range to the right side ("up-stream" of the proton beam).

## 2.3 H1 Trigger System

The bunch crossing (BC) frequency at HERA is approximately 10 MHz at the H1 interaction point. Not every bunch collision yields a reaction leading to secondary particles detectable in the H1 detector, therefore the raw data rate usually reaches a few tens of kHz. The rates of interesting physics events ( $ep$  collisions) is orders of magnitude smaller - ranging from  $\sim 30$  Hz for the tagged photoproduction to the production of  $W$ 's where about one events is expected in few days. The background is dominated by proton interactions with residual gas nuclei (beam gas interactions) and cosmic events.

The aim of the H1 Trigger System is a fast and efficient separation of real physics events from the dominating background and a proper accommodation of the  $ep$  collisions within a limited H1 bandwidth. For these purposes the trigger system consists of four separate levels, each consecutively filtering incoming data and making more and more complex decisions. The filtered data from one level are sent to the next level until the manageable rate for the H1 data acquisition system ( $\approx 40\text{ Hz}$ ) is reached after the final level (see Figure 2.14).

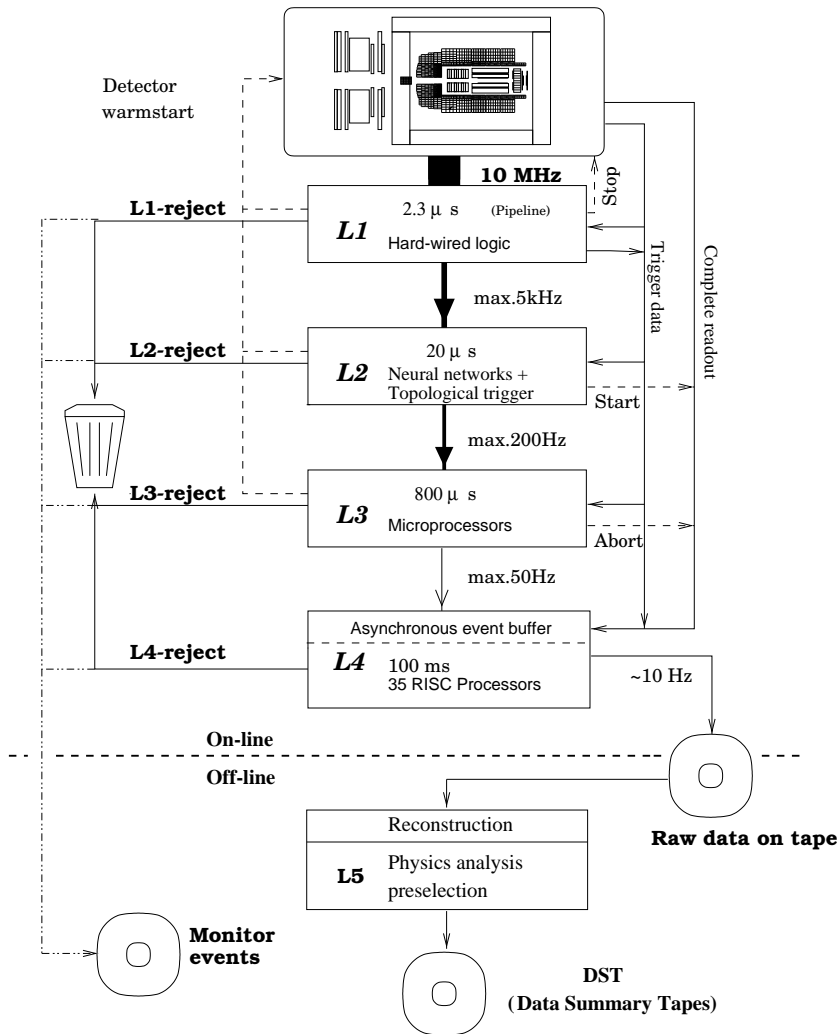


Figure 2.14: The H1 Trigger System.

### 2.3.1 The First Trigger Level (L1)

The decision to keep or reject an event at the first trigger level (L1) is based on the information arriving from all subdetectors in the form of *trigger elements*. The trigger elements from the subdetectors are passed in dead time free pipelines (the pipelines length varies between 27 and 35 BC's deep depending on the subdetector) to the Central Trigger Logic (CTL). The CTL coordinates and synchronises the data stream from all subdetectors, combines these trigger elements into so-called *subtriggers* and makes a decision to keep event ("L1keep") if at least one subtrigger is set<sup>8</sup>. If the event was kept, the pipelines are stopped and the "dead time" (time when the detector cannot continue to take data) starts.

A description of relevant trigger elements for the charged current analysis provided by the tracker system, LAr calorimeter and ToF system is given below.

The Fast Tracking Trigger (FTT) [95,96] has been recently integrated into the H1 trigger system (replacing the old DCr $\phi$  trigger). FTT uses partial read-out of the CJC1 and CJC2 chambers for flexible topological selectivity and provides L1, L2 and L3 trigger elements. FTT was just in the commissioning phase during this analysis data taking period and will not be discussed here.

#### Tracking System Trigger Elements

The tracking chambers provided trigger elements used in this analysis are summarised in Table 2.2, details can be found in [97].

name	short description
CIP_sig	significance in the central part of the interaction vertex determined from the tracks
CIP_T0	a timing signal set if there is at least one central track in coincidence with the interaction time
CIP_MUL	the multiplicity of the tracks

Table 2.2: *List of tracking system trigger elements used in the present analysis for the charged current event triggering.*

The trigger elements of the tracking system are also used to supplement veto conditions, i.e. to reject non-*ep* background events. In the present analysis the following veto conditions are used: CIP\_MUL>7 (more than 1000 tracks in the event) and CIP\_sig==0 (no central tracks found which could be used to determine the event interaction vertex).

<sup>8</sup>Some subtriggers may have a *prescale*  $p$  which means that this trigger will be ignored by CTL until it has been set  $p$  times.



### LAr Trigger Elements

The LAr calorimeter trigger [61] is the main trigger for all high  $Q^2$  physics analyses. The LAr energy measurement is built from the signals provided by 45000 LAr cells (see section 2.2.2). Subset of these signals are added to so-called *trigger cells* (TC) and added further to *trigger towers* (TT) with a projective geometry. TTs are used to build even coarser granularity *big towers* (BT) (the distribution of  $\theta$  of BTs is shown in Figure 2.12), each of them split in an electromagnetic (EM) and a hadronic (HAD) part. The signals from the BTs (which are still analog) are digitized with fast ADCs (FADC, fast analog to digital converter) and fed into digital summing electronics which are finally discriminated using programmable threshold functions. The derived trigger elements (TE) are sent to CTL. For details refer to [98].

The LAr trigger elements used in the charged current analysis are summarised in Table 2.3.

name	short description
LAr_Etmiss	the transverse momentum in the calorimeter, defined as: $\sqrt{(\sum_i P_{x,i})^2 + (\sum_i P_{y,i})^2}$ where the sum runs over the $i$ BT's and the momenta is calculated from the energies and angles in the BT $i$ : $P_{x,i} = E_i \sin \theta_i \cos \phi_i$ $P_{y,i} = E_i \sin \theta_i \sin \phi_i$
LAr_IF	the energy sum of the BT's belonging to the IF region
LAr_electron_1	set if the TT energy is above a certain threshold in the electromagnetic part ( $\sim 6$ GeV)
LAr_T0	an "OR" of the TT timing signals $T_0$ determined by a constant fraction discriminator technique

Table 2.3: *List of trigger elements provided by LAr calorimeter trigger and used in the present analysis for the charged current event triggering.*

### ToF Trigger Elements (Veto conditions)

The trigger elements or *veto conditions* provided by the ToF system are applied to most of the subtriggers. All ToF subsystems provide their trigger elements in three time windows around the interaction time  $\sim [-4; +16$  ns]:

- BG** background window (set by particles arriving earlier than particles from the interaction point),
- IA** interaction window (set by particles from the interaction point),
- GL** global window (set by particles arriving later than the particles from the interaction point).

The veto conditions are combinations of signals from the ToF subsystem and from the trigger time window. For example, the signal provided by the Forward Interaction Timing system in the interaction window would be FIT\_IA.

In addition, there are veto conditions set by the ToF system together with some other subdetector. The additional condition used in this analysis is:

**SPCLh\_AToF\_E\_1** set when the total SpaCal hadronic "out of time" energy (AToF) is greater than  $0.6 \text{ GeV}$ .

### 2.3.2 The Second Trigger Level (L2)

Two trigger systems, the Neural Network Trigger (L2NN) [99] and the Topological Trigger (L2TT, [100]) form the second trigger level. At level 2, the full L1 information from all subdetectors is available. Since the time within which the L2 decision has to be taken is  $20 \mu\text{s}$ , there is enough time to exploit the correlations between the various subdetectors.

The L2NN system consists of 13 independent neural networks, each of them with the possibility to have up to 64 input neurons, 64 hidden and 1 output neuron. Each network is trained to recognise a specific physics channel making use of its specific patterns in the detector.

The short introduction to neural networks and technical details of the L2NN trigger system are given in section 2.4. Examples of the network training procedure applied to the main inclusive DIS subtriggers in order to tighten the conditions at HERA II are also described in section 2.4.

### 2.3.3 The Third Trigger Level (L3)

The third trigger level was not used during HERA I period neither at the HERA II period up to the end of 2005. The Fast Tracking Trigger (FTT level 3) has been only recently commissioned.

### 2.3.4 The Fourth/Fifth Trigger Levels (L4/5)

The L4/5 trigger level makes the event reconstruction from the complete readout of the event information (the readout starts with "L2 keep"). Event parameters (tracks, clusters, vertex, time of the interaction) are reconstructed by the H1 software reconstruction algorithm (H1REC).

The events are classified into certain physics classes by so-called L4 filters [101] (or rejected if they do not fit in any of the existing classes), and are written to the *Production Output Tapes*, POT, ( $\sim 100 \text{ kb}$  per event). A subset of the POT information is duplicated to the *Data Summary Tapes* (DST,  $\sim 10 \text{ kb}$  per event) which is usually sufficient for most of the data analyses.

## 2.4 Neural Networks for DIS Inclusive Event Triggering

The H1 Level 2 trigger provides an early opportunity for event "pattern recognition" based on information from all subdetectors. Since 1996, the L2NN trigger has been successfully used to trigger various physics channels (mostly exclusive channels, like heavy vector meson production, e.g.  $ep \rightarrow epJ/\psi$  or Deeply Virtual Compton Scattering  $DVCS$ ,  $ep \rightarrow e\gamma p$ ) and to significantly reduce the corresponding physics trigger rates. An example of the neural network application for elastic photoproduction of  $J/\psi$  vector mesons can be found in [102, 103].

The performed studies have shown that L2NN can be successfully used to trigger also the inclusive physics channels being used for the ongoing data taking by the H1 experiment.

In this chapter an overview of the L2 neural networks (as introduced in section 2.3.2) trained to recognise DIS inclusive interactions is presented. First, a short introduction<sup>9</sup> to neural networks (NN) is given. Then, the level 2 neural network trigger will be described. The applications of networks for inclusive events (charged and neutral current, multi-electrons, isolated leptons) are presented in the last section.

### 2.4.1 Introduction to Neural Networks

A neural network (or more precisely Artificial Neural Network, ANN) consists of elementary units called *neurons* (or nodes) in association with the nerve cells of the human brain. Regardless of how complicated the real biological neuron may be, a simplified abstraction can be simulated by a simple mathematical model (Figure 2.15 (a)): A neuron  $i$  receives a certain number of inputs, each with a weight  $w_i$ . The neuron  $i$  computes a non-linear function  $f(a)$  from the weighted sum of its inputs:

$$y_i = f(\sum_i x_i w_i - b) \quad (2.8)$$

Here,  $b$  is the neuron threshold value which is compared with the summed result of the weighted inputs, i.e. the "activation" of the node ( $b$  is sometimes also called activation threshold). The function  $f$  is a *threshold function*, which is usually taken as

$$f(a) = \frac{1}{1 + e^{-a}} \quad (2.9)$$

---

<sup>9</sup>The more detailed introduction to neural networks can be found in e.g [104].

Using this basic building block, networks of neurons can be built up. There are several possible architectures for neural networks. One of the most popular (also well suitable for pattern recognition problems) is the *multilayer feed-forward architecture*. The neurons in the feed-forward networks are organised in layers, passing the information from an input layer to an output layer of neurons.

The construction of the neural network is performed in the following way: Each neuron in the layer receives the inputs from all neurons in the previous layer and sends its output to all neurons of the next layer. A symbolic view of such a net is shown in Figure 2.15 (b). The network shown has three layers: One *input*, one *hidden* and one *output* layer. When neurons in the *hidden* layer have received all inputs from the *input* layer, they perform the computation of the function  $f$  (equation 2.9) and provide their outputs  $y_i$  to each node of the *output* layer. The single neuron of the *output* layer computes the final network output, a single number in the range  $[0, 1]$ .

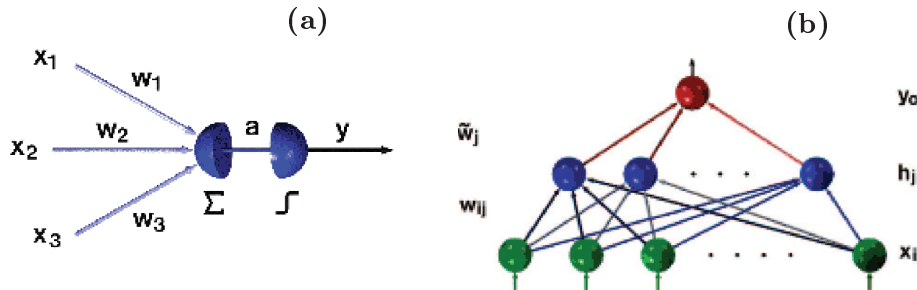


Figure 2.15: *Symbolic presentation of (a) the neural network elementary unit - neuron; (b) the feed forward neural network with one hidden layer. For explanation of symbols see text.*

The geometrical interpretation of such a network is quite simple: If one imagines the space formed by the network inputs ("trigger" space in this case), then each neuron of the hidden layer defines a hyperplane in this space where the normal vector of the hyperplane is given by the vector of weights  $w_i$ . The distance to the origin is given by the threshold  $b$ . Several such hyperplanes divide the trigger space into two arbitrarily shaped regions: "signal" and "background"<sup>10</sup>. The final output of the network (given by the single output neuron) is the separating function in trigger space.

The idea of the network training is finding the optimal function for the best two class-separation. For this purpose a set of example patterns is required with associated target values for the output ("1" for signal and "0" for back-

<sup>10</sup>Generally, there could be more than two classes required to distinguish the signal from the background, but such problems will not be discussed here.

ground in the simple case). The way of training by adopting to classified examples is called *supervised learning*.

The difference between the correct answer  $\nu$  and the network output  $y$  can be described by an error function  $E$ , given by:

$$E = \frac{1}{2} \sum_i (\nu_i - y_i)^2 \quad (2.10)$$

The randomly initialised network weights can be adjusted in a minimisation procedure using gradient descent of the error function

$$w \rightarrow w - \epsilon \frac{\partial E}{\partial w} \quad (2.11)$$

Here,  $\epsilon$  is the step size (or *learning rate*) which describes the dynamics of the changing of weights. Starting from the output layer, the derivative of error function  $\frac{\partial E}{\partial w}$  is derived for each layer and propagated "backwards" through the network down to the input layer. This is the basic idea of the *back propagation algorithm* [105].

In order to control the network performance, the usual procedure is to separate the input data into three sets: *training*, *selection* and *test*<sup>11</sup>. After the network is trained with the training sample, the independent selection set allows to find an optimal network performance between several trainings with different training parameters. The final independent test sample is necessary to test the "true" performance of the selected network. In this way the network response to unknown patterns is tested (*generalisation*).

As the standard evaluation of the neural network performance it is common to discuss the signal efficiency versus background rejection (more explanations are given in section 2.4.3).

A more detailed description of the network training procedure is given in [103].

## 2.4.2 H1 Level 2 Neural Network Trigger (L2NN)

Basic arguments of using neural networks in the H1 trigger system are:

- to exploit multidimensional correlations between various trigger quantities from all subdetectors available at the second trigger level,
- the speed performance of the networks which use parallel hardware architecture and thus provide a clear advantage for a limited trigger decision time.

---

<sup>11</sup>The typical splitting of the known set of example patterns into training, selection and testing is 50%-25%-25%.

There are three algorithms available in the L2NN: *Feed Forward Networks* (FFN), *Background encapsulators* and *Constructed Nets*. FFNs are the networks with a three-layer structure (one input, output and one hidden layer) and with a maximum of 64 nodes each. Background encapsulators are nets which encapsulate the background events according to its specifics and are used for "unknown physics" to trigger. Constructed Nets are used for simple applications such as topological correlations. In the following, the term "neural network" will refer to the FFN type networks.

## L2 Trigger Hardware

L2NN is a set of 13 neural networks presently implemented on parallel computers (CNAPS from Adaptive Solutions [106]). Each network has its own data preprocessing module *Data Distribution Board* (DDB), which provides suitably preprocessed input data to the CNAPS board and transfers the network output to the Central Trigger Logic (CTL). The layout of the L2NN hardware is shown in Figure 2.16.

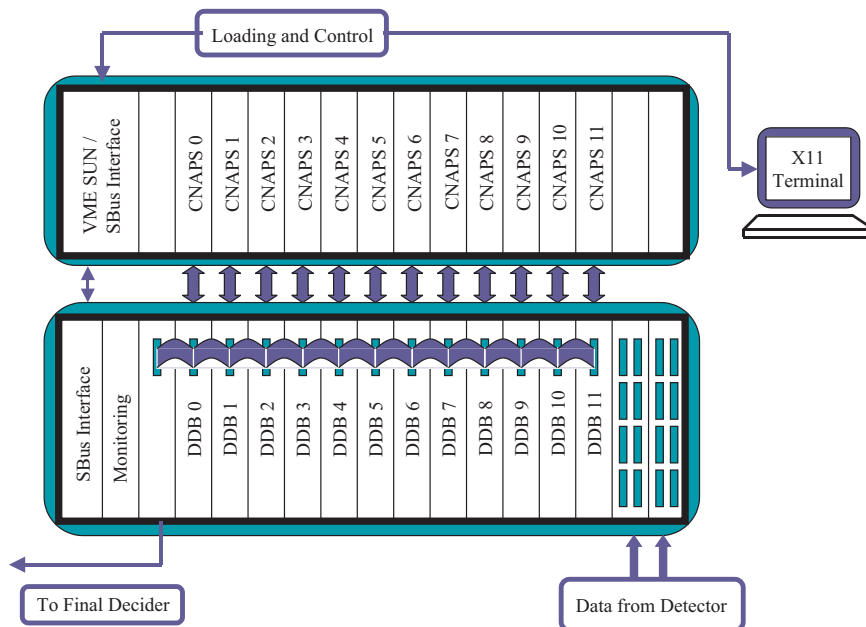


Figure 2.16: Layout of the H1 Neural Network Trigger (L2NN) system. The processors of each network (CNAPS) are associated with a preprocessing module (DDB) which prepares the input quantities for the neural network.

*Data Distribution Boards (DDB)*

After special receiver cards collect the incoming trigger information from all subdetectors, the information is distributed further via a 128 *bit* wide L2 bus to the Data Distribution Boards (DDBs). Each DDB "selects" the relevant information from the L2 data stream and also performs basic preprocessing operations such as bit summing, for example. The DDB can provide up to 64 8 *bit* inputs to the associated CNAPS board.

*CNAPS boards*

The array of CNAPS boards is located in a VME crate with 8 *bit* wide input and output buses used for the data transfer. Each of the boards is equipped with one CNAPS chip which defines the size of the processable FFN to a  $64 \times 64 \times 1$  (64 inputs, 64 nodes in hidden layer and single output node) architecture<sup>12</sup>. This type of net requires about 8  $\mu s$  for the decision calculation. A complete technical description of CNAPS can be found in [99, 108].

The strategy of network usage is the following: Each of the networks is trained for a specific physics channel and is associated with one (or several) level 1 subtriggers which are found to be efficient for triggering the given physics channel but whose trigger rates exceed the allowed bandwidth. The additional L2NN condition is used to reduce the excess rate for the given subtrigger without losing too many physics events.

**2.4.3 Training of Neural Networks and their Performance**

In this thesis the focus is drawn to networks trained to reduce the rates of two main DIS inclusive subtriggers, S67 and S77. Both subtriggers are based on the calorimetric information and are used in the charged current analysis (definitions of these subtriggers are given in section 5.1.3). The CC events used for the training were selected similarly to the analysis described in chapter 5. The main trigger element of S67 is *LAr\_electron\_1* (see section 5.1.3). This subtrigger is also very efficient for the triggering of other physics channels, such as charged current, rare processes with isolated electrons in the final state, etc.

After the HERA upgrade and the increase of the instantaneous luminosity (equation 2.1), the high rates of the subtriggers S67 and S77 became critical. The rates of S67 and S77 as function of instantaneous luminosity over the whole year 2005 are shown in Figure 2.17. As can be seen from these figures,

---

<sup>12</sup>The network design is motivated according to the Kolmogorov [107] rule saying that any multi layer FFN can be represented by the FFN with a single hidden layer.

both subtriggers can reach rates of 10  $Hz$  for certain beam conditions. In these conditions a large part of the H1 bandwidth is consumed<sup>13</sup> and other physics triggers are prevented to run efficiently. The prescaling scenario cannot be applied to these subtriggers as the selection of the deep inelastic  $e^\pm p$  reactions are the prime goal of the H1 physics output (in H1 jargon also called "holy cow" triggers). The Level 2 neural networks appeared to be an attractive solution of the problem.

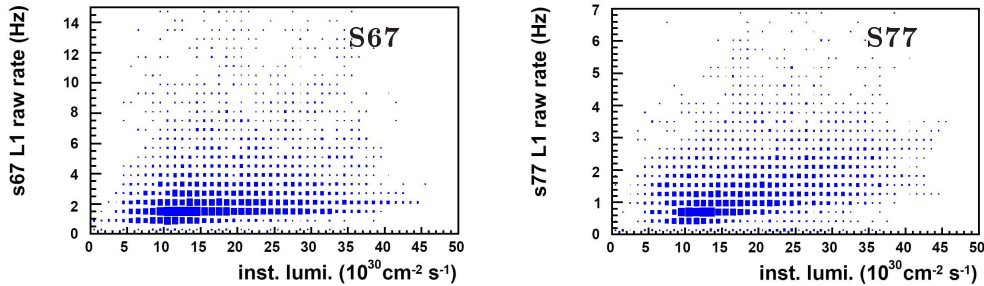


Figure 2.17: Rates of subtriggers 67 and 77 versus the instantaneous luminosity in the year 2005.

### Combined Networks for Inclusive Physics Channels

To train the neural networks for rate reduction of the subtriggers S67 and S77 (one network for each subtrigger) it is necessary to select "signal" and "background" samples first. The signal samples should be composed of the physics channels which are triggered by S67 and S77, respectively. The concerned physics reactions are: charged current, neutral current, multi lepton events<sup>14</sup>, and events with isolated electrons in the final state<sup>15</sup>.

In order to prepare training samples for the networks, one has to deal with the problem of very small signal sample of the rare multi lepton and isolated electron processes (approximately few hundred in total over the whole year 2005) which is barely sufficient to train networks with a complex input layer as required for high efficiency. A good approximation which was chosen for the given conditions was to offer the rare events more frequently in the network training (i.e. high weights were applied to these events).

<sup>13</sup>The H1 bandwidth is limited by the front-end readout time, the L4 computing power and the maximum data logging rate.

<sup>14</sup>Events with multi leptons (usually 2) in the final state originate mainly from photon-photon interactions: Photons radiated from the incident electron and proton interact to produce a pair of leptons,  $\gamma\gamma \rightarrow l^+l^-$  (see section 1.3.2 or [109]).

<sup>15</sup>Within the Standard Model isolated leptons in the final state and missing transverse momentum are expected mainly due to W boson production with a subsequent leptonic decay [110, 111].



As all physics channels rely on similar detector information (tracking and calorimetric measurements), same inputs were chosen for the S67 and S77 networks:

*energy in LAr calorimeter*

eifq0-3	quadrants of the inner forward region
efbq0-3	quadrants of the forward region
ecbq0-3	quadrants of the central region
laret/larx/lary	transverse energy, $x$ and $y$ components (see Table 2.3)

*tracking system*

fttmulti/fttmultc	number of tracks in different $p_T$ ranges (FTT)
cipcq0-3	number of tracks in CIP quadrants (central region)
cipbtot	number of tracks in backward CIP region

Some examples of the input quantities for the combined signal and background events are shown in Figure 2.18.

The chosen network architecture with the given 22 input quantities is  $22 \times 5 \times 1$ , where 5 corresponds the number of nodes in the hidden layer and 1 is the output node.

The results of the S77 network training (with the four discussed physics classes used as signal in the training) are presented in Figure 2.19 where the output distributions of the training and test events are shown. The plots on the left column correspond the training sample (upper for signal, bottom for background), the plots on the right column correspond to results of the independent testing sample. The result of the network, i.e. the plot of signal efficiency versus background rejection (Figure 2.20) shows very good results for both, training and testing samples (the network performance is slightly worse for the testing events, as expected). From these output plots an optimal cut (also called "working point") can be chosen, i.e. the value defining the decision to keep or reject the event. The cut corresponds the value  $x$  in the plots of Figure 2.19, i.e. only the events in the right side of this cut are kept. Similarly, the cut corresponds the value  $y$  in the plot of Figure 2.20, i.e. the event is kept if  $y > y_{cut}$ .

The optimal working point of the network was chosen at 0.02 yielding an efficiency of 99.89% and 75% background rejection. This means that 99.89% of physics events are triggered by the S77 network and 75% of the background events are rejected for the chosen threshold.

The trained combined networks for the subtrigger S67 and S77 rate reduction are presently operated at the H1 second level triggers system.

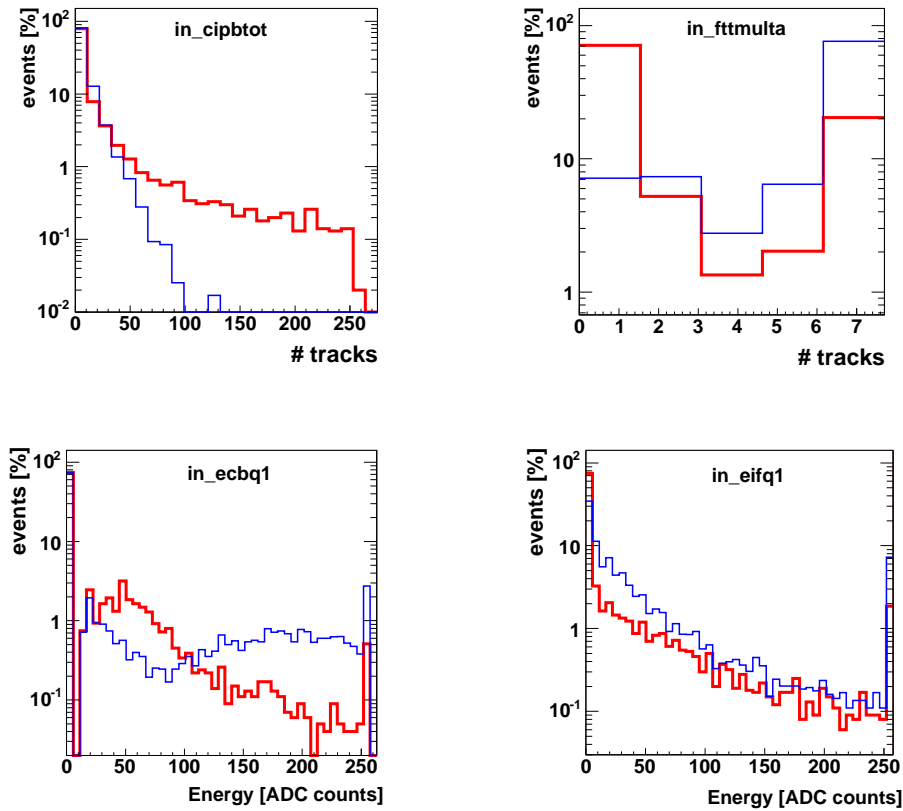


Figure 2.18: *Input distributions of cipbtot, ffmulta, ecbq1 and eifq1 (for meaning see text) of combined signal (charged current, neutral current, isolated electron and multi lepton events) and background events. The signal is shown as a thin line, background events correspond bold line. The scale used in for ecbq1 and eifq1 is  $1 \text{ GeV} \approx 5 \text{ ADC counts}$ .*

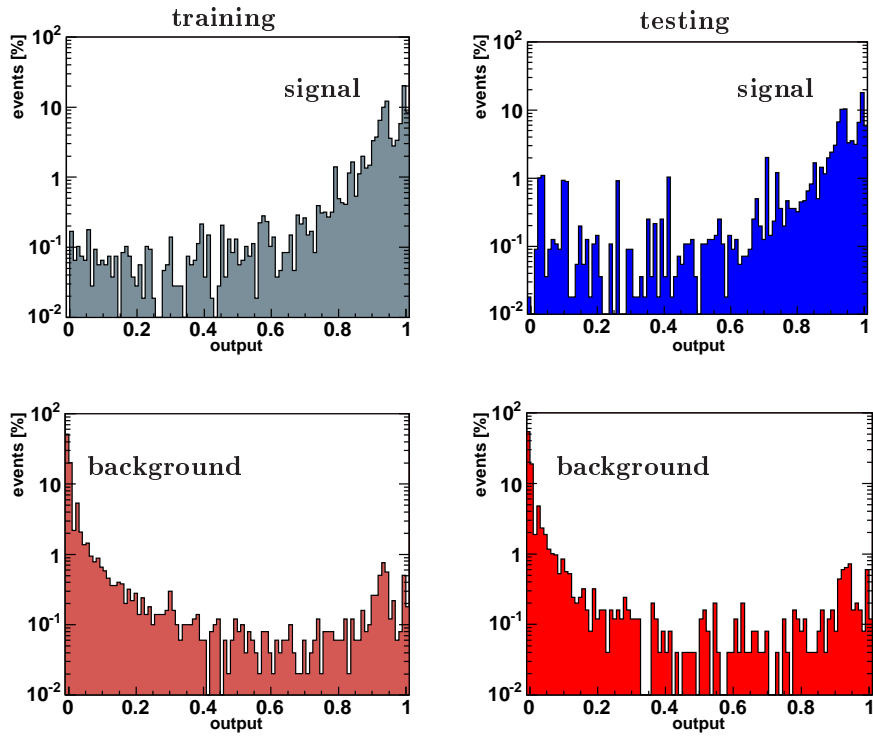


Figure 2.19: Output of  $S77$  neural network trained for combined DIS inclusive event classes. The plots on the left column correspond to the training sample, the right column represents the testing sample. The network output is in the range of  $[0 - 1]$  where 1 (0) corresponds to the signal (background).

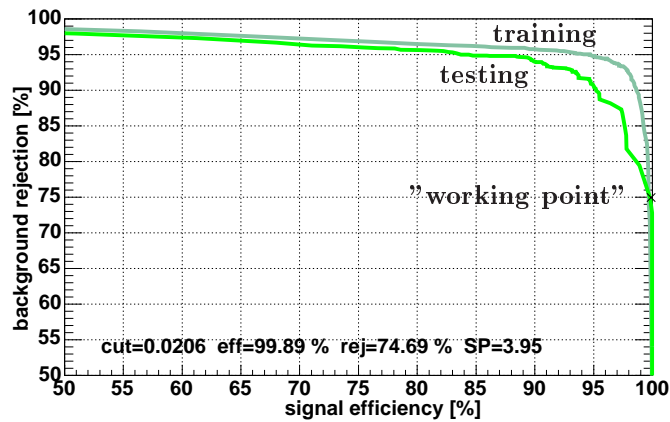


Figure 2.20: Efficiency versus rejection graph of  $S77$  neural network trained for combined DIS inclusive event classes. The results of training and testing are indicated in the plot. The optimal working point (corresponding values are given in plot) is shown as a cross.



## Chapter 3

# Reconstruction of Kinematic Quantities

As mentioned in chapter 1.1, two of the three inclusive kinematic variables are sufficient to describe inclusive DIS processes, e.g.  $x$  and  $Q^2$ .

DIS kinematics can be determined from the scattered electron or the hadronic final state (HFS) observed in the detector. The HFS is formed by the hadrons resulting from the  $e - q$  interaction and the proton remnant. Unlike neutral currents where the scattered electron information can be used, in the charged current case kinematic variables can only be reconstructed from the hadronic final state.

In the present analysis the neutral current events are used to calibrate the hadronic energy measured in the LAr calorimeter ("hadronic calibration") and to determine the efficiencies of the CC selection requirements. Therefore, the relevant NC event kinematic reconstruction methods are introduced here as well.

The kinematic reconstruction methods are described in the following order: First, the "electron" method where the kinematics are determined from the scattered electron alone, second, the "hadron" method where only the hadronic information is used, and finally, the " $\Sigma$ " and "double angle" methods where both, hadron and electron information is used.

All expressions below are given in the ultrarelativistic limit, i.e. the particle masses are neglected.

### Electron method

The event kinematics in this method is determined from the scattered electron alone. This was traditionally the method used in the fixed target experiments, e.g. R. Hofstadter [2], SLAC experiments [3, 4], etc.:

$$Q_e^2 = 4E_e E_e' \cos^2 \frac{\theta_e}{2} \quad y_e = 1 - \frac{E_e'}{2E_e} (1 - \cos \theta_e) \quad x_e = \frac{Q_e^2}{s y_e} \quad (3.1)$$

Here,  $E_e'$  and  $\theta_e$  are the energy and polar angle of the scattered electron,  $s$  is the electron-proton center-of-mass energy squared.

As can be seen from the formulae above, the variable  $y_e$  at large angles  $\theta_e$  (the electron is scattered backwards) depends mainly on the scattered electron energy  $E_e'$ , whereas  $Q_e^2$  depends mainly on the scattered electron angle  $\theta_e$ . This leads to a high resolution in  $x$  at high  $y$  but the resolution rapidly decreases towards low  $y$  (however, the  $Q^2$  resolution is very good over the full kinematic range).

### Hadron method

Using the method which was introduced by Jacquet-Blondel [112], the kinematic variables can be determined from the hadronic final state particles:

$$y_h = \frac{1}{2E_e} \sum_h (E_h - p_{z,h}) \quad Q_h^2 = \frac{p_{T,h}^2}{1 - y_h} \quad x_h = \frac{Q_h^2}{s y_h} \quad (3.2)$$

Here,  $E_h$  and  $p_{z,h}$  are the energy and longitudinal momentum components of particle  $h$  in the hadronic final state,  $E_e$  is the energy of the incoming electron.  $p_{T,h}$  is the transverse momentum of the hadronic final state, defined as:

$$p_{T,h} = \sqrt{\left( \sum_h p_{x,h} \right)^2 + \left( \sum_h p_{y,h} \right)^2} \quad (3.3)$$

$p_{x,h}$  and  $p_{y,h}$  are momentum components of particle  $h$  in the transverse plane, the sum is over all particles except the scattered electron.

As can be seen from the formula 3.2, the resolution in  $Q^2$  (and consequently in  $x$ ) is severely affected by the term  $1/(1 - y)$ , i.e. the resolution of both variables deteriorates in the high  $y$  region.

### $\Sigma$ method

Another method exploiting the information of the particles in the hadronic final state and the scattered electron is the so-called  $\Sigma$  method [113]. The variable  $y$  is expressed here as in the hadron method with the beam energy obtained from the transverse momentum balance in the event:

$$p_T^{in} = p_T^{out} = E_e' \sin \theta_e + \sum_h (E_h \sin \theta_h), \quad (3.4)$$

where the sum runs over all hadronic final state particles. The difference of the energy and longitudinal momentum in an ideal detector should be equal to  $2E_e$ , thus from energy and momentum conservation one obtains:

$$2E_e = E'_e - p_{z,e} + \sum_h (E_h - p_{z,h}) = E'_e(1 - \cos \theta_e) + \sum_h (E_h - p_{z,h}) \quad (3.5)$$

Using the same expression for the variable  $y$  as in the "hadron" method, one can deduce:

$$y_\Sigma = \frac{\sum_h (E_h - p_{z,h})}{\sum_h (E_h - p_{z,h}) + E'_e(1 - \cos \theta_e)} \quad (3.6)$$

The quantity  $\sum_h (E_h - p_{z,h})$  sometimes is called " $\Sigma$ ". Then

$$y_\Sigma = \frac{\Sigma}{\Sigma + E'_e(1 - \cos \theta_e)} \quad (3.7)$$

The other kinematic quantities in this method are given by:

$$Q_\Sigma^2 = \frac{P_{T,e}^2}{1 - y_\Sigma} = \frac{E_e'^2 \sin^2 \theta}{1 - y_\Sigma} \quad x_\Sigma = \frac{Q_\Sigma^2}{sy_\Sigma} \quad (3.8)$$

Advantages of the  $\Sigma$  method are the small sensitivity to particle losses in the beam pipe and the small sensitivity to the initial state photon radiation, ISR (as explained in section 1.2.3, the photon radiated of the electron leads to a smaller center-of-mass energy squared  $s$  and, accordingly, to different event kinematics).

### Double Angle method (DA)

The DA method is a kinematic reconstruction method for neutral current events. The variables are reconstructed only from the polar angle of the scattered electron ( $\theta_e$ ) and the hadronic final state ( $\gamma_h$ ):

$$y_{DA} = \frac{\sin \theta_e (1 - \cos \gamma_h)}{\sin \gamma_h + \sin \theta_e - \sin(\theta_e + \gamma_h)} \quad Q_{DA}^2 = \frac{4E_e'^2 \sin \gamma_h (1 + \cos \theta_e)}{\sin \gamma_h + \sin \theta_e - \sin(\theta_e + \gamma_h)}$$

$$x_{DA} = \frac{Q_{DA}^2}{sy_{DA}} \quad (3.9)$$

The hadronic polar angle  $\gamma_h$  is given by:

$$\tan \frac{\gamma_h}{2} = \sum_h \frac{E_h - p_{z,h}}{p_{T,h}}$$

The polar angle of the scattered electron  $\theta_e$  is expressed as:

$$\tan \frac{\theta_e}{2} = \frac{E'_e - p_{z,e}}{p_{T,e}} \quad (3.10)$$

The transverse momentum using the double angle method ( $p_{T,da}$ ) is then given by:

$$p_{T,da} = \frac{2E_e}{\tan \frac{\gamma_h}{2} + \tan \frac{\theta_e}{2}} \quad (3.11)$$

Since the DA method is independent of the calorimetric energy measurement and uses only  $\theta_e$  and  $\gamma_h$ , it can be used to calculate the expected LAr energies ("hadronic calibration"). For details see chapter 4.



## Chapter 4

# Neutral Current Events for the Charged Current Analysis

In the low  $Q^2$  region the charged current interactions are suppressed by the propagator mass ( $\sim [M_W^2/(Q^2 + M_W^2)]^2$ , see equation 1.38). In contrast to the purely weak CC reactions, the neutral current cross section exceeds the CC cross section by more than two orders of magnitude due to the dominant photon exchange ( $\sim 1/Q^4$ ) at low  $Q^2$ .

The scattered electron in NC interactions is identified very efficiently and reconstructed with high precision (e.g. the electron cluster identification inefficiency is below 0.5% in the central LAr calorimeter region [114]). Therefore, the neutral current events provide the possibility to perform detailed detector quality checks. NC events are used in the CC analysis for several purposes which are listed below:

- to calibrate the hadronic energy,
- to determine the distribution of the  $ep$  interaction vertex which is used to adjust the vertex distribution of the CC simulated events,
- to produce so-called *pseudo charged current* events which are used to determine the efficiencies of the CC selection requirements.

The NC events used in this analysis were selected in [115] and correspond to the same  $e^+p$  period as considered in this thesis. One of the detector stability checks which was performed with the selected NC events is illustrated in Figure 4.1. The figure shows the number of NC events per  $1 \text{ nb}^{-1}$  of luminosity ("event yield") as function of time (or, more precisely, so-called run numbers, see explanation in chapter 5.1). As seen from the Figure 4.1, the NC event yield is constant throughout the whole  $e^+p$  data taking period.

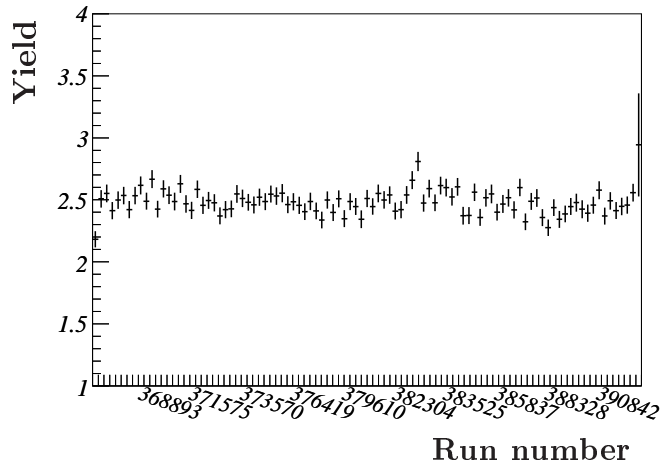


Figure 4.1: Number of neutral current events per  $1 \text{ nb}^{-1}$  (yield) as function of the run number for the  $e^+p$  data taken in the years 2003-04. The selection of events is described in [115].

## 4.1 Hadronic Energy Calibration

As explained in section 2.2.2, the hadronic energy measurement in the LAr calorimeter can be strongly affected by the noise originating from the preamplifier electronics. The noise suppression is particularly important for the charged current analysis due to sensitivity of the variable  $y_h$  to noise: In the hadron method,  $y_h$  is directly proportional to the difference of the energy in the hadronic final state (HFS) and the longitudinal momentum (see equation 3.2). Therefore, even a small fraction of noise misidentified as true energy can strongly effect the  $y_h$  distribution. The effect is especially pronounced at low values of  $y_h$ , when hadrons are boosted into the forward direction.

The noise suppression (section 2.2.2) is applied to data and simulation. The resulting  $y_h$  distributions are compared in Figure 4.2. Good agreement of the suppressed noise measured with different H1 detector components is observed between data and simulation. For the remaining difference of the suppressed noise in Figure 4.2, a systematic uncertainty of 10% was assigned to the energy identified as noise in the LAr calorimeter.

The final hadronic energy measurement is performed using the energy flow algorithm HADROOII [89]. The inputs to the HADROOII algorithm are *clusters* and *tracks*. The clusters are formed from neighboring LAr calorimeter cells (see illustration in Figure 4.3) after the suppression of noise. Input tracks must satisfy certain quality criteria (see [89]) and must not point to isolated  $e$  or  $\mu$  candidates.

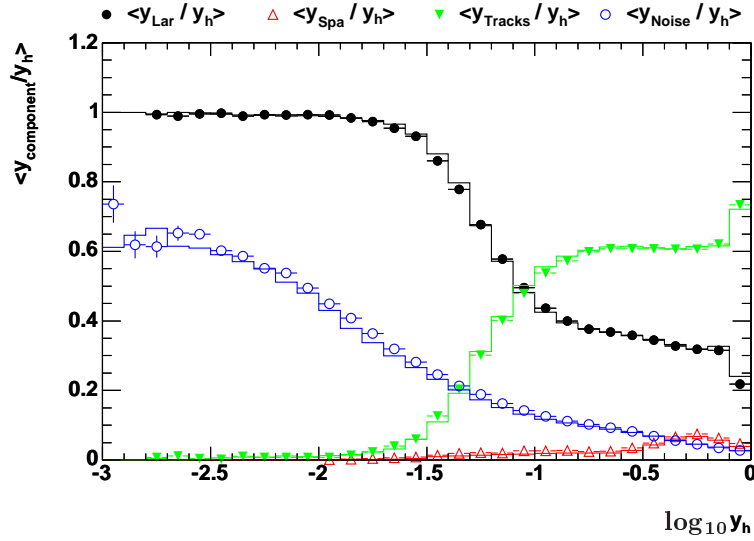


Figure 4.2: Contributions to  $y_h$  after noise suppression from the LAr, SpaCal and the tracking system are shown for data (points) and Monte Carlo (histograms). The variable  $y_{\text{Noise}}$  corresponds to the fraction of noise which has been removed. The sum of rest components is equal to 1.

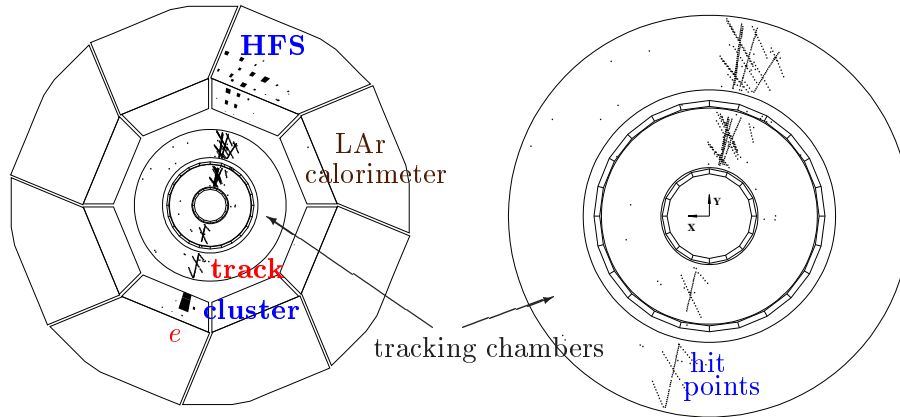


Figure 4.3: An illustration of the track and cluster formation in a NC event at the H1 detector. The right picture shows the radial view of the tracking chambers, raw "hits", i.e. recorded signals on sense chamber wires, and the reconstructed charged particle tracks. On the left side also the LAr calorimeter and the corresponding energy deposits in the individual cells are shown. Clusters are formed from the group of adjacent calorimeter cells containing deposited energy.

As a first step in the calibration procedure, a hadron finding algorithm associates clusters with tracks (so-called track-cluster "matching"): Each track is extrapolated up to the surface of the calorimeter as a helix, and as a straight line inside the calorimeter. The calorimetric energy  $E_{cylinder}$  is computed in the volume of a  $67.5^\circ$  cone originating at the calorimeter inner surface and the extrapolated track line intersection.

To achieve an optimal measurement for each particle in the hadronic final state, HADROOII compares the resolution of the tracker and the calorimeter. For this purpose the resolution of each track is compared with the expected calorimeter resolution on the basis of the particle's energy.

Low  $p_T$  charged particles in most cases have a better track measurement as the momentum resolution increases with decrease of the transverse momentum ( $\sigma_{p_T}/p_T \sim p_T$ ), while the relative energy resolution of the calorimeter improves with increasing energy  $E$  of the incident particle ( $\sigma_E/E \sim 1/\sqrt{E}$ ). If the resolution of the tracker is better than the resolution of the calorimeter and the observed calorimeter fluctuations are below 95 % C.L., the calorimetric energy  $E_{cylinder}$  is fully suppressed to avoid double counting. In case larger fluctuations are observed, they are considered as originating from neutral components in the showers (or other tracks) and are not suppressed. Similarly, if the resolution of the calorimetric energy is better than the resolution of the tracker and the energies  $E_{cylinder}$  and  $E_{track}$  are comparable, the calorimeter information is used to create a particle candidate.

The calibration of the hadronic energy is applied for the each jet<sup>1</sup> in the hadronic final state. The method to calibrate jets is described in [116]. This method uses DIS neutral current events and as a reference relies on the double angle kinematic reconstruction method which, as explained in chapter 3, is independent on the measured energies in the calorimeter.

The ratio of the hadronic transverse momentum and the double angle transverse momentum is used in the calibration and is called  $p_T^{bal}$

$$p_T^{bal} = \frac{p_{T,h}}{p_{T,da}} \quad (4.1)$$

$p_{T,h}$  is defined in equation 3.3. An example of the  $p_T^{bal}$  distribution for NC data and MC events (before calibration) is shown in Figure 4.4 (left).

Constants to correct the hadronic energy to the true level are determined using NC events selected with one jet only and such that the  $p_{T,da}$  measurement is well under control (for the full selection list refer to [89]).

The calibration constants are determined from a certain factor  $F_{ptbal}$ . This

---

<sup>1</sup>A jet is a collimated bunch of the hadronic final state particles.

factor is obtained from a fit to the mean values of the  $p_T^{bal}$  distributions as function of  $p_{T,da}$ , separately in different  $\theta$  regions. Only jets with  $p_T^{jet} > 4 \text{ GeV}$  are calibrated with this method. The calibration of Monte Carlo events is performed separately following the same procedure.

The distribution of  $p_T^{bal}$  for one jet NC data and MC events after application of the calibration is given in Figure 4.4 (right).

More details of the calibration procedure can be found in [89].

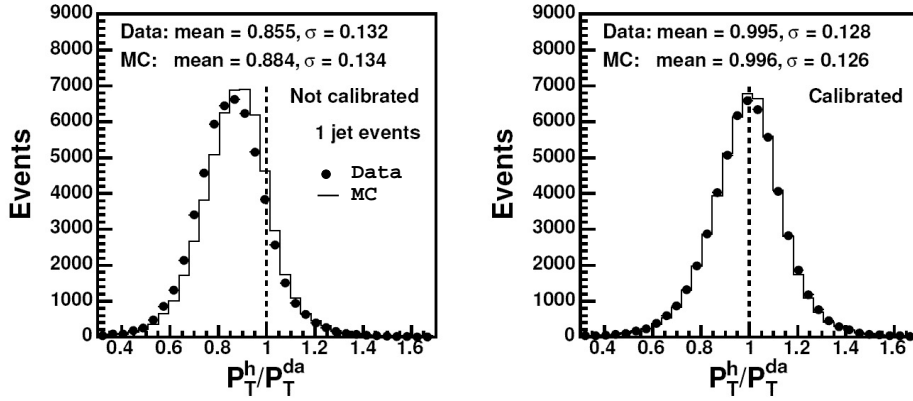


Figure 4.4:  $p_T^{bal} = p_{T,h}/p_{T,da}$  distribution for one jet data (points) and MC (line) events before (left) and after (right) the calibration. From [89].

To test the calibration procedure a large sample with different sets of selection cuts (see [89]) of DIS neutral current events is used. Moreover, this neutral current event sample is subdivided into one, two and three jet event sub-samples in order to be independent from the events used in the calibration.

The agreement between neutral current data selected two jets and the corresponding Monte Carlo sample after the calibration is shown in Figure 4.5.

The comparison of the balance in transverse momentum separately for the data and the Monte Carlo simulation versus the electron transverse momentum  $p_{T,e}$  and the hadronic angle  $\gamma_h$  is given in Figure 4.6. The agreement of data and Monte Carlo in both distributions is well within 2%, taken as the calibration uncertainty.

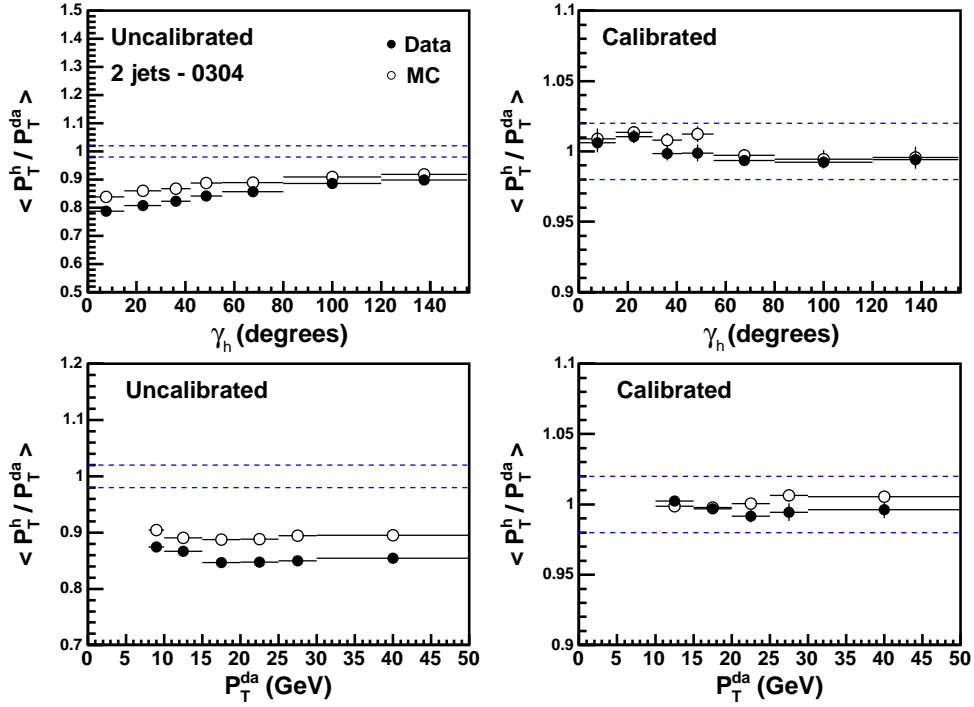


Figure 4.5: Distributions of  $p_T^{bal}$  for data and Monte Carlo events as function of the hadronic polar angle  $\gamma_h$  (upper two plots) and  $p_{T,da}$  (bottom two plots) before (left) and after (right) jet calibration. The dotted lines represent a  $\pm 2\%$  uncertainty around unity.

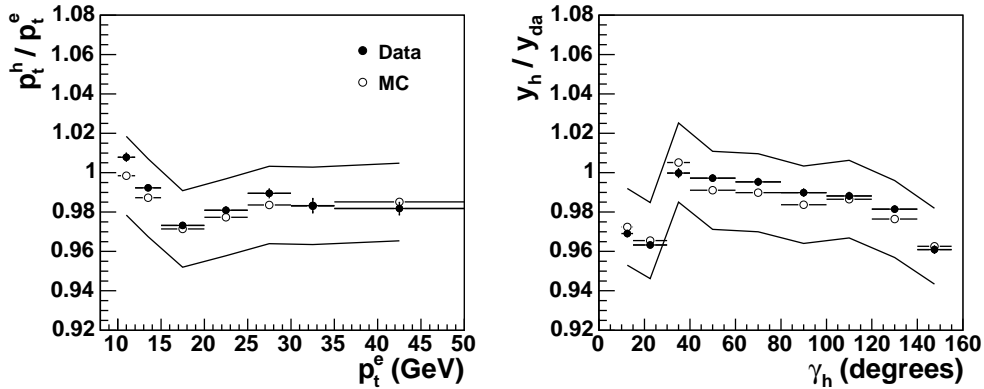


Figure 4.6: Distributions of the  $p_T$  balance after calibration for data and Monte Carlo simulation as function of the electron transverse momentum  $p_{T,e}$  (left), and the  $y$  balance ( $y_h/y_{da}$ ) as function of the hadronic angle  $\gamma_h$  (right). The lines show a  $\pm 2\%$  variation of the simulation.

## 4.2 Interaction Vertex Reweighting for Simulated Events

For the correct CC event kinematic reconstruction it is important that simulated CC events describe the data in all aspects, including the  $z$  position of the  $ep$  interaction vertex. The  $z$  position is important, since all kinematic variables depend on angular information, using the vertex as the origin.

Different beam conditions, defined by the beam optics, cause variations of the  $ep$  interaction vertex position (for detailed explanation see chapter 5). The variation of the vertex position in the longitudinal ( $z$ ) direction is influenced also by the length of the particle bunches. These variations result in a Gaussian distribution of the interaction  $z$  position around the average nominal interaction point.

For practical reasons all Monte Carlo events are simulated with the mean position of  $\langle z \rangle = 0$  cm and a fixed Gaussian width for the  $z$  distribution of the vertex,  $\sigma_z = 13$  cm. The simulated  $z$  distribution therefore must be adjusted to the data. The NC events are used to determine the  $z$  vertex shape, resulting in reweighting factors which are applied to the MC. An 11th order polynomial is used to parametrise the reweighting function with parameters  $\beta_i$ . The weight applied to MC is calculated as:

$$w_{zvtx} = \frac{\sum_{i=0}^{10} \beta_i z_{vtx}^i}{\beta_{11}} \quad (4.2)$$

The  $z$  vertex distributions of the NC data and NC Monte Carlo events before and after the MC reweighting are shown in Figure 4.7. Details about the vertex reweighting procedure can be found in [115].

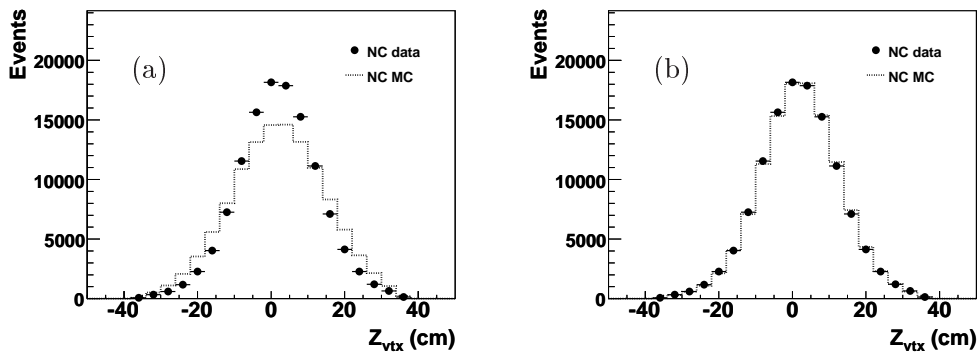


Figure 4.7: Distributions of the  $z$  vertex for NC data and NC Monte Carlo events (a) before reweighting, (b) after the simulation is adjusted to the  $z$  vertex distribution of the data.

### 4.3 Pseudo Charged Current Events (PSCC)

For the present measurement it is essential to know the efficiencies of the triggers used to trigger charged current events. In principle, a monitoring sample of the data using independent triggers could provide a possibility to determine the trigger efficiencies. Due to low statistics and absence of independent monitoring subtriggers it is not possible to use this method for CC events. The trigger simulation in the CC Monte Carlo events also cannot be used as it is not fully reliable in this respect. Moreover, CC simulated events have to be corrected for the efficiencies of the CC selection requirements.

In order to fulfill all these needs, NC data events are employed: If the information of the scattered electron in the detector is removed, the resulting event topology becomes almost identical to the one of the charged current (as explained in section 1.2.3, some difference expected concerning radiative effects) [117]. Such events are called *pseudo charged current* (PSCC) events.

In the PSCC procedure<sup>2</sup> the scattered electron finding algorithm is applied to each selected NC event. When the electron is found, all relevant detector information, i.e. tracks and calorimetric energy, found inside the  $\eta - \phi$  cone ( $\phi$  is the azimuth angle and  $\eta$  is pseudorapidity<sup>3</sup>) with the radius  $R_{\eta-\phi} = 29^\circ$  is removed from the event. The cone radius is defined as:

$$R_{\eta-\phi} = \sqrt{\Delta\eta_{tracks}^2 + \Delta\phi_{tracks}^2}.$$

In order to obtain correct kinematics, the full event reconstruction (H1REC, see section 2.3.4) is applied to the modified NC (i.e. PSCC) events.

Finally, PSCC events are reweighted to the charged current cross section so that the correct kinematic distributions expected for real CC events are reproduced: Each PSCC event receives a weight  $w(x, Q^2)$  with which it enters into all subsequent distributions. The weight is defined as:

$$w(x, Q^2) = \frac{d^2\sigma_{CC}}{dx dQ^2} / \frac{d^2\sigma_{NC}}{dx dQ^2} \quad (4.3)$$

Here,  $x$  and  $Q^2$  are taken as measured for the neutral current event. Both, charged and neutral current cross sections are calculated using the H1 PDF 2000 [18] parton distribution functions.

---

<sup>2</sup>The code modifying the NC events to PSCC events was developed by many authors. Several improvements were made to the code in order to fulfill certain requirements for the present analysis. These modifications are described in the next chapter.

<sup>3</sup>The pseudorapidity  $\eta$  is defined as  $\eta = -\ln(\tan(\theta/2))$ .



An example of a neutral current event and the corresponding PSCC event is displayed in Figure 4.8.

The method to determine the CC selection efficiencies using PSCC events is discussed in chapter 5.2.

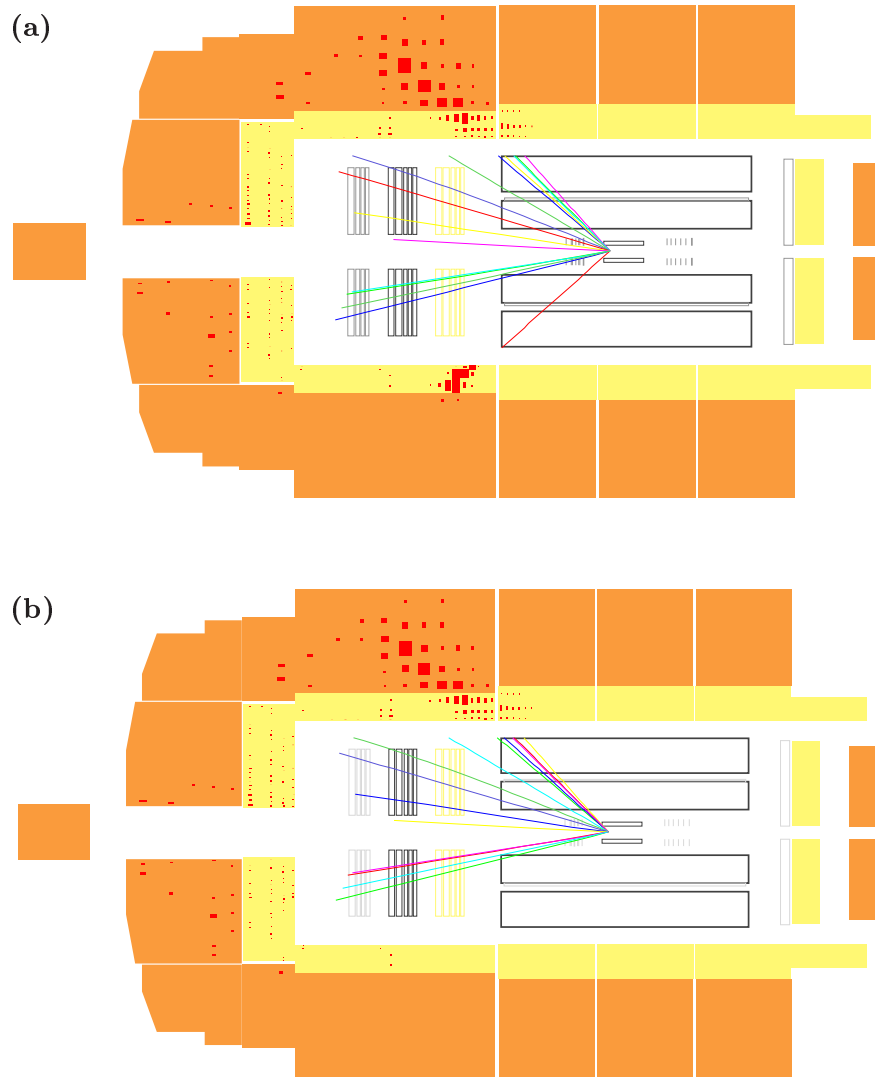


Figure 4.8: Neutral current event (a) and the same event after the electron removal - PSCC event (b).



## Chapter 5

# Charged Current Data

The  $e^+p$  data collected in the years 2003-04 with the H1 detector are considered in this analysis. The data correspond to  $47.6 \text{ pb}^{-1}$  of total integrated luminosity and comprise two periods with different helicity states of the beam positron. The integrated luminosity  $\mathcal{L}$  and the luminosity weighted mean polarisation  $P_e$  for these data are given in Table 5.1. In the table and throughout this thesis the notations "L" and "R" are used for periods with the left ( $P_e < 0$ ) and right ( $P_e > 0$ ) handed positrons, respectively.

data sample	luminosity $\mathcal{L} \text{ (pb}^{-1}\text{)}$	polarisation $\langle P_e \rangle \text{ (\%)}$	time period
L $e^+$	20.7	-40.2	3.4.2004 - 19.6.2004
R $e^+$	18.4	33.3	17.10.2003 - 1.4.2004
	8.5	34.3	2.7.2004 - 12.8.2004
sum of R	26.9	33.6	

Table 5.1: *Main characteristics of the data samples used in the analysis.*

This chapter is entirely devoted to the selection of CC events in the presented data sets which are needed to measure CC cross sections.

The general quality criteria valid for most of the analyses and the data pre-selection procedure are described first. As explained in section 2.3, the raw data rate is already significantly reduced by the H1 Trigger System with the help of the trigger elements designed for specific physics event signatures. The description of the final CC selection requirement starts with the *subtriggers*, i.e. compositions of the trigger elements optimised to trigger charged current interactions.

In the following, the kinematic phase space of the measurement is defined. This is done by the interaction vertex requirement (in order to select events in the optimised detector resolution region) and the kinematic cuts.

A set of selection requirements have been designed to suppress background

events. To reject  $ep$  events which are backgrounds to CC reactions (see section 1.3) various software algorithms have been developed or adopted from previous analyses. Finally, the non- $ep$  background event classes and their specific rejection methods are discussed.

To control the CC selection requirements and to study detector effects in the data (used to correct the response in simulated events), the *pseudo charged current* technique is used (see chapter 4). The determination of selection efficiencies is described in the second part of this chapter. On the basis of these efficiency studies the systematic uncertainties for each selection requirement were determined and are discussed at the end of each section.

The characteristics of the final selected charged current event samples are given at the end of this chapter.

## 5.1 Charged Current Selection

### 5.1.1 Run Selection

The data collected by the H1 and the other HERA experiments is delivered during so-called *luminosity fills*. A fill starts with the time when both particle beams are brought into colliding mode after optimising the beam optics for maximum luminosity and minimum background. The fill usually ends with the dump of one or both beams, mainly determined by the lifetime of the positron beam (typically  $\sim 10$  h). The data are collected by the experiments in *runs*, which are defined by stable detector conditions. Typically, during one fill there are many runs taken. The quality of a run is defined corresponding to the operational status of the detector components and is distinguished as *good*, *medium* or *poor*. During a good run all "major" systems (tracking devices, LAr, luminosity system, SpaCal and central muon chambers) are operational. A run is declared as medium if at least one of the major systems is not working or several subsystems are out of operation. The run is poor if there is a serious hardware or software problem.

- For the present data analysis only **good** and **medium** runs were accepted,
- a **minimum luminosity** of  $0.2 \text{ nb}^{-1}$  per run (corresponding to a run of  $\sim 10$  s duration) was required in order to ensure that the detector operation was stable during data taking.

The *High Voltage* (HV) requirement is an important data selection criterium which shows the operation status of the device. For example, the HV of

the tracking system during a run may "trip" due to short beam instabilities resulting from a large particle flow in the detector. During such trips the HV is temporarily switched off to protect the chambers. In contrast to the tracking system, high voltage is always applied for the LAr calorimeter. The HV status is differentiated on a single event basis.

- **HV requirement** for analysed events is applied for LAr, CJC, CIP, TOF and luminosity system.

As mentioned in section 2.2.4, some subtriggers which trigger high rate physics reactions (like photoproduction, see section 1.3.1) can have a prescale greater than 1, i.e. not each triggered event will actually be kept.

- The data were selected with the prescale of 1, i.e. with subtriggers **without prescale**. Dedicated studies were performed to validate no prescale for the CC subtriggers.

In addition, in order to rely on the  $e^+$  polarisation measurement,

- only those events were accepted where at least one of the two **polarimeters** (LPOL preferred) has been operational.

The "profile" of the  $e^+$  polarisation (i.e. luminosity versus  $e^+$  polarisation) measured for the analysed data sample is shown in Figure 5.1. The small region with  $-20\% < P_e < 0\%$  was excluded from the analysis in order to measure the charged current cross sections with a high mean polarisation.

In addition to the standard run selection given above, four run ranges with CIP readout and data logging problems have been removed from the analysis: 360177-360281, 361882-362486, 372336-372619 and 384836-385073. All excluded runs together correspond to  $\sim 0.6 \text{ pb}^{-1}$  of integrated luminosity.

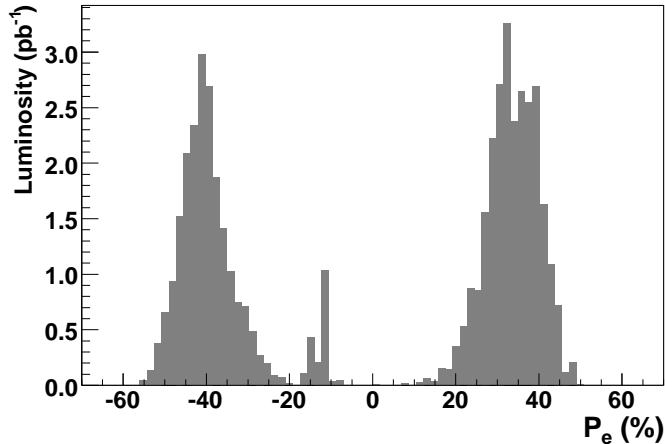


Figure 5.1: *Polarisation profile for the 2003-04  $e^+p$  data taken by the H1. The low negative polarisation region ( $-20\% < P_e < 0\%$ ) is excluded from the present analysis.*

### 5.1.2 Loose Pre-Selection

The run quality, minimum run luminosity and several additional requirements which are given below, were used for the **preselection** of the inclusive neutral and charged current DIS data sample. The cuts which were relevant for the charged current preselection are:

$$p_{T,miss} > 8 \text{ GeV},$$

$$Q_h^2 > 100 \text{ GeV}^2,$$

$$y_h < 0.95,$$

**rejection of "obvious" non- $ep$  background.**

The  $p_{T,miss}$  and  $Q_h$  cuts are based on the typical charged current event signature, i.e. missing transverse momentum (result of the undetected  $\nu$ ). The high  $y_h$  region was excluded due to poor resolution of the hadronic reconstruction method (see chapter 3). Finally, a significant part of the non- $ep$  background was rejected by a set of high efficiency topological background finders which will be discussed further in this chapter. The studies performed have shown that no interesting physics events were lost in the preselection step due to calibration or other data treatments. The effect of the preselection cuts on the simulated CC and simulated background events is shown in Figure 5.2. With the given preselection a factor of 40 was achieved in the reduction, resulting to the data sample of  $\approx 2$  million events. With this sample the optimisation of the final cuts and cut control was performed, as described below.

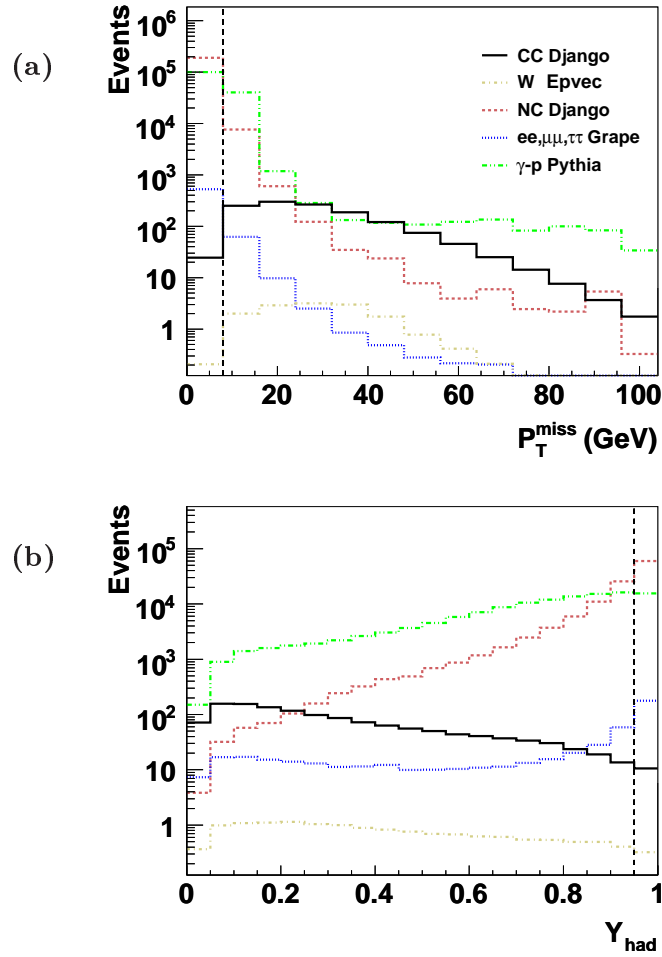


Figure 5.2: The  $p_{T,\text{miss}}$  (a) and  $y_h$  (b) distributions for the simulated charged current events and simulated background processes (see section 1.4) for  $Q_h > 100 \text{ GeV}^2$ . The preselection cuts ( $p_{T,\text{miss}} > 8 \text{ GeV}$  and  $y_h < 0.95$ ) are indicated in the plots.

### 5.1.3 Final Selection

#### Trigger requirements: S66||S67||S77

The triggering of charged current events is based on the "missing" transverse momentum caused by the undetected neutrino (LAr\_Etmiss trigger element) and the event timing information (LAr\_T0 and CIP\_T0). In addition, global veto conditions (see section 2.2.4) are applied to the subtriggers. The complete definitions of the charged current subtriggers as used in the present analysis are given in Table 5.2.

<i>ST</i>	<i>trigger elements</i>	<i>description</i>
S66	(LAr_IF>1&& LAr_Etmiss>2) && (CIP_T0    (LAr_T0 && !CIP_T0_nextBC)) && (FIT_IA    !FIT_BG) && (!SPCLh_AToF_E_1 && !VETO_BG && !BToF_BG && !SToF_BG) && (!(CIP_MUL>7 && CIP_SIG==0))	phys. signature timing criteria veto condition
S67	(LAr_electron_1) && (CIP_T0    (LAr_T0 && !CIP_T0_nextBC)) && (FIT_IA    !FIT_BG) && (VETO_BG && !BToF_BG && !SToF_BG) && (!(CIP_MUL>7 && CIP_SIG==0))	phys. signature timing criteria veto condition
S77	(CIP_SIG>0 && LAr_Etmiss>1) && (CIP_T0) && (FIT_IA    !FIT_BG) && (!BToF_BG && !SToF_BG) && (!(CIP_MUL>7 && CIP_SIG==0))	phys. signature timing criteria veto condition

Table 5.2: *List of the charged current subtriggers and their logical trigger element combinations.*

**Subtrigger 66** is designed to trigger events passing a high  $E_{T,miss}$  threshold<sup>1</sup> in coincidence with deposited energy in the forward LAr region (LAr\_IF>1).

About 66% of the charged current events are triggered by this subtrigger.

**Subtrigger 67** is designed to trigger NC events. The main element of S67 is LAr\_electron\_1. The electromagnetic FADC (see section 2.3.1) energies of a given big tower (BT) are discriminated by  $\theta$  - dependent thresholds ( $\sim 5$  GeV). The trigger bit is set for a BT if the electromagnetic part of the tower passes this threshold. This subtrigger is also very efficient for the triggering of charged current events: About 84% of charged current events triggered by S67.

**Subtrigger 77** is the main charged current subtrigger. It triggers all low transverse momentum events: LAr\_Etmiss>1 corresponds to the low  $E_{T,miss}$  threshold. CIP\_SIG>0 is the loosest central vertex requirement. Generally, there are four CIP\_SIG trigger elements which are set according to following condition:

<sup>1</sup>In total there are three  $E_{T,miss}$  thresholds in the LAr calorimeter. The thresholds have been set to 38 FADC counts ( $\sim 4.75$  GeV), 48 FADC counts ( $\sim 6$  GeV) and 60 FADC counts ( $\sim 7.5$  GeV) [118], respectively.



$$N_{ctr}^{tracks} > K(N_{fwd}^{tracks} + N_{bwd}^{tracks})$$

where  $N_{ctr}^{tracks}$ ,  $N_{fwd}^{tracks}$  and  $N_{bwd}^{tracks}$  are the number of CIP tracks in the central, forward and backward regions, respectively.  $K$  is a multiplication factor which is equal 0 (or 1, 2, and 4) for the significance 0 (or 1, 2 and 3).

Typically about 98% of the charged current events are triggered by S77.

For the description of the veto trigger elements given in Table 5.2, see sections 2.2.4 and 2.3.1.

### Interaction Vertex Requirement

The beam optics can slightly differ from one luminosity fill to another and thus cause variations of the  $ep$  interaction vertex position. Variation of the beam position in the  $x, y$  plane (*beam shift*) and possible beam inclinations with the respect to the H1 coordinate system (*beam tilt*) are relatively small (typically of order few  $mm$ ) and are determined for the data on a run by run basis. Due to the beam bunch structure (each  $e$  bunch has a width of  $\sigma_z \sim 1\text{ cm}$  in the longitudinal direction, the  $p$  bunch has a width of  $\sigma_z \sim 13\text{ cm}$ ) the interaction position in the  $z$  direction has a nearly Gaussian distribution around the average nominal interaction point ( $z = 0\text{ cm}$ ). As the detector provides better resolution and therefore better kinematic reconstruction for the  $ep$  interactions close to nominal interaction point, the  $z$  vertex reconstruction is restricted in the present analysis to

$$-35\text{ cm} < z_{vertex} < 35\text{ cm}.$$

This range corresponds to  $\sim 3\sigma$  of the  $z$  vertex distribution. The requirement is applied to the vertex determined from tracks measured in the central drift chamber (*central vertex*).

As described in section 4.2, the Monte Carlo events are reweighted to the  $z$  vertex distribution of the NC data.

The distributions of the interaction vertex in the  $z$  direction for the 2003 - 04 CC data and the reweighted CC Monte Carlo events are presented in Figure 5.3. Good agreement is seen in the figure between the data and MC distributions for both data sets (the larger fluctuations observed in the L data are caused by limited statistics).

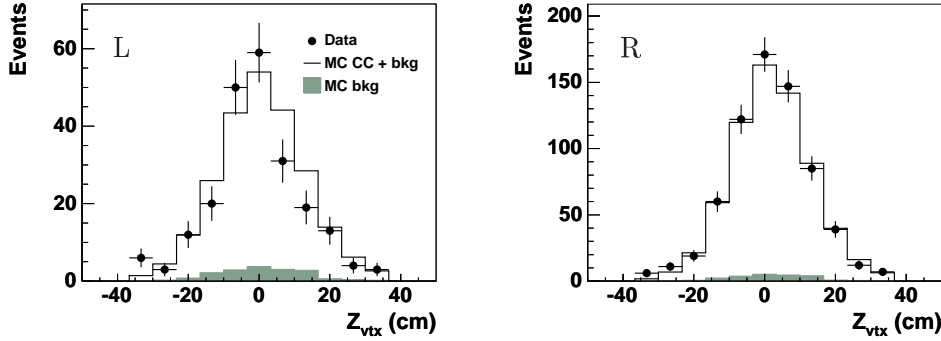


Figure 5.3: *Distribution of the  $z$  vertex for the 2003-04 CC events of the L (left) and R (right) periods. The CC MC and simulated background contributions are also shown.*

### Definition of the Kinematic Phase Space

The kinematic phase space for the charged current cross section measurements was chosen with respect to the detector acceptance and selection efficiencies as follows:

$$p_{T,miss} > 12 \text{ GeV}$$

determined by the rapid decrease of the trigger efficiency towards low  $p_{T,miss}$  (below 40% for  $p_{T,miss}$  smaller than 12  $GeV$ , see section 5.2.1), and the increase of the  $ep$  induced background as will be explained further in this chapter.

$$0.03 < y_h < 0.85$$

the upper, i.e. high  $y_h$  limit is determined by the poor  $Q^2$  resolution of the hadron method (see chapter 3). The low  $y_h$  region is limited due to the detector acceptance where the hadronic final state is partially lost in the beam pipe and thus degrading the trigger efficiency in this region (see section 5.2.1).

$$Q_h^2 > 223 \text{ GeV}^2$$

this requirement is correlated with the  $p_{T,miss}$  cut. The chosen value of 223  $GeV^2$  is defined by the binning used for this measurement as described in chapter 6. The binning was chosen to be consistent with previous analyses on unpolarised data.

## Background Rejection

Backgrounds to charged current interactions originate from two sources:

- $ep$  induced background
- non- $ep$  induced background

In the following these background classes are explained and the specific background rejection methods are discussed in detail.

### $ep$ Induced Background

The largest contributions of the background processes to the charged current sample are induced by  $\gamma p$  and neutral current events (the processes have been introduced in chapter 1).

### Rejection of the photoproduction background

The variable used to distinguish between  $ep$  background processes and the genuine charged current events is based on the transverse momentum imbalance [119]: While the neutrino is always scattered in the opposite direction to the struck quark (apparent transverse imbalance of the final state particles in the detector), the  $\gamma p$  is expected to have final state particles isotropically distributed around the beam axis, i.e. not showing any missing  $p_T$ . However, photoproduction events can "obtain" some transverse imbalance caused by leptonic decays of HFS particles and by imperfect hadronic measurement.

The sums of the transverse momentum vectors parallel ( $\vec{p}_{T,p}$ ) and anti-parallel ( $\vec{p}_{T,ap}$ ) to the transverse vector sum formed by the all detected particles ( $\vec{p}_{T,h}$ ) are defined as:

$$V_{ap} = - \sum_{ap} \frac{\vec{p}_{T,h} \cdot \vec{p}_{T,ap}}{p_{T,h}}, \quad (5.1)$$

$$V_p = \sum_p \frac{\vec{p}_{T,h} \cdot \vec{p}_{T,p}}{p_{T,h}}, \quad (5.2)$$

The axis defining the positive hemisphere in the transverse plane is given by the transverse vector sum  $\vec{p}_{T,h}$  and thus the parallel and anti-parallel momentum vectors are  $\vec{p}_{T,h} \cdot \vec{p}_{T,p} > 0$  and  $\vec{p}_{T,h} \cdot \vec{p}_{T,ap} < 0$ .

The ratio of  $V_{ap}$  and  $V_p$  is called  $V_{ratio}$ :

$$V_{ratio} = \frac{V_{ap}}{V_p}. \quad (5.3)$$

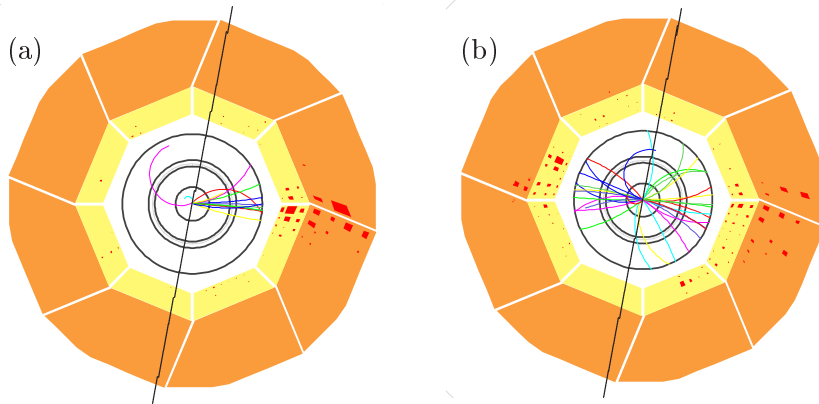


Figure 5.4: *Radial view of a typical charged current (a) and a typical photoproduction event (b). The lines shown are perpendicular to the axis of the transverse vector sum of the all detected particles ( $\vec{p}_{T,h}$ ) and divide the detector in two hemispheres visualising the large transverse imbalance in the charged current event (all measured final state momentum is in one hemisphere, since the  $\nu$  is not detected on the opposite side). In the photoproduction event the measured transverse momentum is approximately equal in both hemispheres.*

Charged current events with a large transverse imbalance would typically have very different  $V_{ap}$  and  $V_p$  components leading to  $V_{ratio} \approx 0$ . In photoproduction events with balanced transverse momentum vectors,  $V_{ratio} \approx 1$ .

In the present analysis the variable  $V_{ratio}$  is calculated summing over all particles measured in the detector after the noise subtraction and calibration (section 4.1). A cut of  $V_{ratio} \leq 0.25$  is applied in this analysis (Figure 5.5 (a)).

Further studies with the  $\gamma p$  and charged current Monte Carlo events showed that the rejection power of the  $V_{ratio}$  cut is strongly improved in combination with the  $p_{T,miss}$  variable [120]. As seen from the 2-dimensional  $V_{ratio} - p_{T,miss}$  plot in Figure 5.5 (b), a significant part of the  $\gamma p$  background has low  $p_{T,miss}$  and high  $V_{ratio}$  values. With the increase of  $p_{T,miss}$  the charged current events start to dominate. The dashed line in this figure indicates the 2-dimensional  $V_{ratio} - p_{T,miss}$  cut optimised for the present analysis.

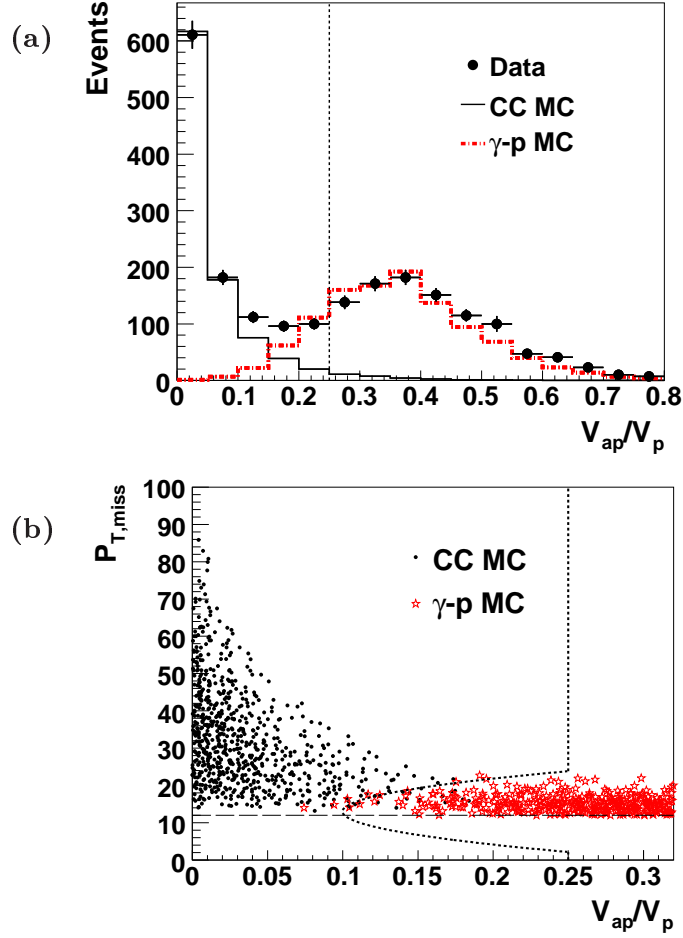


Figure 5.5: Illustration of  $\gamma p$  background suppression cuts: (a)  $V_{ratio}$  distribution for the 2003-04 data, CC MC and  $\gamma p$  MC after all other selection cuts. The dashed lines indicate the cut  $V_{ratio} \leq 0.25$ . (b) 2-dimensional  $V_{ratio}$  and  $p_{T,miss}$  distribution for CC MC and  $\gamma p$  MC events. The dashed line indicates the 2-dimensional  $V_{ratio} - p_{T,miss}$  cut down to  $p_{T,miss} = 12$  GeV (horizontal line) used as an additional CC selection requirement.

### Neutral current event rejection

The majority of NC events are already strongly suppressed by the kinematic phase space and selection requirements adjusted for the CC events. However, a small fraction of NC events ( $\sim 5\%$ ) satisfies the CC selection requirements and enters in the final CC sample. These are mainly NC events where the scattered electron is not identified as such in regions where the calorimetric measurement is poor.

There are three algorithms applied in the presents analysis to suppress these remaining NC events. In the first algorithm the reconstructed track of the misidentified electron is used to recognise NC events:

1. The event has an isolated track opposite to the hadronic final state.

An isolated track is defined as opposite to the hadronic final state if the difference between the track and the hadronic final state (HFS) in the azimuth angle  $\phi$  is

$$\Delta\phi = |\phi_{track} - \phi_{HFS}| \geq 160^\circ$$

The isolation criterium is applied only to tracks identified as non leptonic (originating neither from electrons or muons) and have reliable momentum measurement, i.e. with  $p_T > 1 \text{ GeV}$  and  $\Theta > 25^\circ$ . The track is isolated if there is no another track in the  $\eta - \phi$  cone around it with a radius  $R_{\eta-\phi} = 0.5$  ( $29^\circ$ ), calculated as

$$R_{\eta-\phi} = \sqrt{\Delta\eta_{tracks}^2 + \Delta\phi_{tracks}^2}$$

Here,  $\Delta\phi_{tracks}$  and  $\Delta\eta_{tracks}$  are the difference in azimuth angle  $\phi$  and pseudorapidity  $\eta$  between two tracks.

The second algorithm searches for isolated electrons opposite to the hadronic final state:

2. The event has an isolated electron with large  $D_{jet}$  and acomplanarity  $\Delta\phi_{ac} \geq 160^\circ$ .

The quantity  $D_{jet}$  defines the distance in  $\eta - \phi$  space between the isolated electron and the four-vector of the closest jet (or hadronic final state if there is no jet):

$$D_{jet} = \sqrt{\Delta\eta_{e-jet}^2 + \Delta\phi_{e-jet}^2}$$

It is required that the  $D_{jet}$  is greater than 1.0 ( $57.3^\circ$ ).

The lepton acoplanarity  $\Delta\phi_{ac}$  is the distance in azimuth angle  $\phi$  between the electron and the four-vector of the hadronic final state

$$\Delta\phi_{ac} = |\phi_{lepton} - \phi_{HFS}|$$

The isolation here means electron against the hadrons, i.e. the identified electron is called isolated if the calorimeter energy in the cone around the electron of radius  $R_{\eta-\phi} = 0.5$  ( $29^\circ$ ) is less than 5% of the electron energy [121, 122].

Finally, an additional cut was developed in this analysis in order to reduce the remaining fraction of neutral current events with the scattered electron:

3. The event has an identified scattered electron and a balanced transverse momentum  $p_{T,bal} = p_{T,h}/p_{T,e}$ :

$$0.75 < p_{T,h}/p_{T,e} < 1.05$$

The distribution of  $p_{T,h}/p_{T,e}$  for the CC events, CC simulated and NC simulated events before and after this cut is shown in Figure 5.6.

The remaining number of the NC events in the CC sample after the described NC rejection algorithms is reduced to below the permil level.

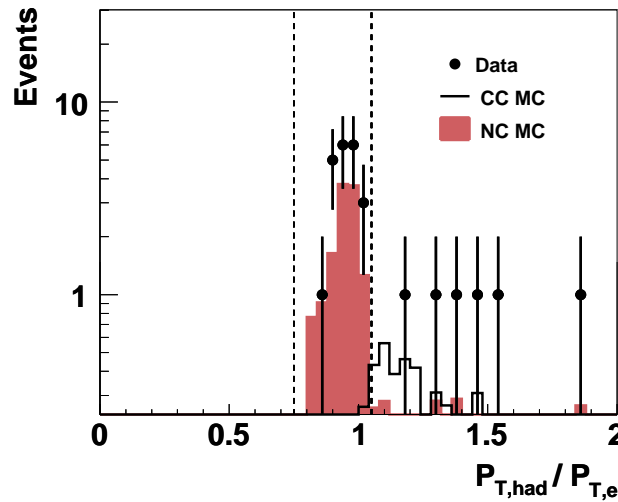


Figure 5.6: *Distribution of  $p_{T,h}/p_{T,e}$  for the CC data, CC and NC Monte Carlo events with the scattered electron. The full charged current selection as well as 1 and 2 NC rejection cuts are applied to these event samples. The dashed lines indicate the region rejected by the cut 3.*

### Non- $ep$ Induced Background

The non- $ep$  backgrounds are cosmic muons crossing the detector, beam particle interactions (mostly protons) with the residual gas nuclei inside the beam pipe (*beam gas*), and particle interactions with the beam pipe or accelerator components surrounding the beam pipe (*beam halo* events). All three such background types are largely suppressed during the data taking by the ToF system (see section 2.2.4) and dedicated L4 filters (see 2.3.4 section). However, the rate of non- $ep$  background still remains very high (relative to the small cross section of CC events) and requires additional rejection at the analysis level. This is done by filter algorithms called *topological non-ep background finders* [123–125].

The background suppression is based on the topological signatures of each class:

- **cosmic muons** originate from collisions of cosmic rays with the atmosphere and leave "downgoing" tracks in the instrumented iron, LAr calorimeter and the tracking devices;
- in the final state of the **beam gas** interactions many low  $p_T$  particles are produced which are distributed isotropically in the transverse plane. These particles correspondingly generate many low  $p_T$  tracks in the H1 tracking chambers. As a result of the high energy of the proton beam, the final state particles are boosted in the direction of the proton beam. Beam gas events may be misidentified as charged current events if the proton collides with beam gas nuclei close to the  $ep$  interaction vertex and due to hadronic final state fluctuations when the event "obtains" missing transverse momentum;
- the signature of **beam halo** events is a muon track crossing the detector parallel to the beam pipe. These muons are originating from interactions of the protons with the beam pipe or machine elements surrounding the beam pipe far upstream of the detector (the  $\mu$ 's mainly comes from pions and kaons). The hadronic components of these interactions are quickly absorbed by the surrounding material and usually are not arriving at the detector.

The non- $ep$  background events may also overlap with the physics events or with each other. Such events are called *overlap events*. Examples of each background class and one overlap event are presented in Figures 5.7-5.10.



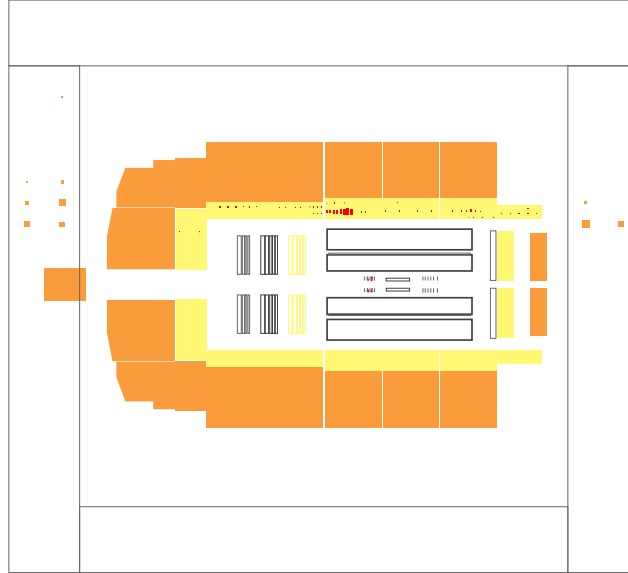


Figure 5.7: An example of a beam halo event. The  $\mu$ 's originating from beam proton interactions with the beam pipe or surrounding elements (usually far upstream the detector) leave characteristic energy pattern in the electromagnetic LAr calorimeter and the muon chambers parallel to the beam pipe.

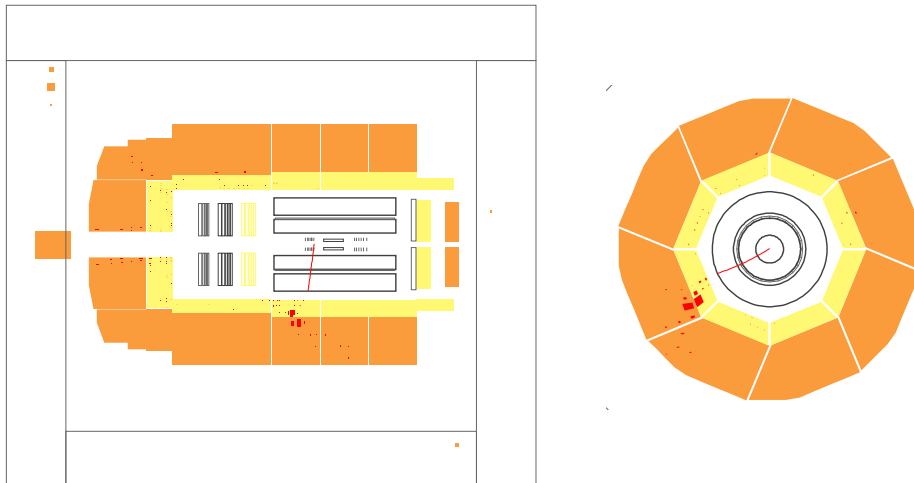


Figure 5.8: An example of a cosmic event. A high energy muon generates an energy deposit in LAr calorimeter and straight track in the tracking chambers, resulting in a missing transverse momentum  $p_{T,miss} = 24.6$  GeV. Due to the single reconstructed track pointing into the expected  $ep$  interaction vertex this event satisfies all CC selection requirements. The event was rejected during the visual scanning.

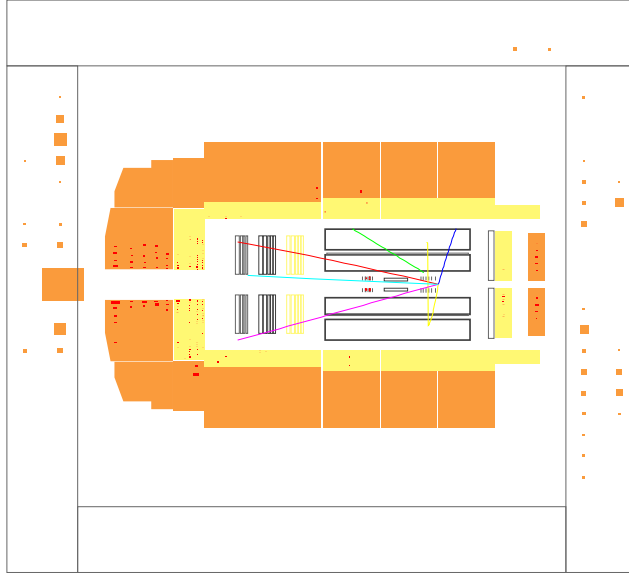


Figure 5.9: An event with several overlapping beam-gas interactions. The  $\mu$  energy patterns are clearly visible in the muon chambers. Such events may contribute to CC background if the proton interaction with the residual gas nuclei occurs close to the ep interaction region, and also if fluctuations in the final state induce missing transverse momentum  $p_{T,miss}$ .

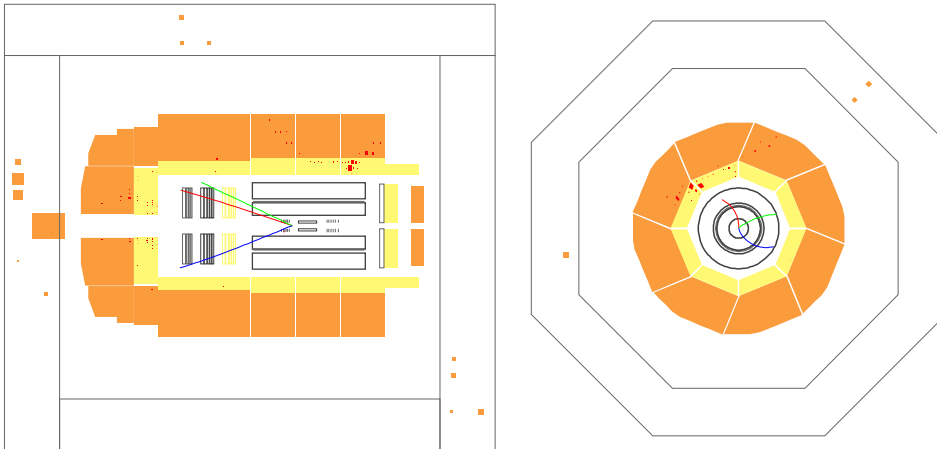


Figure 5.10: An example of an overlap event. A clear cosmic muon pattern crossing the detector is visible together with an ep interaction occurring at the same time. The total event missing transverse momentum  $p_{T,miss} = 17.4$  GeV. This event fulfilled all CC selection requirements but was rejected during the visual scanning.

### Topological background finders

A set of background finder algorithms, called QBGFMAR<sup>2</sup>, is used to reject the non-*ep* background introducing minimal inefficiency to the CC MC events. The algorithms in QBGFMAR have been developed to recognise typical signatures of cosmic, beam halo and beam gas events. At the analysis level QBGFMAR is implemented in a bit coded formats and stored as the flag *Ibg*. A short description of each QBGFMAR finder is given in Table 5.3.

Besides QBGFMAR, two additional sets of non-*ep* background finders, called *Ibgfm* and *Ibgam*, have been applied in the analysis. *Ibgfm* is an extension of the QBGFMAR package and uses different combinations of QBGFMAR variables (a detailed description can be found in [125]).

The *Ibgam* finders are described in Table 5.4 (taken from [125] and updated). The *Ibgam* bits 3, 4 and 8 are not applied in this analysis since these finders cause a inefficiency for charged current events (as was determined by CC MC events).

<i>bit</i>	<i>finder</i>	<i>description</i>
0	HALAR	longitudinal energy pattern in the LAr calorimeter
1	HAMULAR	longitudinal energy pattern in the LAr calorimeter with energy deposit inside the backward iron endcup
2	HAMUMU	horizontal muon track in the forward detector region and energy deposit inside the backward iron endcup
3	HASPALAR	cluster in the inner forward LAr part, matching energy deposit in SpaCal
4	HAMUIF	cluster in the inner forward LAr part, matching energy deposit inside the backward iron endcup
5	COSMUMU	two opposite muon tracks matching in directions
6	COSMULAR	at least one muon with 90% energy deposited in a matching LAr cluster
7	COSTALAR	two opposite clusters in the Tail Catcher with 85% energy deposited in matching LAr clusters
8	COSTRACK	two CJC tracks with opposite directions in space
9	COSLAR	LAr cluster with the highest hadronic energy deposit in the isolated cylinder of the radius 25 <i>cm</i> . Energy in the electromagnetic part is small.

Table 5.3: Overview of the QBGFMAR non-*ep* background finders as coded in 10 *Ibg* bits.

<sup>2</sup>A detailed description of QBGFMAR can be found in [124].

<i>bit</i>	<i>finder</i>	<i>description</i>
0	BEAMGASTRACK	many CJC tracks in the backward region of the detector
9		large ratio of the non-vertex/vertex fitted CJC tracks
1	COSLARSHAPE	cosmic muon not crossing drift chamber
2		cosmic muon crossing drift chamber with energy deposits in opposite sides of LAr calorimeter
3		cosmic muon crossing drift chamber with energy deposit in one side of LAr calorimeter with matching iron track
4	COSLARTRACK	high energy cluster without matching tracks
5	HALARTRACK	high energy horizontal cluster without matching tracks
6	HASPA	uniform energy deposition in SpaCal
7	COSTRACKTIME	cosmic muon determined by chronological sequence of CJC tracks
8		many non-vertex fitted CJC tracks with the large $T0_{CJC}$ time difference
10	BEAMGASLAR-TRACK	many CJC tracks in the backward detector region
11	HALARTRACK	no good quality track measured in the detector region with a good acceptance
12		large track-cluster mismatch in the polar angle $\theta$

Table 5.4: *Description of the non-ep background finders as coded in the Ibgam bits. Bits 3, 4 and 8 are not used in the present analysis.*

### Timing requirements

An additional background rejection is achieved requiring the event interaction time to be in coincidence with the bunch crossing (BC) time<sup>3</sup>. The event timing is determined precisely with the central drift chamber (from the drift time of the charged particles to the anode wires inside the chamber) or with the LAr calorimeter (an average  $T0$  timing derived from all big towers). The resolution of the  $T0$  of CJC chamber is  $\sim 2 ns$  (about 0.02 BC) and  $\sim 0.1 BC$  for the LAr  $T0$ .

The timing requirement applied in the analysis is a combination of both CJC and LAr  $T0$ :

$360 \text{ ticks} \leq T0_{CJC} \leq 510 \text{ ticks}^*$	(runs 357072 - 368000)
$410 \text{ ticks} \leq T0_{CJC} \leq 510 \text{ ticks}$	(runs 368001 - 392213)
$ T0_{LAr} - T_{LAr,nom}  \leq 0.54 \text{ BC}$	

\* 500  $T0_{CJC}$  ticks correspond to 96  $ns$

For the runs 357072 - 368000 the larger  $T0_{CJC}$  timing period was chosen in order to cover a secondary CJC  $T0$  peak which appeared in this period due to hardware problems. For the rest of time, i.e. runs 368001 - 392213, a tighter  $T0_{CJC}$  timing cut was applied. The timing distributions with the indicated cuts for the 2003-04 data after all charged current selection except the timing cuts are shown in Figure 5.11.

### Visual Event Scanning

After all cuts which were applied to the charged current candidates, an additional 33 events (3.5% of all 932 selected CC events) have been identified by visual scanning as non- $ep$  background. Two out of 33 events which were scanned away are shown in Figures 5.8 and 5.10.

---

<sup>3</sup>With the exception of COSTRACKTIME finder in *Ibgam*, the background finders do not have any timing requirements. The CJC timing ( $T0$ ) is used in COSTRACKTIME to determine the direction of a cosmic muon by chronological sequence of hits in the CJC.

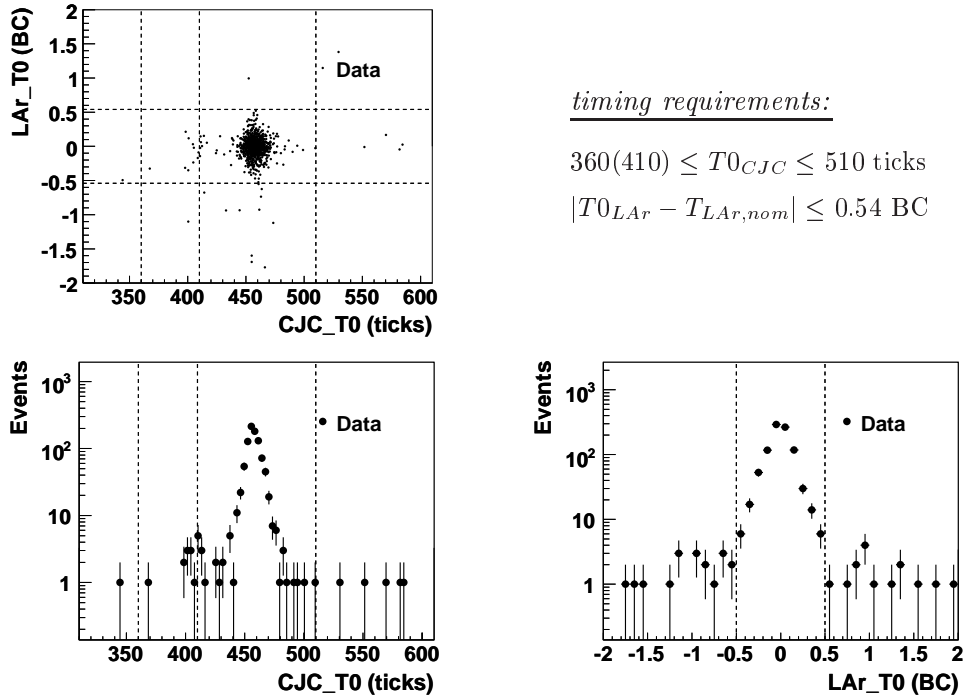


Figure 5.11: Distributions of the CJC and LAr timing signals ( $T0$ ) for selected CC events from the data taken in the years 2003-04. The timing requirements are indicated as dashed lines in the plots.

## A Summary of the Final CC Data Cuts

The summary of the charged current selection cuts is given below. In brackets the rejection of each step is given, starting from  $\approx 2$  million events after the loose pre-selection (section 5.1.2).

- **Trigger requirements:**  
 $S66 \parallel S67 \parallel S77$   
(reject  $\approx 29\%$ )
- **Primary interaction vertex:**  
measured by the central tracker in the region  
 $-35 \text{ cm} < z_{vertex} < 35 \text{ cm}$   
(reject  $\approx 65\%$  of the remaining sample)
- **Kinematic cuts:**  
 $p_{T,miss} > 12 \text{ GeV}$ ,  $0.03 < y_h < 0.85$  and  $Q^2 > 223 \text{ GeV}^2$   
(reject  $\approx 96\%$  of the remaining sample)
- **$ep$  induced background rejection:**  
 $\rightarrow V_{ratio} \leq 0.25$  and  $V_{ratio} - p_{T,miss}$  2-dimensional cut  
 $\rightarrow$  rejection of NC events  
(reject  $\approx 47\%$  of the remaining sample)
- **Non- $ep$  induced background rejection:**  
 $\rightarrow$  topological background finders (Ibg, Ibgfm and Ibgam)  
 $\rightarrow$  event interaction timing requirements:  
 $360(410) \leq T0_{CJC} \leq 510$  ticks and  $|T0_{LAr} - T_{LAr,nom}| \leq 0.54 \text{ BC}$   
(reject  $\approx 86\%$  of the remaining sample)
- visual event scanning  
(reject  $3.5\%$  of the final sample)

The total number of the CC events selected in the years 2003-04 is 899.

## 5.2 Efficiency Estimation Using PSCC Events

When the detector information of the scattered electron is "removed" in a NC event, the resulting event looks as a real CC event. Such events are called *pseudo charged current events* (PSCC), see section 4.3.

The PSCC events are used for the determination of the trigger requirement and selection efficiencies for the CC events. The simulated CC events are adjusted to the determined PSCC efficiencies so that Monte Carlo events model data in each analysis aspect (details see below).

The efficiency  $\varepsilon$  of any CC selection requirement using PSCC events is defined in a following way:

$$\varepsilon_{cut} = \frac{N_{PSCC}^{cut}}{N_{PSCC}^{all}} \quad (5.4)$$

Here,  $N_{PSCC}^{cut}$  is a number of weighted PSCC events (see section 4.3) which fulfill the cut requirements. It is a sum of the event weights:  $N_{PSCC}^{cut} = \sum w_{PSCC}^{cut}$ .  $N_{PSCC}^{all}$  is the total number of weighted PSCC events ( $N_{PSCC}^{all} = \sum w_{PSCC}^{all}$ ).

As will be shown later, the measurement of the cross section can be represented in double differential form, i.e. as function of the two independent kinematic quantities  $x$  and  $Q^2$ . All selection cut efficiencies in this thesis were determined in  $(x, Q^2)$  bins which are used for the double differential CC cross sections measurement. The simulation then is adjusted to the determined efficiencies in the each  $(x, Q^2)$  bin.



### 5.2.1 Trigger Efficiency

As discussed above, trigger efficiencies were determined using PSCC events. Since the data from the negative and positive polarisation periods (i.e. left and right handed data samples) could potentially have different detector performance, the efficiencies were determined separately for the L and R data sets. Further studies have shown that there are no significant differences between the efficiencies determined separately for two periods and are comparable within statistical errors. Nevertheless, the trigger efficiencies for two periods were used separately.

An example of the trigger efficiencies as function of  $x$  and  $Q^2$  for the right handed data period (with more integrated luminosity, see Table 5.1) are displayed in Figure 5.12.

The efficiencies as function of the missing transverse momentum  $p_{T,miss}$  and the hadronic angle  $\gamma_h$  are shown in Figure 5.13. Part of the inefficiency at low  $p_{T,miss}$  (corresponding to low  $Q^2$  and high  $x$ ) is caused by the limited detector acceptance at low  $\gamma_h$  angles, i.e. where the  $E_{T,miss}$  trigger element is reconstructed from the part of the hadronic final state which is not disappearing in the beam pipe. The inefficiency at low  $p_{T,miss}$  and high  $\gamma_h$  angles (low  $Q^2$ , low  $x$ ) rises due to relatively high energy thresholds against noise in the central detector region.

Figure 5.14 shows the trigger efficiencies as function of  $x$  for various values of  $Q^2$ . The inefficiencies at low  $Q^2$  and high  $x$  has the same origin as for low  $p_{T,miss}$  and low  $\gamma_h$ , i.e. limited by the detector acceptance. In the same way the inefficiency at low  $Q^2$  and low  $x$  is caused by the high energy thresholds against the noise in the LAr calorimeter.

The CC MC events are reweighted with the trigger efficiencies determined from the PSCC events.

### Systematic uncertainty

The systematic uncertainty on the trigger efficiencies in each  $(x, Q^2)$  bin is determined in a similar way to previously performed CC analyses, e.g. [126]. The uncertainty depends on the efficiency in the  $(x, Q^2)$  bin and the statistical error of the PSCC sample used, and is given by:  $15\%(1 - \varepsilon) \oplus Err_{PSCC}^{stat}$ . For the present analysis,  $Err_{PSCC}^{stat}$  was determined to be 1%.

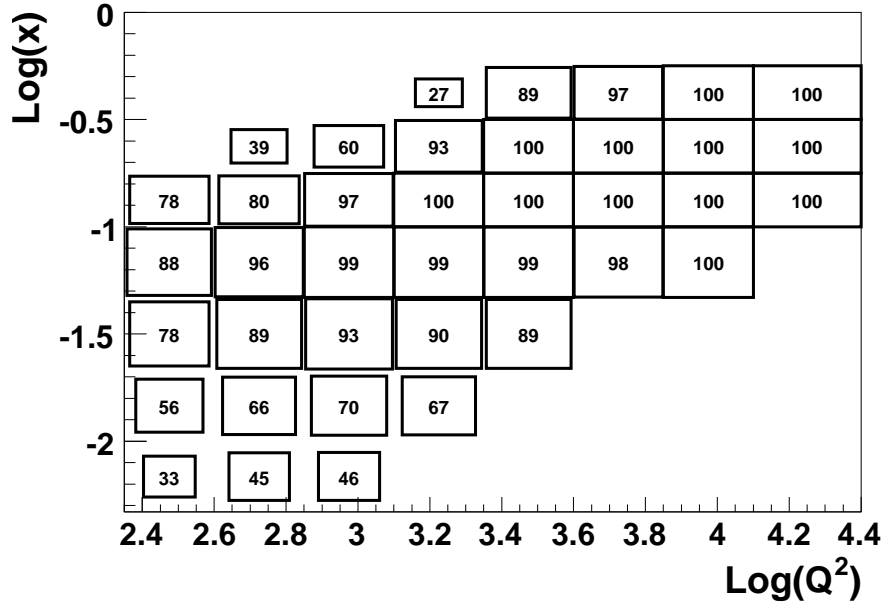


Figure 5.12: Trigger efficiencies in  $(x, Q^2)$  bins as determined for the right handed (R) CC sample.

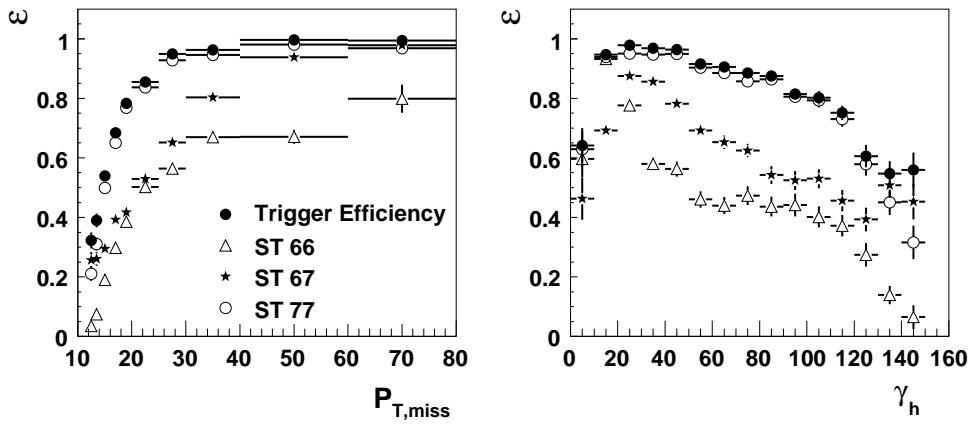


Figure 5.13: Trigger efficiencies as function of the transverse missing momentum  $p_{T,miss}$  (left) and hadronic angle  $\gamma_h$  (right) as determined for the right handed (R) CC sample. The solid symbols show the combined trigger efficiency (S66||S67||S77).

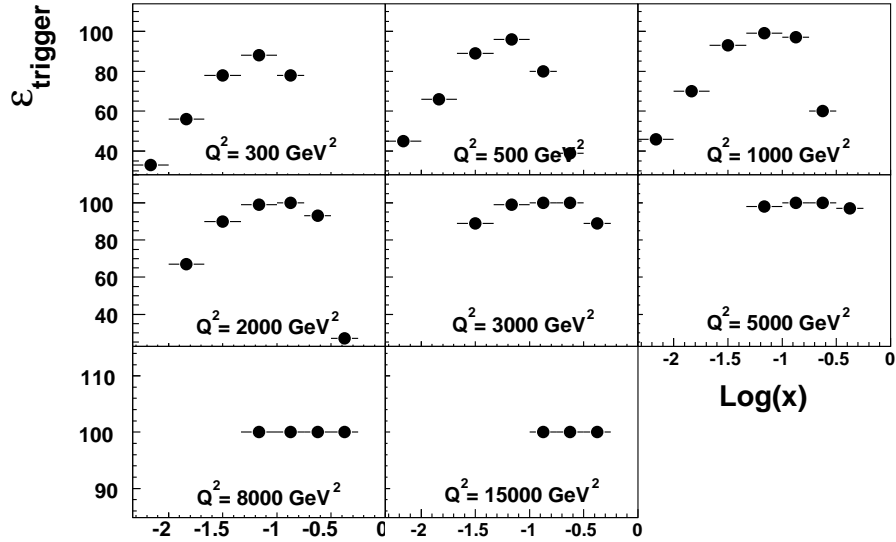


Figure 5.14: *Trigger efficiencies as function of  $x$  for different  $Q^2$  values. The efficiencies shown are for the right handed (R) CC sample.*

### 5.2.2 Vertex Requirement Efficiency

The distribution of the interaction vertex for CC data events is determined by the central tracker for  $-35 \text{ cm} < z_{\text{vertex}} < 35 \text{ cm}$  (see chapter 5.1.3). The data interaction vertex has to be modelled accurately by the Monte Carlo (see section 4.2). Moreover, the central vertex efficiency has to be described by the simulation.

Again the PSCC data events are used to determine the interaction vertex efficiency<sup>4</sup>. The central vertex requirement efficiency as function of  $y_h$  is presented in Figure 5.15 (a). As can be seen from the figure, the vertex efficiency in the high  $y_h$  region is close to 100% but decreases rapidly towards low  $y_h$  where the acceptance of the central drift chamber is limited. The vertex efficiency determined from MC events is also shown in Figure 5.15. From the efficiency ratio in Figure 5.15 (b) a difference up to 20% is observed between PSCC events and the CC simulation (the lowest bin in the efficiency plot can be ignored as it is outside of the analysis cut  $y_h > 0.03$ ).

The published measurement of the total charged current cross sections of the 2003-04 data [13] by a large part is based on the analysis described in this thesis. For the publication, a large systematic uncertainty of the vertex requirement efficiency was assigned from the efficiency ratio of PSCC data and CC MC as observed in Figure 5.15 (b).

<sup>4</sup>As there were no significant variations observed for the vertex requirement efficiency of the L and R data samples, the efficiency was determined for the whole data period.

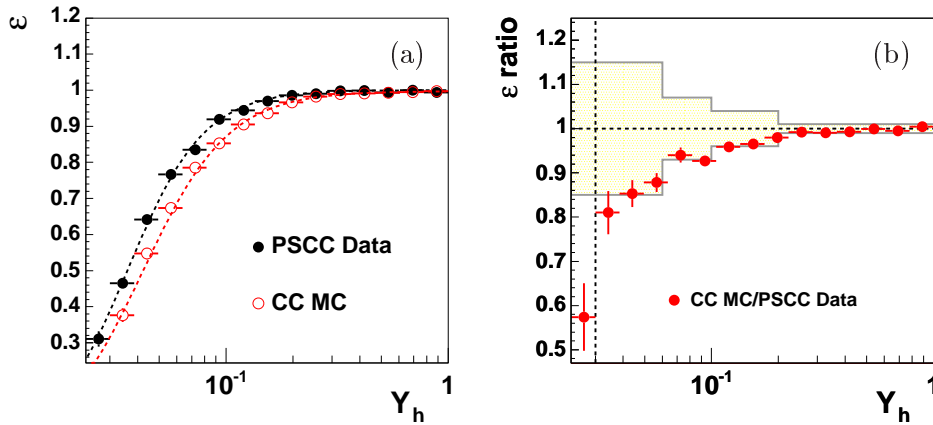


Figure 5.15: (a) Vertex requirement efficiencies of the PSCC data and CC MC events as function of  $y_h$ ; (b) ratio of vertex efficiencies with the assigned  $y_h$  dependent systematic uncertainty: 15% for  $y_h < 0.06$ , 7% for  $0.06 < y_h < 0.1$ , 4% for  $0.1 < y_h < 0.2$ , 1% for  $0.2 < y_h < 1.0$ . The vertical dashed line indicates the analysis cut of  $y_h > 0.03$ .

Many studies were performed in order to understand the origin of this difference (some of these checks are discussed further down in this section).

An important fact realised during these studies was that the central vertex reconstruction of the PSCC events is not exactly the same as the reconstruction in the CC data and CC MC simulation:

- in the pseudo charged current algorithm the vertex is determined using reconstructed tracks remaining after the electron removal;
- the central vertex in the original reconstruction (data and simulation) is determined using primary event information, mainly hits in the central drift chamber<sup>5</sup>.

In order to have consistent samples to determine the vertex efficiency as well as to study different vertex reconstruction properties, also the neutral current Monte Carlo events have been modified to pseudo charged current events (PSCC MC). A good agreement of the  $z$  vertex distributions between PSCC data and PSCC MC samples is observed in Figure 5.16 (a). However, due to the different vertex reconstruction methods, the positive  $z$  values of the charged current MC at  $z \gtrsim 40$  cm are generally higher than in pseudo charged current events (Figure 5.16 (b)).

<sup>5</sup>The hit information is not available in the PSCC events due to limitations in data storage and access speed.

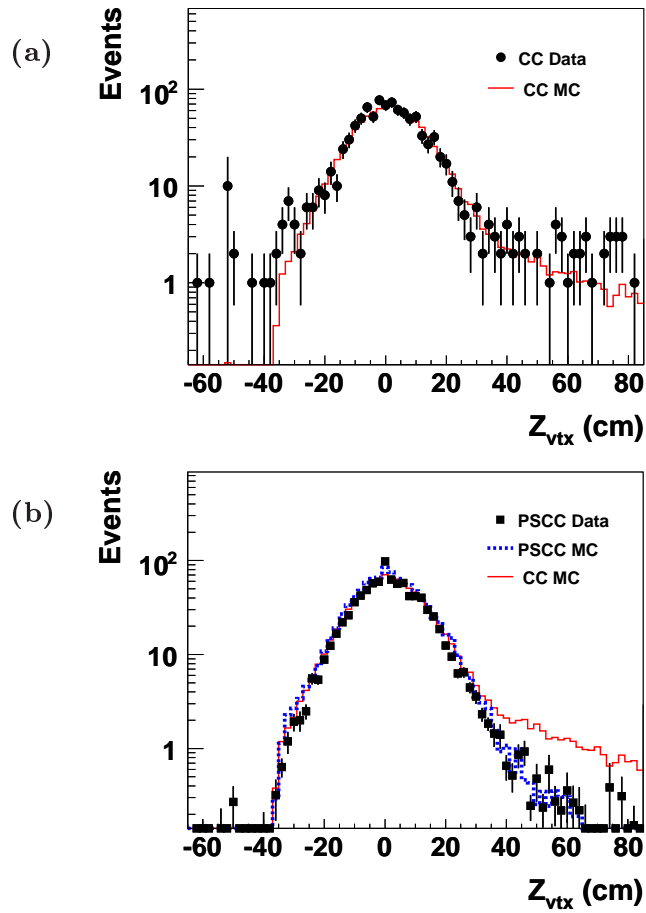


Figure 5.16: (a) Distribution of the  $z$  vertex for the 2003-04 CC data and CC Monte Carlo events; (b)  $z$  vertex distribution of PSCC data, PSCC MC and CC MC events.

A potential reason for the vertex efficiency difference in the CC and PSCC (neutral current) simulations is related to radiative effects:

- as described in section 1.2.3, the photon radiation in the CC Monte Carlo events includes three terms: The photon radiation from the "incoming" lepton (initial state radiation, ISR), the photon radiation from the exchanged  $W^\pm$ , and some part of the photon radiation from the final state, i.e. "outgoing" quark ( $q_{out}$ ). The interference of the included  $q_{out}$  part with other terms is taken into account. Terms which account for the remaining radiation from the outgoing quark and virtual loop corrections on the quark line are neglected as argued in [40];

- contrary to the CC MC, in the NC Monte Carlo events the photon radiation from the outgoing quark is not accounted for. Clearly, photon radiation from the  $W^\pm$  does not exist in NC MC events. In addition, there are photons radiated from the scattered electron (Final State Radiation, FSR) which do not exist in the CC events.

The polar angle ( $\Theta$ ) distribution of the radiated photons in PSCC and CC MC events is shown in Figure 5.17. The PSCC MC distribution in this figure is corrected for the FSR, i.e. for the presence of the photons radiated from the scattered electron. As noted in Figure 5.17, the photons radiated in the backward region (at large polar angles) are emitted by the incoming electron (ISR). The distributions of ISR photons are similar for CC MC and PSCC MC events. The photons observed in the central and forward region (small polar angles) in CC MC are emitted by the outgoing struck quark and the  $W$ . The forward photons are not observed in the PSCC MC events.

The discussed differences concerning radiative effect may lead to differently reconstructed kinematic variables in PSCC and CC MC events and thus affect the vertex efficiencies.

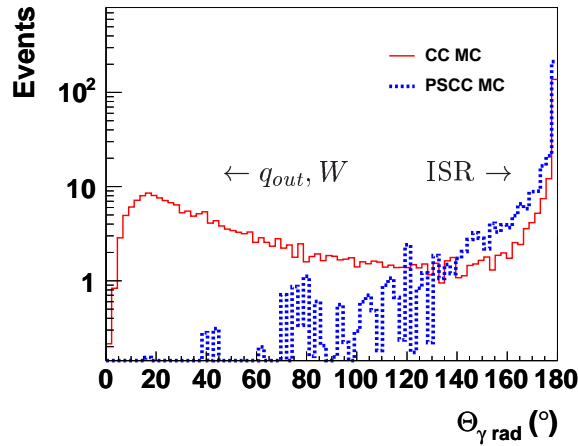


Figure 5.17: *Distribution of the polar angle ( $\Theta$ ) of radiated photons in CC MC and PSCC MC events.*

To study a possible influence of the radiative effects on the vertex requirement efficiency in CC and PSCC simulated events, non-radiative Monte Carlo events were generated for CC and NC interactions, i.e. the photon radiation off the lepton line was switched off during event generation. The PSCC technique was then applied to the non-radiative NC MC events and the vertex efficiency was determined from the produced non-radiative PSCC simulated events. The ratio of the vertex efficiency for the usual radiative PSCC MC and non-radiative PSCC MC events is shown in Figure 5.18. The observed

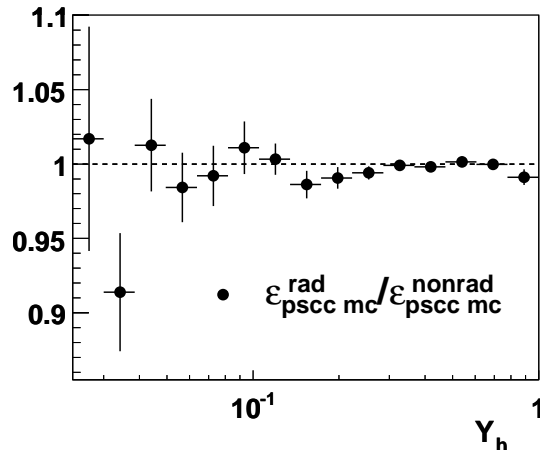


Figure 5.18: *Ratio of the vertex requirement efficiencies determined from PSCC MC generated ignoring photon radiation off the lepton line and the usual radiative PSCC (i.e. NC) simulated events.*

difference in vertex efficiency for radiative and non-radiative PSCC events is small (typically below 2% as can be seen in Figure 5.18). The conclusion can be drawn from this study<sup>6</sup>, that radiative effects are not the reason for the large vertex efficiency difference between CC MC and PSCC events observed in Figure 5.15.

After many other studies it has finally been found that the vertex fitting algorithm was not fully adjusted to PSCC events: For those events for which the vertex refitting procedure failed (vertex mismatch in the  $xy$  plane, for example), the "original", i.e. NC event vertex value was taken. This means, that up to 4% of PSCC events had vertex values determined by the scattered electrons of the original NC events. The electron usually leaves a clear isolated track in the detector which is used to determine a precise event vertex position (see NC studies performed in [115], for example).

After the modification of the vertex fit algorithm, the new vertex efficiency was determined for PSCC (data and MC) and CC MC events. As seen in Figure 5.19, a clear improvement of agreement in the vertex requirement efficiency between PSCC data and CC MC is observed. One should note that small differences in the sources (tracks and hits) used for vertex refitting algorithm for PSCC and CC MC events still remain and thus some difference in the vertex efficiencies may stay. This remaining difference, however, is covered by the systematic uncertainty which is given below.

<sup>6</sup>The influence of the radiative effects to other CC selection efficiencies was studied and found to be negligible.

The results of the performed studies can be summarised as follows:

- good agreement of the vertex distributions was observed for CC data and CC MC events (Figure 5.16 (a)),
- disagreement of the vertex distributions was observed for CC data and PSCC events at  $z \gtrsim 40 \text{ cm}$  (Figure 5.16 (b)),
- good agreement of the vertex distributions was found for PSCC data and PSCC MC events (Figure 5.16 (b)),
- reasonable agreement of the vertex efficiencies for CC MC and PSCC events was found after modifying the vertex algorithm (Figure 5.19),
- due to different methods used to reconstruct the event vertex position in CC MC and PSCC events, some small differences of the vertex efficiency remain between PSCC data and CC MC (and thus between PSCC MC and CC MC) (Figure 5.19). The remaining difference is used to determine the systematic uncertainty of the interaction vertex requirement.

### Systematic uncertainty

As the difference between vertex requirement efficiencies for PSCC data and CC MC events increases towards low  $y_h$  values, a  $y_h$  dependent systematic uncertainty was chosen from Figure 5.19 (b): 15% for  $y_h < 0.05$ , 6% for  $0.05 < y_h < 0.15$  and 1% for  $0.15 < y_h < 1.0$ .

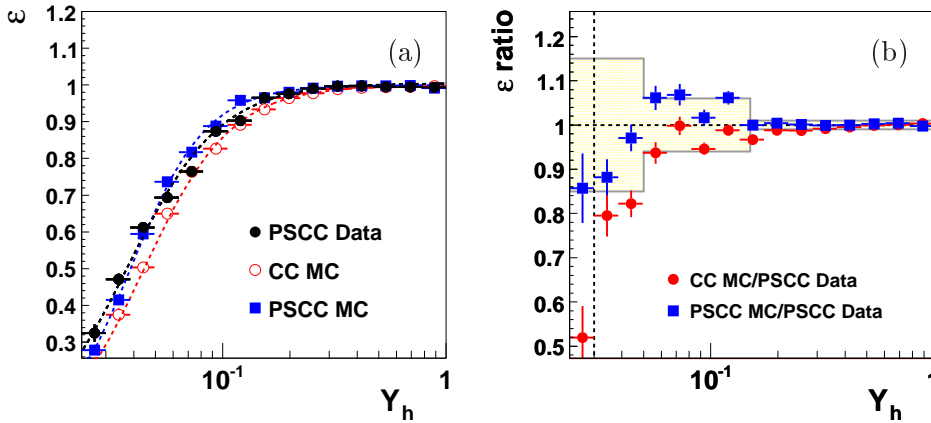


Figure 5.19: (a) Vertex requirement efficiencies as function of  $y_h$  for PSCC data, CC MC and PSCC MC events; (b) ratio of vertex efficiencies of CC MC and PSCC data events. The applied systematic uncertainties: 15% for  $y_h < 0.05$ , 6% for  $0.05 < y_h < 0.15$  and 1% for  $0.15 < y_h < 1.0$  (shown as shaded bars). The vertical dashed line indicates the analysis cut of  $y_h > 0.03$ .



### 5.2.3 $ep$ Background Rejection Efficiency

#### $\gamma p$ background rejection

The inefficiency due to  $\gamma p$  suppression cuts was determined from the PSCC events and compared with the efficiency determined from CC simulation<sup>7</sup>. As shown in Figure 5.20, the efficiencies of the  $\gamma p$  suppression cuts for PSCC and CC MC are in good agreement over the whole  $x_h$  region. Detailed studies have been performed to evaluate systematic uncertainties rising from the  $ep$  induced background.

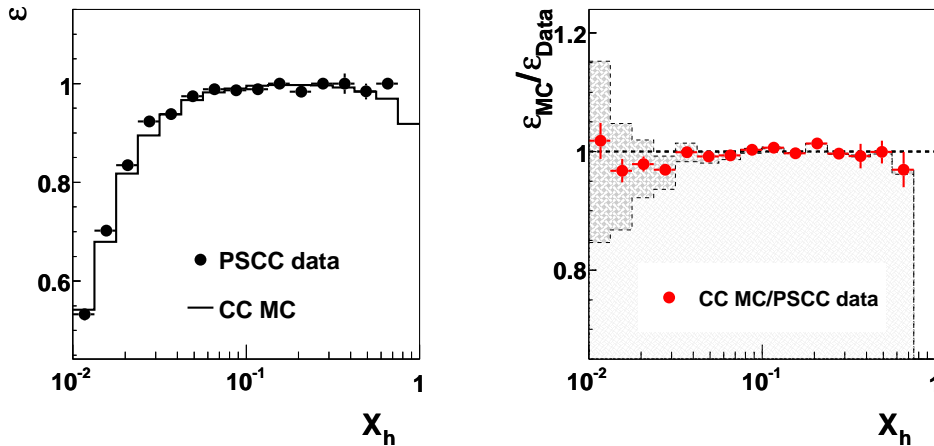


Figure 5.20: Efficiencies of the  $\gamma p$  background suppression cuts for the PSCC data and CC MC events as function of  $x_h$ . The dashed area represents changes in the efficiency of the CC MC due to a systematic variation of the variable  $V_{ratio}$  by  $\pm 0.02$ .

#### Systematic uncertainty

There are two sources of systematic uncertainties for the  $ep$  induced background: The uncertainty from the cuts against photoproduction ( $V_{ratio}$ ,  $p_{T,h}$ ) and the uncertainty of the subtracted  $ep$  background ( $\gamma p$ ).

The first uncertainty is estimated by varying  $V_{ratio}$  variable by  $\pm 0.02$  and, by the same amount, varying the 2 dimensional  $V_{ratio} - p_{T,h}$  cut in the simulation. The effect of the  $V_{ratio}$  variation to the efficiency of the  $ep$  background suppression is shown in Figure 5.20 (b). The corresponding effect on the cross section is discussed in chapter 6.

The second uncertainty is determined from a comparison of data and  $\gamma p$  simulation in the region where the background dominates, i.e. with relaxed  $\gamma p$

<sup>7</sup>The efficiency of the  $ep$  background suppression cuts was determined for the whole 2003-04 data period.

suppression cuts. As shown in Figure 5.21 (a), good agreement is observed in the  $V_{ratio}$  distributions for the CC data and  $\gamma p$  simulated background.

The other method to estimate the systematic uncertainty of the subtracted  $\gamma p$  background is to use the electron tagger (ET, see chapter 2.2). ET is used to identify  $\gamma p$  events by measuring the scattered electron in the data and in the simulated photoproduction processes. Data and simulation events were selected in the tagger acceptance region  $0.4 < y_e < 0.85$ . In addition, the average ET acceptance (determined for a given analysis period) was taken into account for the simulation. To suppress the overlap with the Bethe Heitler events, an energy in the photon tagger (PT, chapter 2.2) was required to be less than  $2 \text{ GeV}$ .

The method showed good agreement of the  $V_{ratio}$  distributions for tagged data and photoproduction events (Figure 5.21 (b), detailed studies performed in [120]). For the remaining differences observed in the  $V_{ratio}$  distributions a systematic uncertainty of 30% on normalisation of the  $ep$  background subtraction has been chosen (shown as the shaded area in Figure 5.21). The effect on the uncertainty to the CC cross section is smaller than 1%.

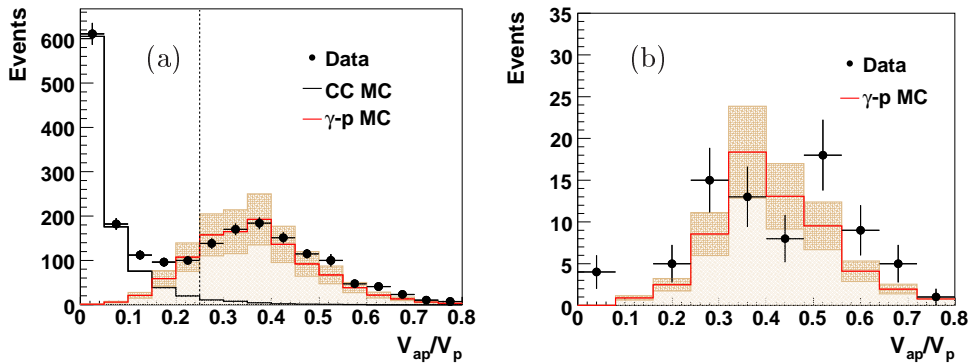


Figure 5.21: (a) Distribution of variable  $V_{ratio}$  for the CC data, CC MC and  $\gamma p$  simulated events after all CC selection cuts except for 2-dimensional  $V_{ratio} - p_{T,h}$  cut. The dashed line indicates the analysis cut of  $V_{ratio} < 0.25$ ; (b)  $V_{ratio}$  distribution for tagged CC data and  $\gamma p$  simulated events after all CC selection cuts except for 2-dimensional  $V_{ratio} - p_{T,h}$  cut. The shaded bars show the 30% systematic uncertainty chosen for the  $ep$  background subtraction (see text).

### Neutral current background rejection

The total inefficiency induced by all NC suppression cuts in the PSCC and CC MC events was estimated to be below 0.5% in the present analysis and was therefore neglected. However, a 10% systematic uncertainty was assigned to the NC background suppression (this results in an effect smaller than 1% to the total CC cross section, see section 6.3).

#### 5.2.4 Non- $ep$ Background Rejection Efficiency

The background finders are applied to both the data and the simulation. The efficiency of the background finders is determined from the PSCC events and from the simulated events separately<sup>8</sup>.

The efficiencies for the background finders  $Ibg$ ,  $Ibgfm$  and  $Ibgam$ , determined as function of the hadronic angle  $\gamma_h$  from the PSCC and CC MC events, are shown in Figure 5.22. As seen in the figure, the efficiency of the background finders is close to 100% for a wide range of  $\gamma_h$  but typically decreases for very low  $\gamma_h$  values where the detector acceptance is limited. The efficiency at high  $\gamma_h$  values is influenced by limited number of events and the edge of the LAr calorimeter acceptance. However, the difference between the efficiencies of PSCC and simulated events is below 5% everywhere.

As the differences of the individual efficiencies for each background finder classes are small, the total efficiency is determined for all background finders together. The resulting efficiency determined from PSCC events was used to adjust the efficiency in the simulation: The MC events were reweighted with the factor  $w$  defined for each  $(x, Q^2)$  bin as:

$$w(x, Q^2) = \varepsilon_{bgf}^{PSCC} / \varepsilon_{bgf}^{CC MC}$$

Here,  $\varepsilon_{bgf}^{PSCC}$  and  $\varepsilon_{bgf}^{CC MC}$  are the efficiencies of the background finders determined from PSCC and CC MC, respectively.

The ratio of the non- $ep$  background finder efficiencies as function of  $y_h$  for PSCC data and CC MC events before and after the MC reweighting is shown in Figure 5.23.

The procedure to derive the systematic uncertainty for the background finder cuts is described at the end of this section.

---

<sup>8</sup>Non- $ep$  background rejection efficiencies were determined for the whole 2003-04 data period.

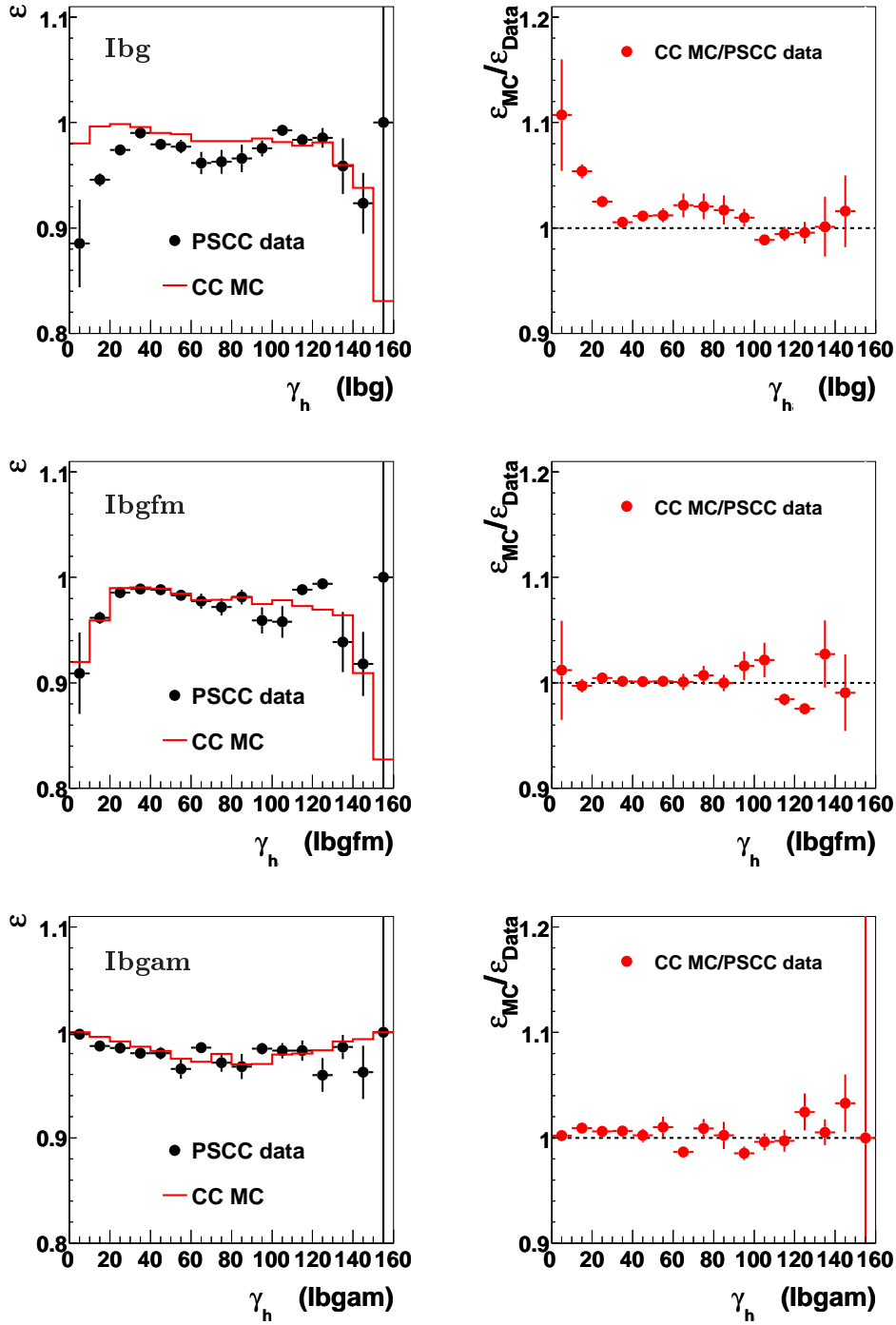


Figure 5.22: Efficiencies of *Ibg* (top), *Ibgfm* (middle) and *Ibgam* (bottom) non-ep background finders for PSCC and Monte Carlo events (left) as function of  $\gamma_h$  and the ratio between them (right).

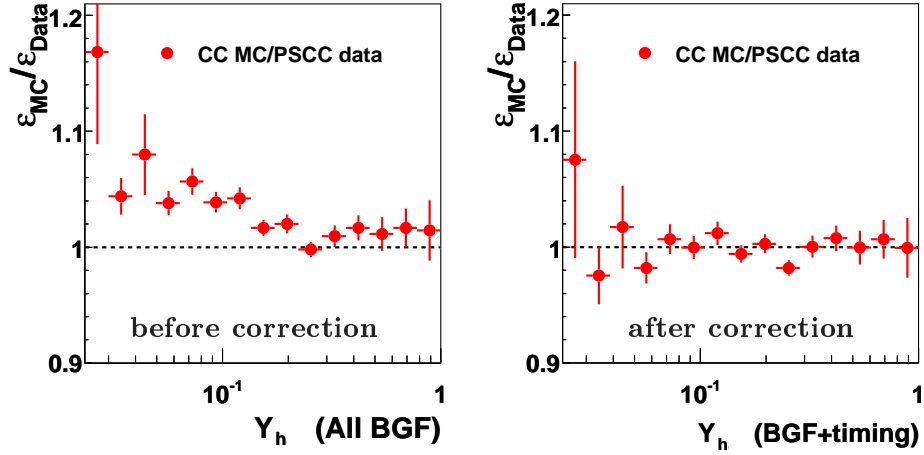


Figure 5.23: Ratio of the non- $ep$  background finder efficiencies as function of  $y_h$  for PSCC and CC MC: Before correcting MC efficiency to the PSCC efficiency (left) and after (right).

### Timing requirement efficiency

In order to make a reliable estimation of the timing efficiency, the PSCC code was modified. The change of code was required in order to apply the calibration of the LAr  $T_0$  signal to PSCC events as it is applied to the CC data [127]. After the modification of PSCC code, the full reconstruction of LAr trigger timing signal became possible and thus the calibration of the LAr  $T_0$  in PSCC events. The distribution of the LAr  $T_0$  in PSCC events before and after the calibration is shown in Figure 5.24.

The total inefficiency of the CC timing requirements in PSCC data was found to be 1.7% for both timing cuts (LAr and CJC). The timing requirement efficiency determined from PSCC data was used to adjust the CC simulation in each  $(x, Q^2)$  bin.

### Systematic uncertainty

In order to determine common systematic uncertainty, the timing requirement efficiency was combined with the non- $ep$  background finder efficiency (see Figure 5.25). An uncertainty of 2% for  $y_h < 0.1$  and 1% for  $y_h > 0.1$  has been chosen from Figure 5.25 and applied in the present analysis.

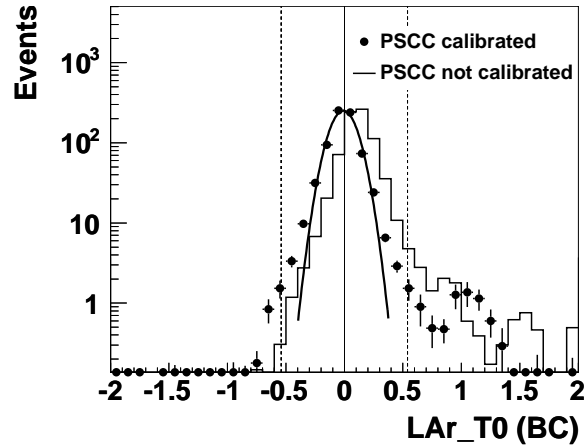


Figure 5.24: *Distribution of the LAr T0 signal in PSCC data events before and after the LAr T0 calibration. The central part of the calibrated PSCC distribution is well described by a Gaussian. The dashed lines indicate the timing cut ( $|T0_{LAr}| \leq 0.54$  BC) which corresponds  $\approx 5\sigma$  of the distribution.*

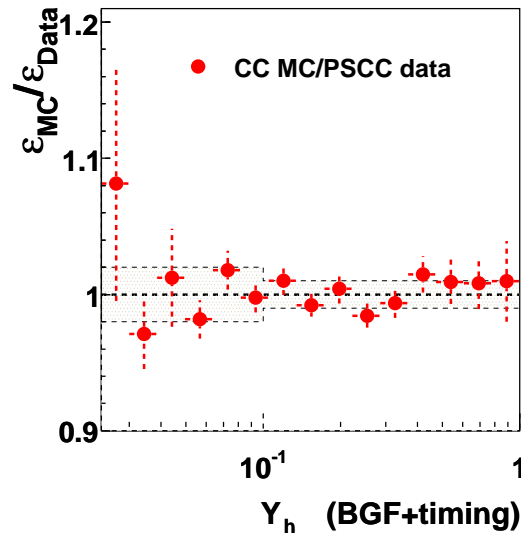


Figure 5.25: *Non-ep background finder efficiency combined with the event timing requirement for PSCC and CC Monte Carlo events as function of  $y_h$ . The lines represent the systematic uncertainty as determined from the remaining efficiency differences: 2% for  $y_h < 0.1$  and 1% for  $y_h > 0.1$ .*

### 5.3 Final Charged Current Event Samples

The number of the selected charged current events together with the corresponding Monte Carlo expectations and the measured background contributions for L and R positron running periods are given in Table 5.5.

	L $e^+$	R $e^+$
CC data	220	679
CC MC expectation	221.9	649.1
background MC	16.9	22.2

Table 5.5: *Final charged current samples selected in this analysis.*

The distributions of several kinematic quantities ( $p_T$ ,  $Q^2$ ,  $E - p_z$ ,  $x$ ) for the selected charged current events are shown in Figure 5.26 and Figure 5.27 for L and R data sets, respectively. Good agreement between the distributions for CC data and simulation is found. As the rate of background events does not depend on the positron polarisation, the relative background contribution in the L data set is larger.

As mentioned in chapter 4, an important data quality check is the stability of the detector with time. The numbers of CC events per  $1 \text{ nb}^{-1}$  luminosity ("event yield"), corrected to zero polarisation, are shown as function of the run number in Figure 5.28. As in the NC case (Figure 4.1), the yields of both CC samples were found stable with time.

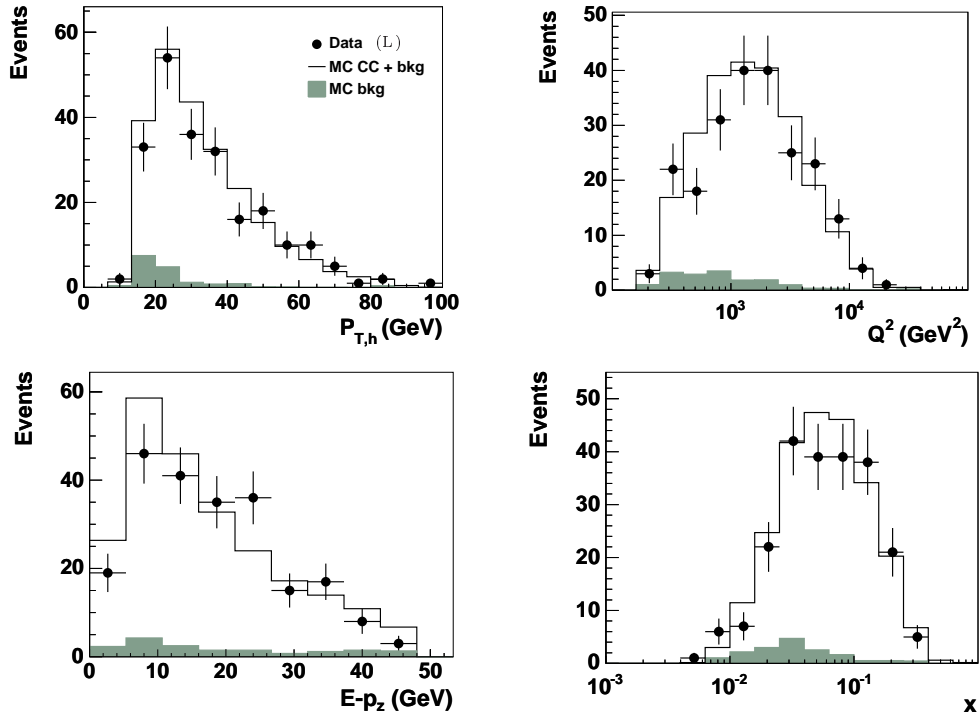


Figure 5.26: Distributions of the kinematic variables  $p_T$ ,  $Q^2$ ,  $E - p_z$  and  $x$  for the left handed CC data together with expectations for the full simulation, taking into account all efficiencies. The contribution of the simulated background is shown as well.



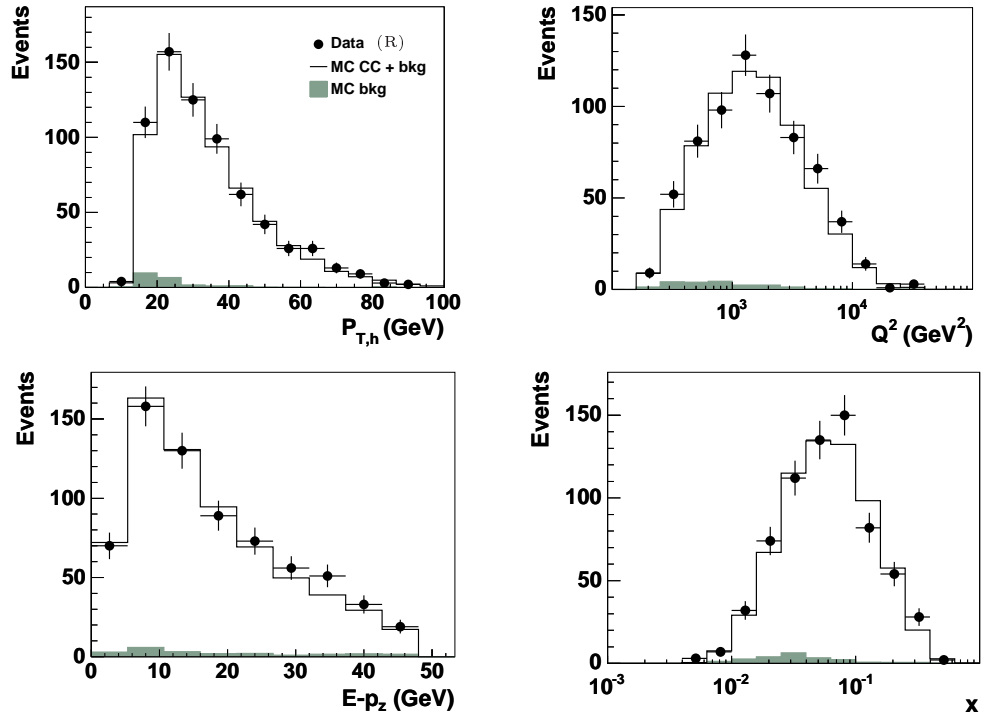


Figure 5.27: Distributions of the kinematic variables  $p_T$ ,  $Q^2$ ,  $E - p_z$  and  $x$  for the right handed CC data together with expectations for the full simulation, taking into account all efficiencies. The contribution of the simulated background is shown as well.

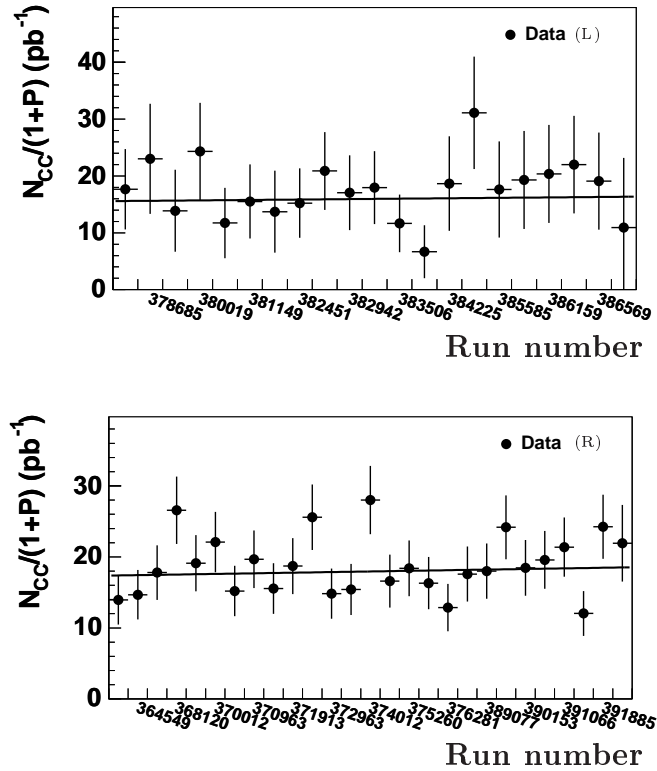


Figure 5.28: Event yield of L (top) and R (bottom) charged current events divided by  $(1 + P_e)$  as function of the run number. The lines are linear fits for a given period with a  $\chi^2/\text{dof} = 0.6$  and 1.1 for the L and R handed CC samples, correspondingly.

## Chapter 6

# Charged Current Cross Section Measurement

The procedure to measure the cross sections for the deep inelastic charged current scattering process is described in this chapter.

The kinematic  $(x, Q^2)$  plane is divided into bins for the cross section determination. The size of each bin is optimised according to the resolution and certain quality criteria (acceptance, purity and stability). The cross section is calculated from the measured number of events in the data and the corresponding simulated events in the  $(x, Q^2)$  bins. The simulation is corrected for detector acceptance and all efficiencies are taken into account. The discussion of the systematic uncertainties is presented at the end of this chapter.

### 6.1 Definition of $(x, Q^2)$ Bins

The binning in the  $x$  and  $Q^2$  plane for the determination of the charged current cross section is defined with equidistant bins in  $\log_{10}(x)$  and  $\log_{10}(Q^2)$ . The sizes of the bins are defined taking into account the statistical precision of the measurement and the resolution of the kinematic quantities. The cross sections are measured at the bin center values.

The definition of the  $(x, Q^2)$  bins used in this analysis follows the binning used in the previous published inclusive measurements, e.g. [126].

#### Bin boundaries:

$\log_{10}(Q^2)$	2.35	2.60	2.85	3.10	3.35	3.60	3.85	4.10	4.40
$Q^2 \text{ GeV}^2$	224	398	708	1259	2239	3981	7080	12589	25119
$\log_{10}(x)$	-2.33	-2.00	-1.67	-1.33	-1.00	-0.75	-0.50	-0.25	0.00
$x$	0.005	0.010	0.021	0.047	0.100	0.178	0.316	0.562	1.000

Bin center values:

$\log_{10}(Q^2)$	2.48	2.70	3.00	3.30	3.48	3.70	3.90	4.18
$Q^2 \text{ GeV}^2$	300	500	1000	2000	3000	5000	8000	15000
$\log_{10}(x)$	-2.10	-1.89	-1.50	-1.10	-0.89	-0.60	-0.40	-0.19
$x$	0.008	0.013	0.032	0.080	0.130	0.250	0.400	0.650

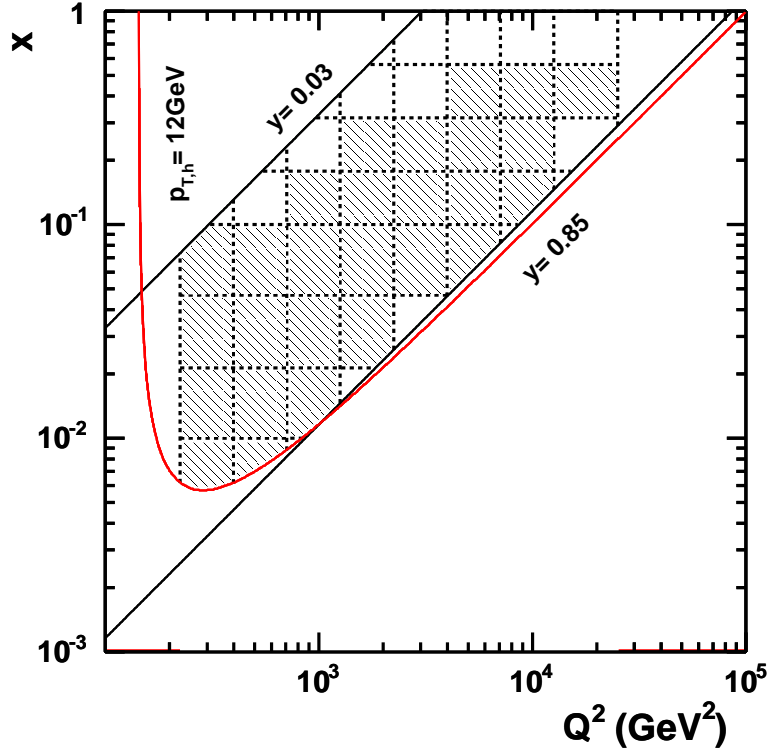


Figure 6.1: Kinematic plane in  $x$  and  $Q^2$  for the charged current measurement. The dashed lines represent bin boundaries, the solid lines are limits defined by the  $y$  and  $p_{T,h}$  cuts. The bins used for the CC cross section measurement, i.e. satisfying the  $P$  and  $S$  quality requirements (see text), are shown as the dashed areas.

The kinematic plane in  $x$  and  $Q^2$  is further restricted by the cuts  $0.03 < y < 0.85$  and  $p_{T,h} > 12 \text{ GeV}$ , corresponding to the requirements applied in this analysis (see section 5.1.3). The kinematic plane for the CC measurement is shown in Figure 6.1.

Additional quality criteria for the selection of bins are given by the *Acceptance* ( $A$ ), *Purity* ( $P$ ) and *Stability* ( $S$ ) determined from Monte Carlo simulation. These variables are calculated as follows:

$$A_i = \frac{N_i^{rec}}{N_i^{gen}} \quad (6.1)$$

$$P_i = \frac{N_i^{gen+rec}}{N_i^{rec}} \quad (6.2)$$

$$S_i = \frac{N_i^{gen+rec}}{N_i^{gen+rec(all)}} \quad (6.3)$$

where

- $N_i^{gen}$  is the number of generated MC events in the bin  $i$  (events must also satisfy the  $y$  and  $p_{T,h}$  requirements),
- $N_i^{rec}$  is the number of reconstructed MC events in the bin  $i$  (events must also satisfy all CC selection requirements),
- $N_i^{gen+rec}$  is the number of generated and reconstructed MC events in the bin  $i$ ,
- $N_i^{gen+rec(all)}$  is the number of MC events generated in the bin  $i$  and reconstructed in any bin.

The *Acceptance* is a fraction of reconstructed events over the generated in the bin  $i$ . However, events may migrate from bin to bin. For example, if the number of events migrated out from the bin  $i$  is replaced by the same amount of events migrated in from other bins,  $A$  stays 100%. Such effects are quantified by the *Purity*, i.e. the fraction of events generated and reconstructed in the same bin  $i$ . Finally, the *Stability* accounts for the generated events which were reconstructed in bins other than  $i$ .

In order to be able to trust the quality criteria which are entirely determined from simulated events, it is important to verify good agreement between data and simulation (for the agreement in the present analysis see chapter 4).

*Acceptance*, *Purity* and *Stability* as function of  $x$  at fixed values of  $Q^2$  are presented in Figure 6.2 for the L and R CC samples. The decrease of  $S$  and  $P$  in the high  $x$  region is caused by the loss of final state particles in the beam pipe. The effect becomes smaller with the increase of  $Q^2$ . The low  $x$  region (high  $y$ ) is affected by the poor resolution of the hadron reconstruction method (see chapter 3).

The measurement of CC cross sections was performed only in those bins where  $P$  or  $S$  are larger than 30%. The bins used for the CC measurement, i.e. fulfilling  $P$  or  $S$  quality criteria, are shown in Figure 6.1 with the dashed area<sup>1</sup>.

<sup>1</sup>The CC cross sections were not measured at  $Q^2 = 15000 \text{ GeV}^2$  in the present analysis as no CC events were found in the correspond bins.

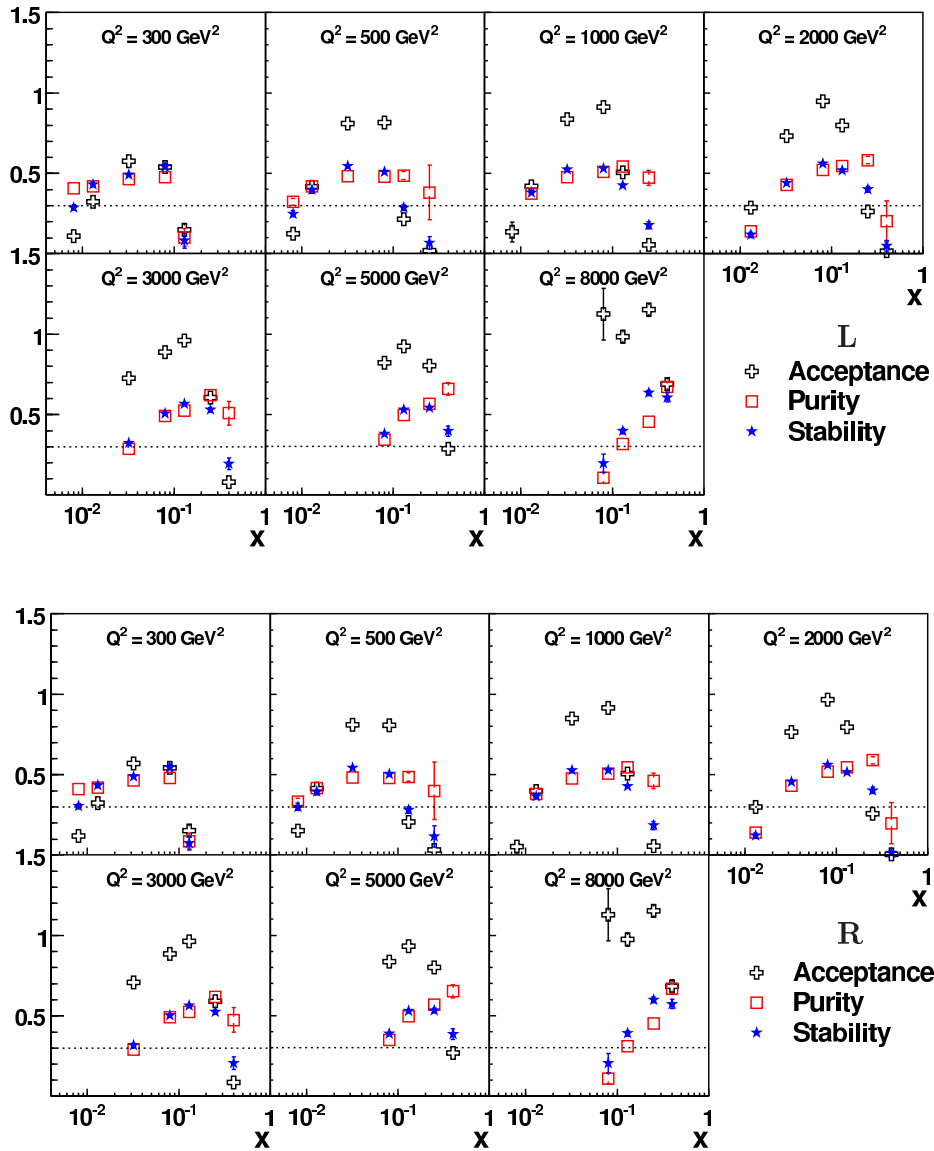


Figure 6.2: Acceptance ( $A$ ), Purity ( $P$ ) and Stability ( $S$ ) as function of  $x$  for various values of  $Q^2$  as determined in the present charged current analysis for the left (top) and right (bottom) handed CC samples. Typically, the errors are smaller than the symbol size. Only bins where  $P$  and  $S$  greater than 30% are used for the cross section measurement (indicated by the dashed line).

## 6.2 Cross Section Calculation

The general formula to measure the cross section in a given  $(x, Q^2)$  bin is:

$$\sigma^* = \frac{N^{data} - N^{bgr}}{\mathcal{L}^{data} A} \delta^{bc} \frac{1}{1 + \delta^{rc}}. \quad (6.4)$$

Here,  $\sigma^*$  represents the total, single differential and double differential cross sections, i.e.  $\sigma^* = \sigma_{tot}, \frac{d\sigma}{dQ^2}, \frac{d\sigma}{dx}, \frac{d^2\sigma}{dx dQ^2}$ ,

$N^{data}$  is the number of data events selected in a bin,

$N^{bgr}$  is the number of simulated background events selected in a bin,

$\mathcal{L}^{data}$  is the integrated luminosity (see section 2.1),

$A = \frac{N^{rec}}{N^{gen}}$  is the detector acceptance as defined in the equation 6.1 and determined from MC including radiative corrections,

$\delta^{bc}$  is a correction factor for the cross section to account for the shift from the finite size bin to the bin center position ("bin center correction"). It is determined from the theoretical cross section prediction at the bin center  $(x_{i,c}, Q_{i,c}^2)$  and the integrated cross section over the same bin  $i$ :

$$\delta_i^{bc} = \frac{\left. \frac{d^2\sigma}{dx dQ^2} \right|_{x=x_{i,c}, Q^2=Q_{i,c}^2}}{\int_{x_{i,min}}^{x_{i,max}} \int_{Q_{i,min}^2}^{Q_{i,max}^2} \frac{d^2\sigma}{dx dQ^2} dx dQ^2},$$

$\delta_i^{rc}$  is a radiative correction estimated by the Monte Carlo simulation (see section 1.2.3):

$$\delta_i^{rc} = \frac{\sigma^{rad}}{\sigma^{Born}} - 1.$$

The acceptance, bin center and radiative corrections are obtained from the Monte Carlo simulation of the CC reactions. The radiative effects are calculated using HERACLES [50] as implemented in DJANGO [48]. The cross section formula 6.4 can be simplified to:

$$\sigma^* = \frac{N^{data} - N^{bgr}}{N^{MC}} \frac{\mathcal{L}^{MC}}{\mathcal{L}^{data}} \sigma_{MC}^* \quad (6.5)$$

were  $N^{MC}$  is the number of reconstructed MC events in a bin and  $\mathcal{L}^{MC}$  is the luminosity of the MC sample. Similar to equation 6.4,  $\sigma_{MC}^*$  represents the total, single differential and double differential cross sections of the theory.

### 6.3 Systematic Uncertainties

Systematic uncertainties are separated into correlated and uncorrelated ones, depending on their correlation between the cross section  $(x, Q^2)$  bins. Those errors which can cause a systematic shift, common to all measured cross section values are treated as *correlated*, the hadronic energy scale which may differ from the "true" energy equally over all detector regions and thus over all bins, is a typical example. The *uncorrelated* errors originate from the local inefficiencies depending on the detector performance. For example, the hadronic energy measurement also depends on the calorimeter performance and therefore may differ in certain calorimeter regions. Thus the uncertainty of the hadronic energy measurement has both correlated and uncorrelated components, i.e. the uncertainty is treated to be partially correlated and partially uncorrelated.

The separation of uncertainties in correlated and uncorrelated is relevant for comparisons of theoretical expectations with the data (see section 7.1).

Systematic uncertainties to the cross section measurement were determined from the simulated events varying each of the uncertainty sources (listed below) by the amount estimated from the studies discussed in chapter 4. The resulting errors on the cross section found to be symmetric to a good approximation and are listed in Table 6.1 for the total CC cross section measurement.

The systematic uncertainties on the charged current cross section measurements are:

- A 2% uncertainty is assigned to the hadronic energy measured in the LAr calorimeter, 1% of which is assumed to be correlated (section 4.1).
- A 10% correlated uncertainty is assigned to the energy identified as noise in LAr calorimeter (section 4.1).
- A correlated uncertainty due to variation of the variable  $V_{ratio}$  by  $\pm 0.02$  (section 5.2.3).
- A 30% correlated uncertainty on the subtracted photoproduction background (section 5.2.3).
- A 10% correlated uncertainty on the subtracted NC (section 5.2.3), and 20% on the other  $ep$  backgrounds [128] (lepton pair and  $W$  production, see section 1.3).
- A  $y$  dependent uncorrelated uncertainty introduced by non- $ep$  background finders (section 5.2.4):
  - 2% for  $y_h < 0.1$ ,
  - 1% for  $y_h > 0.1$ .



- A  $y$  dependent uncorrelated uncertainty of the vertex finding efficiency (section 5.2.2):
  - 15% for  $y_h < 0.05$ ,
  - 6% for  $0.05 < y_h < 0.15$ ,
  - 1% for  $0.15 < y_h < 0.1$ .
- An uncertainty on the trigger efficiency is determined as a quadratic sum of the trigger inefficiency and the statistical error of PSCC events used for the efficiency determination:  $15\%(1 - \varepsilon) \oplus Err_{PSCC}^{stat}$ .  
The first uncertainty component is assumed to be correlated. The statistical error of PSCC events,  $Err_{PSCC}^{stat}$ , is considered to be uncorrelated and was estimated to be 1% in this analysis (section 5.2.1).
- An uncorrelated uncertainty due to QED radiative corrections (see section 1.2.3) was estimated in [129] and on average is smaller than 2% (depending on the kinematic region). The uncertainty on the radiative corrections is determined by comparing  $\delta_i^{rc}$  obtained from various numerical programs which slightly differ in the implementation of  $O(\alpha)$  and higher order QED corrections.
- A 0.5% correlated uncertainty is related to the variation of the different choice of PDFs used in the MC simulation. The uncertainty was estimated using several commonly used PDFs (e.g. MRSH [53], CTEQ [55]) to derive charged current cross sections.

A global uncertainty of 1.3% is considered on the luminosity measurement, out of which 0.5% is assumed as correlated.

The absolute uncertainty of 1.1% and 0.7% on the mean polarisation is considered for the L and R data samples, respectively.

The total systematic error on the cross section is obtained adding the individual uncertainties in quadrature. The total error of the measurement is formed by adding the total systematic and statistical (determined from the number of data events) errors in quadrature.

For the measurement of the total CC cross section the uncertainty on the luminosity is included in the total systematic uncertainty but the polarisation error is not (see discussion in section 7.1). In the single and double differential cross section measurement the normalisation uncertainty of the luminosity is not considered in the total systematic uncertainty but the uncertainty of polarisation is included.

The summary of all uncertainties with the effects to the total cross section measurements is shown in Table 6.1.

<i>systematic uncertainty</i>	<i>variation</i>	<i>effect on <math>\sigma_{tot}</math></i>
hadronic scale	$\pm 2\%$	1.3%
noise subtraction	$\pm 10\%$	0.3%
trigger efficiency	$\pm(15\%(1 - \varepsilon) \oplus Err_{PSCC}^{stat})$	2%
vertex efficiency	<i>y</i> dependent	2.1%
$V_{ap}/V_p$ cut	$\pm 0.02$	0.6%
statistical error of CC MC		0.5%
$\gamma p$ bkg subtraction	$\pm 30\%$	(0.5 – 1)%
NC bkg subtraction	$\pm 10\%$	< 0.1%
rest <i>ep</i> bkg subtraction	$\pm 20\%$	< 0.3%
background finders	<i>y</i> dependent	1.1%
radiative corrections		0.8%
total systematic uncertainty		(3.6 – 3.7)%
luminosity		1.3%

Table 6.1: *The list of all systematic uncertainties and estimated effects to the total charged current cross section.*

# Chapter 7

## Results

The  $e^+p$  charged current cross sections measured with left and right handed positrons in the beam (polarised cross sections) allow to perform novel tests of the electroweak part of the Standard Model.

The cross sections in this chapter are presented in the following order: The total CC cross section  $\sigma_{CC}^{tot}$ , the  $Q^2$  dependence of the CC cross section  $d\sigma/dQ^2$ , the  $x$  dependence of the CC cross section  $d\sigma/dx$  and the CC cross section measured double differentially,  $d^2\sigma/dxdQ^2$ .

The polarised cross sections were found to be in agreement with the Standard Model expectation, i.e. proportional to the positron polarisation (see equation 1.46). Thus the results can be combined into an unpolarised cross section measurement with the better statistical precision. This also gives an improved access to the QCD observables and allows direct comparisons with previous H1 CC measurements.

The numerical values of all CC cross sections of the present measurement together with the systematic uncertainties are summarised in Appendix A, Tables A.4-A.9.

### 7.1 Polarised CC Cross Sections

The most interesting measurement, testing the electroweak model, is the polarisation dependence on the total charged current cross sections. It is a first such measurement at high  $Q^2$ . The measured polarisation dependence allows direct tests of the electroweak sector of the Standard Model which predicts a linear dependence of the cross section on  $(1 + P_e)$  in a  $V - A$  type theory.

### 7.1.1 Polarisation Dependence of the Total CC Cross Section

The measurement of the total charged current cross sections,  $\sigma_{CC}^{tot}$ , was performed in the kinematic region  $Q^2 > 400 \text{ GeV}^2$  and  $y < 0.9$ <sup>1</sup>.

The measured total CC cross sections for two values of the longitudinal positron polarisation  $P_e$  are presented in Table 7.1. In the table also the unpolarised CC total cross section, based on  $65.2 \text{ pb}^{-1}$  of data and collected in the years 1999-2000 [18], is given.

$P_e(\%)$	$\sigma_{CC}^{tot} \text{ (pb)}$	SM expectation (pb)
-40.2	$14.16 \pm 1.08_{stat} \pm 0.56_{syst}$	$15.69 \pm 0.3$
0	$28.44 \pm 0.77_{stat} \pm 0.85_{syst}$	$26.3 \pm 0.4$
+33.6	$35.58 \pm 1.47_{stat} \pm 1.35_{syst}$	$35.08 \pm 0.6$

Table 7.1: *The total CC cross section values measured in the region  $Q^2 > 400 \text{ GeV}^2$  and  $y < 0.9$  together with the expectations of the Standard Model.*

The labels *stat* and *syst* in Table 7.1 stand for the statistical and total systematic uncertainties. As discussed in 6.3 section, the luminosity error is included in the total systematic  $\sigma_{CC}^{tot}$  uncertainty, the polarisation error is not.

The unpolarised ( $P_e = 0$ ) cross section shown in Table 7.1 differs from the one in [18] in two respects: The  $Q^2$  cut is adopted to the present analysis (from  $Q^2 > 1000 \text{ GeV}^2$  to  $Q^2 > 400 \text{ GeV}^2$ ), and the uncertainty of the QED radiative corrections are reduced from 3% to 0.8% (based on [129]). The uncertainty of the luminosity measurement (1.5%) is included in the total systematic uncertainty of the unpolarised measurement.

For comparison, the expectations of the Standard Model for the measured cross sections are also given in Table 7.1. The uncertainties of the SM are combinations of the model errors and the errors of the experimental data entering into the H1 PDF 2000 fit. The measured charged current cross sections together with the SM predictions are shown in Figure 7.1.

In order to test the SM predictions of a linear polarisation dependence a linear fit has been performed to the three data measurements using a  $\chi^2$  minimisation (least squares) method. In the error matrix for the fit, the correlated systematic uncertainties (see section 6.2) are taken into account. The absolute error of the polarisation measurement was considered as independent uncertainty which is completely uncorrelated for the two measurements.

<sup>1</sup>The correction from the kinematic cuts ( $Q_h^2 > 400 \text{ GeV}^2$ ,  $0.03 < y_h < 0.85$ ,  $p_{T,miss} > 12 \text{ GeV}$ ) to the measured cross section region ( $Q^2 > 400 \text{ GeV}^2$  and  $y < 0.9$ ) was determined to be 1.063 using the H1 PDF 2000 parametrisation.

The linear fit results in a  $\chi^2 = 4.0$  for one degree of freedom. The fit extrapolated to the point  $P_e = -1$  yields a fully left handed charged current cross section of

$$\sigma_{CC}^{tot}(P_e = -1.0) = -3.3 \pm 2.3_{stat} \pm 0.6_{syst} \pm 0.8_{pol} \text{ pb}$$

This value is consistent with zero. The errors here correspond to the statistical (*stat*) and systematic (*syst*) uncertainties. There is an additional systematic uncertainty from the polarisation measurement (*pol*).

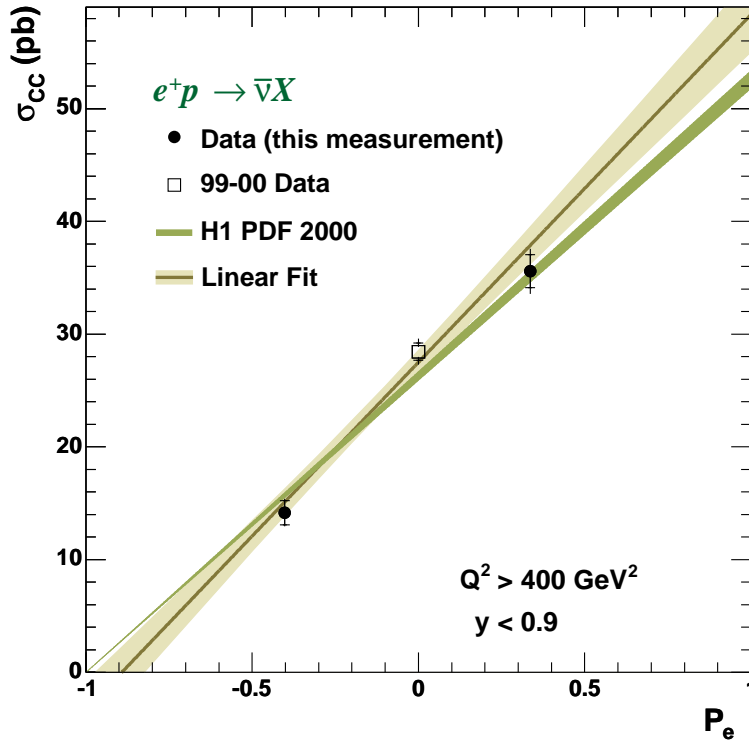


Figure 7.1: The  $e^+p$  CC cross section as function of the positron polarisation  $P_e$ . The full symbols represent this measurement, the open symbol represents the H1 1999-00 data. The inner error bars are the statistical, the outer ones the total errors. The (horizontal) errors on the polarisation measurement are smaller than the symbol sizes. Also shown is the prediction from the Standard Model using H1 PDF 2000 (see text) for the parton distribution functions (dark green shaded band). The linear fit to the data is shown as the dark line with a one-sigma error band.

From the uncertainties of the extrapolated cross section to the point  $P_e = -1$ , an upper limit of 2.24 pb at 95% confidence level (CL) is derived using a prescription, according to Feldman and Cousins [130].

The result obtained is consistent with the electroweak theory prediction of a vanishing cross section due to the  $V - A$  character (see section 1.1.5) of the weak charged current.

The upper limit of  $\sigma_{CC}^{tot}(P_e = -1)$  can be used to set a limit on the mass of a hypothetical right handed gauge boson  $W_R$ . Assuming that the total CC cross section is as a sum of R and L charged currents (mediated by  $W_L$  and  $W_R$ , respectively), i.e.  $\sigma_{CC}^{tot} = (1 + P_e)\sigma_{CC}^L + (1 - P_e)\sigma_{CC}^R$ , the extrapolated cross section upper limit 2.24 pb at  $P_e = -1$  can be directly used to determine the mass of  $W_R$ . For the calculation the assumptions of a massless right handed  $\nu_e$  and SM couplings were made. The result obtained excludes the existence of charged currents mediated by a right handed  $W_R$  of mass below 200 GeV at 95% CL.

The published measurement of the total CC cross sections [13] is the result of a common effort of two independent analysis groups at H1. A very good agreement of two independent cross section measurements was achieved and the results of both analyses were used in the publication.

The result of this analysis differs from the corresponding published [13] result of  $\sigma_{CC}^{tot}$  (at  $P_e = +33.6\%$ ) in the following aspect: Due to improved understanding of the difference of the vertex efficiency between pseudo CC and CC simulated events, the corresponding systematic uncertainties were reduced substantially (see section 5.2.2).

The measurement of the total CC cross section was also performed within the ZEUS collaboration [131]. Both results are presented in Figure 7.2. The linear fit of the ZEUS data provides a cross section [131] at  $P_e = -1.0$  of

$$\sigma_{CC}^{ZEUS}(P_e = -1.0) = 7.4 \pm 3.9_{stat} \pm 1.2_{syst} \text{ pb}$$

with the same error notation as above. The result obtained is consistent with the prediction of Standard Model as well.

Starting in 2005, the HERA machine is running with electrons instead of positrons. The  $e^-p$  data offer an additional possibility to test the electroweak part of the Standard Model. Like  $e^+p$  CC cross sections, the CC cross section for polarised  $e^-$  beam depends linearly on the longitudinal polarisation, but with a  $(1 - P_e)$  dependence. Thus the  $e^-p$  CC cross section vanishes at  $P_e = +1$ . The prediction for the  $e^-p$  CC total cross section, based on the H1 PDF 2000 parton distribution functions, is shown as a dashed line in Figure 7.2.

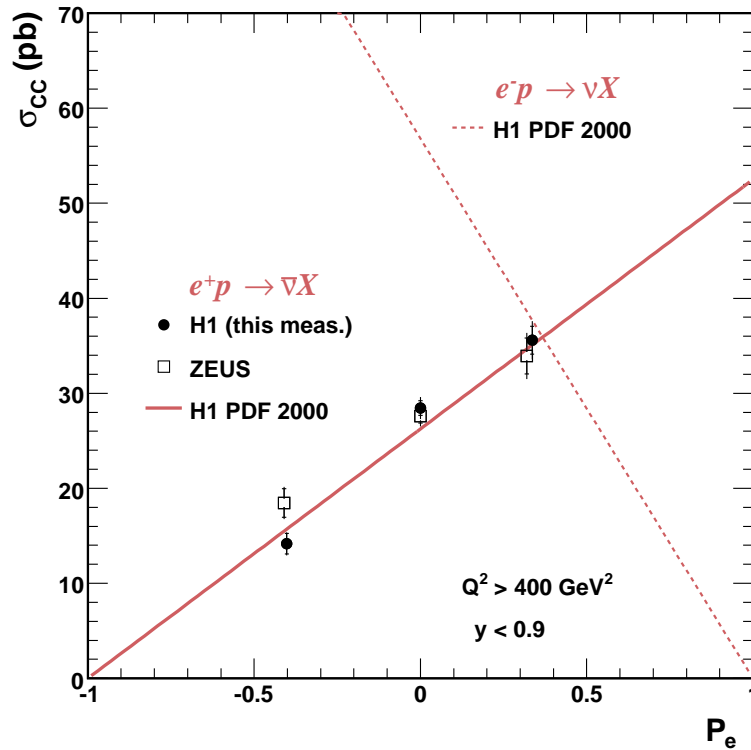


Figure 7.2: The  $e^+p$  CC total cross sections as function of  $P_e$  measured in this analysis (closed circles) and published by the ZEUS collaboration [131] (open boxes). The inner error bars represent the statistical, the outer ones the total errors. The horizontal errors on the polarisation measurement are smaller than the symbol sizes. Also shown is the prediction from the Standard Model based on the H1 PDF 2000 parton distribution functions for  $e^+p$  (line) and  $e^-p$  (dashed line).

### 7.1.2 The $Q^2$ Dependence of the Polarised CC Cross Section

The  $Q^2$  dependence of the polarised charged current cross sections was measured in the kinematic region  $y < 0.9$ <sup>2</sup>. The measured cross sections together with the SM predictions based on the H1 PDF 2000 parton distribution functions are shown in Figure 7.3 (note that the measurement of  $\sigma_{CC}^{tot}$  presented in the previous section does not include the value of  $d\sigma/dQ^2$  measured at  $Q^2 = 300 \text{ GeV}^2$ ). As seen in the figure, the measured cross sections agree well with the theory predictions over the entire  $Q^2$  range. However, a small difference in the region  $398 \text{ GeV}^2 < Q^2 < 708 \text{ GeV}^2$  was observed. The difference has been investigated and was shown to originate neither from detector effects nor from the data treatment [120]. Most likely, this is a statistical fluctuation (consistent within 2.6 standard deviations with the expectation). The cross section values of the  $d\sigma/dQ^2$  measurement are given in Appendix A, Tables A.2 and A.3.

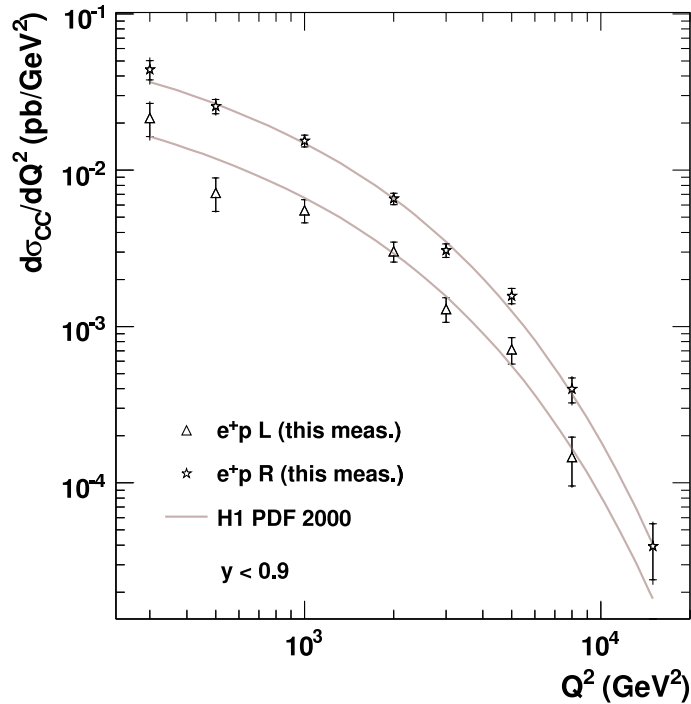


Figure 7.3:  $e^+p$  CC cross sections of two polarised ( $L$  and  $R$ ) measurements as function of  $Q^2$  for  $y < 0.9$ . For comparison, the SM predictions based on the H1 PDF 2000 parton distribution functions are shown.

<sup>2</sup>The factors estimating the influence to  $d\sigma/dQ^2$  due to changes in the kinematic region (from the analysis cuts to the cross section measurement) are given in Appendix B, Table B.1.



### 7.1.3 The $x$ Dependence of the Polarised CC Cross Section

The  $x$  dependence of the CC cross sections was measured in the kinematic region  $Q^2 > 1000 \text{ GeV}^2$  and  $y < 0.9$ <sup>3</sup>. The results together with the SM predictions are presented in Figure 7.4. The decrease of the theory expectations observed at low  $x$  values is a result of the kinematic cuts ( $Q^2 > 1000 \text{ GeV}^2$  and  $y < 0.9$ ).

The tabulated cross sections can be found in Appendix A, Tables A.5 and A.6.

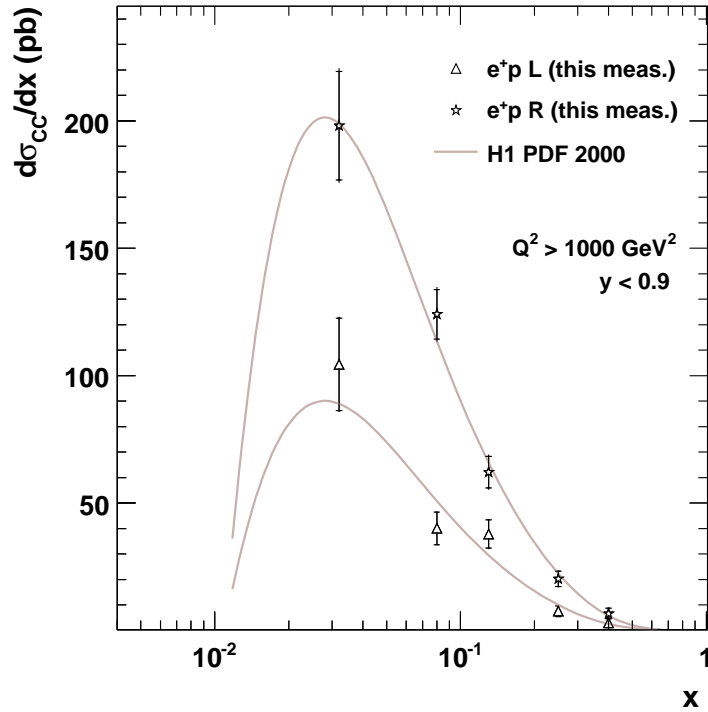


Figure 7.4: Polarised  $e^+p$  CC cross sections as function of  $x$ , measured in the kinematic region  $Q^2 > 1000 \text{ GeV}^2$  and  $y < 0.9$ . For comparison, the SM predictions based on the H1 PDF 2000 parton distributions are shown.

<sup>3</sup>The factors estimating the influence to  $d\sigma/dx$  due to changes in the kinematic region (from the analysis cuts to the cross section measurement) are given in Appendix B, Table B.2.

### 7.1.4 Polarised Double Different Cross Section

The measurement of the polarised double differential charged current cross sections,  $d^2\sigma/dxdQ^2$ , was performed in the region of  $300 \leq Q^2 \leq 15000 \text{ GeV}^2$  and  $0.013 \leq x \leq 0.65$ . The results of this measurement together with the theory predictions are presented in the form of reduced cross sections,  $\tilde{\sigma}_{CC}$ , (equation 1.39) which are directly related to the parton distribution functions, and are shown in Figure 7.5.

The measured double differential cross sections are interesting as the test of the electroweak part of Standard Model as well as an additional input to the existing H1 inclusive results for the extraction of the parton distributions of the proton (PDFs) by a next-to-leading order QCD fit.

The numerical values of  $d^2\sigma/dxdQ^2$  and  $\tilde{\sigma}_{CC}$  are tabulated in Appendix A, Tables A.8 and A.9.

## 7.2 Unpolarised CC Cross Sections

As discussed in section 1.2.1, the theory predicts a linear dependence of the CC cross sections on the positron beam polarisation (equation 1.46). The results discussed in the previous section showed a remarkable agreement of the CC cross sections for each (L and R) sample ( $\sigma_{CC}^{tot}$ ,  $d\sigma/dQ^2$ ,  $d\sigma/dx$  and  $d^2\sigma/dxdQ^2$ ) with the Standard Model expectations. Thus with the available statistical precision, the L and R charged current samples can be combined in order to measure an unpolarised CC cross section. Unpolarised CC cross sections are interesting for the following reason: The statistical error would be significantly reduced (although still remains the dominant uncertainty) and thus better precision can be offered to QCD analyses (i.e. the extraction of the parton distributions within the proton).

The combined L and R charged current sample (for characteristics of L and R data sets see Tables 5.1 and 5.5) was corrected for the remaining polarisation ( $P_{rest} = 1.49\%$ ) to a fully unpolarised data set which is determined as follows:

$$P_{rest} = \frac{\mathcal{L}_R P_R + \mathcal{L}_L P_L}{\mathcal{L}_R + \mathcal{L}_L}$$

Here,  $\mathcal{L}_R$  and  $P_R$  correspond to the integrated luminosity and polarisation of the R data sample, similarly  $\mathcal{L}_L$  and  $P_L$  are used for the L data set.

The integrated luminosity of the unpolarised data set is  $47.6 \text{ pb}^{-1}$ .

In the following, the unpolarised differential CC cross sections  $d\sigma/dQ^2$ ,  $d\sigma/dx$  and  $d^2\sigma/dxdQ^2$  are presented.

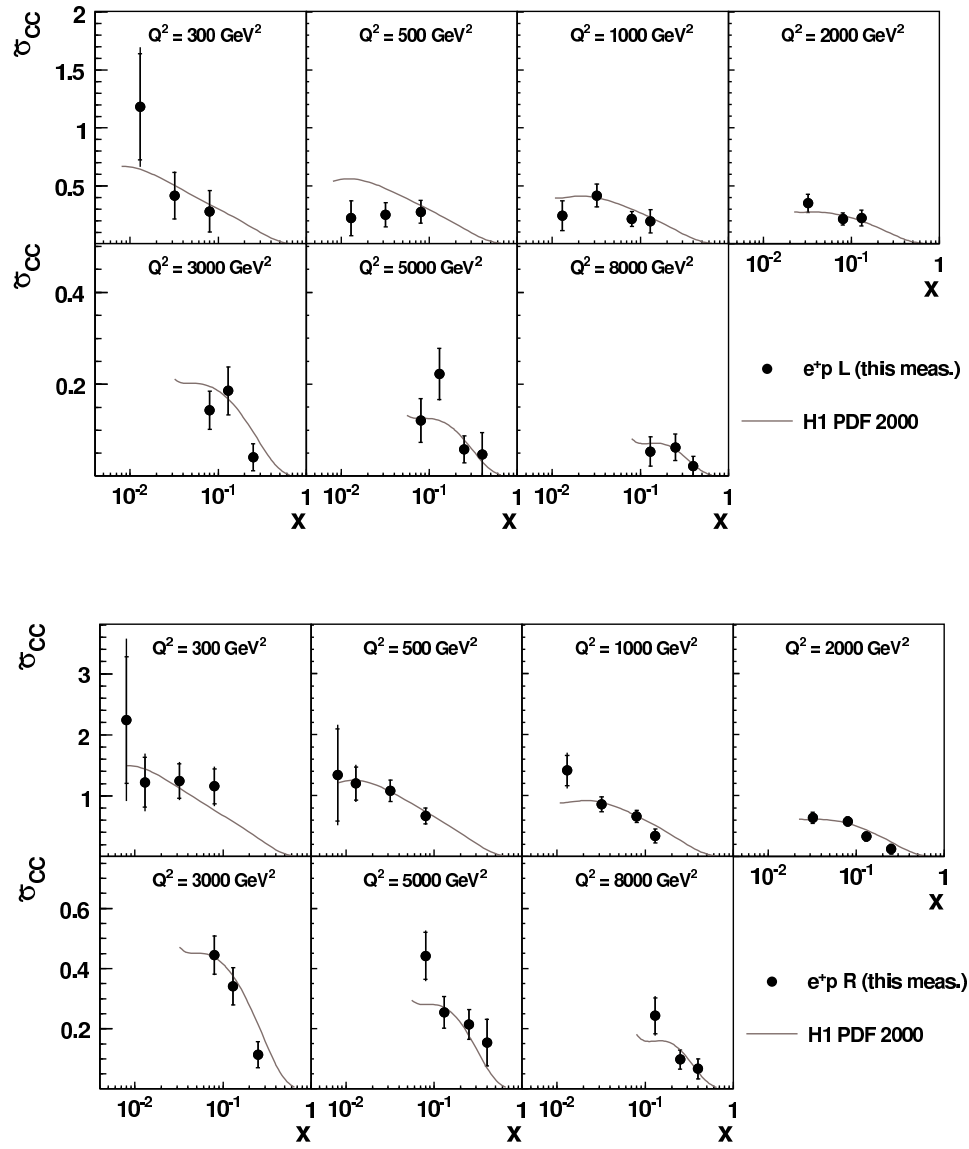


Figure 7.5: *The reduced polarised  $e^+p$  CC cross sections as function of  $x$  for different  $Q^2$  values of the left handed (top) and right handed (bottom) data. The theory expectation based on the H1 PDF 2000 parton distribution functions is also shown.*

### 7.2.1 The $Q^2$ Dependence of the CC Cross Section

The  $Q^2$  dependence of the unpolarised charged current cross sections was measured in the same kinematic region as the polarised one, i.e. for  $y < 0.9$ . The results are presented in Figure 7.3. The data are compared with predictions of the H1 PDF 2000 fit and show good agreement. The data to theory ratio is also given in Figure 7.6.

The numerical values of the cross sections are tabulated in Appendix A, Table A.1.

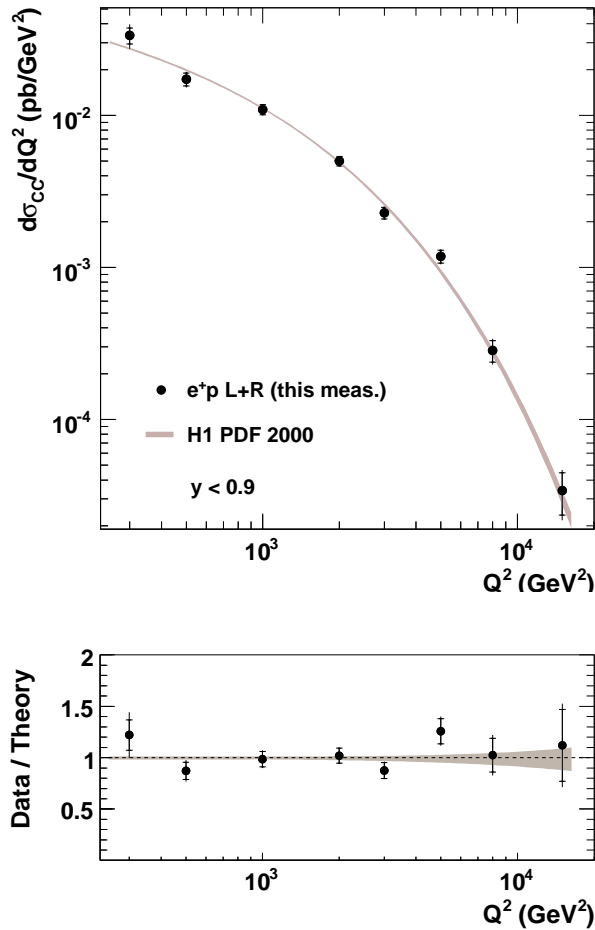


Figure 7.6: Unpolarised  $e^+p$  CC cross section as function of  $Q^2$  for  $y < 0.9$ . The band represents the uncertainty of the H1 PDF 2000 fit calculated by the adding in quadrature the experimental uncertainty as derived from the fit and the model uncertainty [18, 132]. The bottom plot shows the ratio of cross sections for data and theory.

Figure 7.7 shows the new results of the unpolarised differential CC cross section  $d\sigma/dQ^2$  together with corresponding the neural current cross section measured at H1 in the years 1999-2000 [18]. The NC cross section at low  $Q^2$  exceeds the CC cross section due the dominant photon exchange (the NC cross section increases towards low  $Q^2$  like  $1/Q^4$ ), whereas the CC cross section at low  $Q^2$  is suppressed by the  $W$  propagator mass ( $\sim [M_W^2/(Q^2+M_W^2)]^2$ ). However, the CC and NC cross sections approach each other in the region where  $Q^2$  is of comparable size with the weak intermediate vector boson masses ( $Q^2 \approx M_{Z(W)}^2$ ). This is a manifestation of the *electro-weak unification* (see section 1.2).

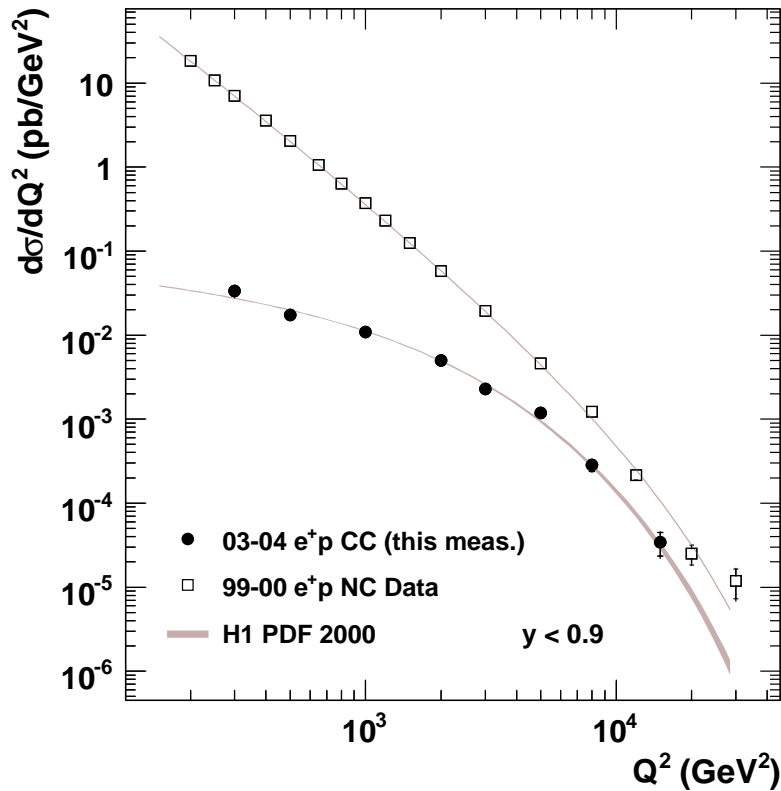


Figure 7.7: Unpolarised  $e^+p$  CC cross sections for data taken from the years 2003-04 (this analysis) and  $e^+p$  NC cross sections measured in the years 1999-00 [18] as function of  $Q^2$  for  $y < 0.9$ . The bands are theory expectations based on the Standard Model with parton density functions from H1 PDF 2000, determined as explained in Figure 7.6.

### 7.2.2 The $x$ Dependence of the CC Cross Section

Similarly to the polarised cross section, the kinematic cuts  $Q^2 > 1000 \text{ GeV}^2$  and  $y < 0.9$  were applied for the measurement of the unpolarised differential cross section  $d\sigma/dx$ . The  $x$  dependence of the unpolarised charged current cross section for data and theory is presented in Figure 7.8. The ratio of the cross sections for data and the H1 PDF 2000 predictions (Figure 7.8) shows good agreement between measured and predicted  $d\sigma/dx$  values.

The numerical values of the cross sections are tabulated in Appendix A, Table A.4.

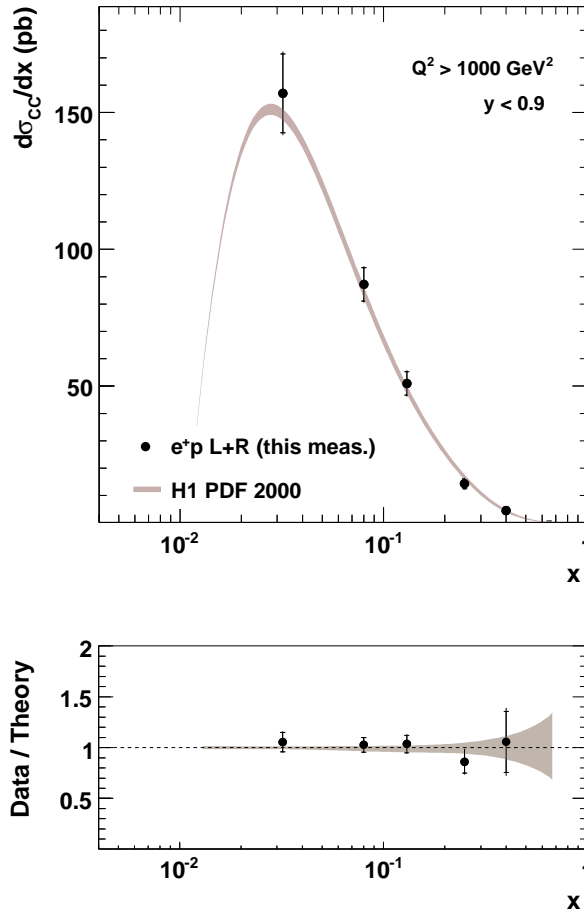


Figure 7.8: Unpolarised  $e^+p$  CC cross sections as function of  $x$  measured in the kinematic region  $Q^2 > 1000 \text{ GeV}^2$  and  $y < 0.9$ . The comparison of the cross sections of data and theory based on the H1 PDF 2000 parton distribution functions (band determined as explained in Figure 7.6), is also shown. The bottom plot shows the ratio of cross sections for data and theory.

### 7.2.3 Unpolarised Double Different Cross Section

The measurement of the unpolarised double differential CC cross section,  $d^2\sigma/dxdQ^2$ , was performed in the same kinematic region as the polarised one, i.e.  $300 \leq Q^2 \leq 15000 \text{ GeV}^2$  and  $0.013 \leq x \leq 0.65$ . The results together with the theory predictions are presented in Figure 7.9 in the form of the reduced cross section,  $\tilde{\sigma}_{CC}$  (equation 1.39).

The numerical values of  $d^2\sigma/dxdQ^2$  and  $\tilde{\sigma}_{CC}$  are tabulated in Appendix A, Table A.7.

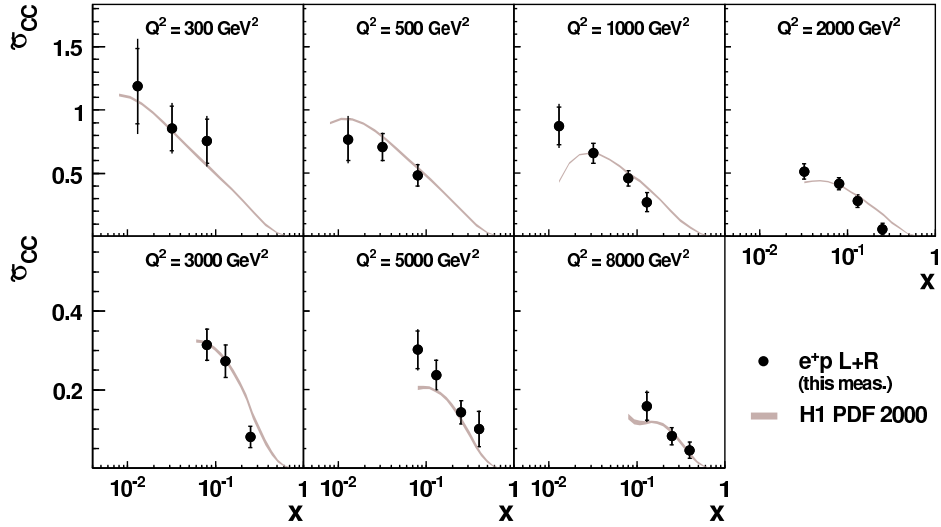


Figure 7.9: Unpolarised  $e^+p$  reduced charged current cross section as function of  $x$  for different values of  $Q^2$ . The model uncertainty based on the H1 PDF 2000 parton density functions is shown as the shaded band (determined as explained in Figure 7.6).

### Comparison with 1999-00 $e^+p$ Measurement at H1

The comparison of the unpolarised reduced CC cross section  $\tilde{\sigma}_{CC}$  with the previous unpolarised H1  $e^+p$  measurement [18] is presented in this section. The unpolarised measurement from [18] is based on data taken in 1999 and 2000 at a centre of mass energy  $\sqrt{s} = 319 \text{ GeV}$  (as in the present analysis), and correspond to an integrated luminosity of  $65.2 \text{ pb}^{-1}$  (luminosity of the present measurement is  $47.6 \text{ pb}^{-1}$ ).

The reduced CC cross sections are shown in Figure 7.10 (top). Good agreement is observed between the unpolarised 1999-00 measurement and the results of the present analysis performed with polarised positrons. Despite the fact that two analyses differ in the event selection requirements, a very reasonable agreement is observed between the cross sections.

The overall good agreement of the cross sections of both data measurements and the predictions of H1 PDF 2000 is also seen in the ratio plots shown in Figure 7.10 (bottom). The highest  $x$  cross section points are missing in this analysis due to low statistics (typically  $\leq 2$  events) but are present in the 99-00 measurement.



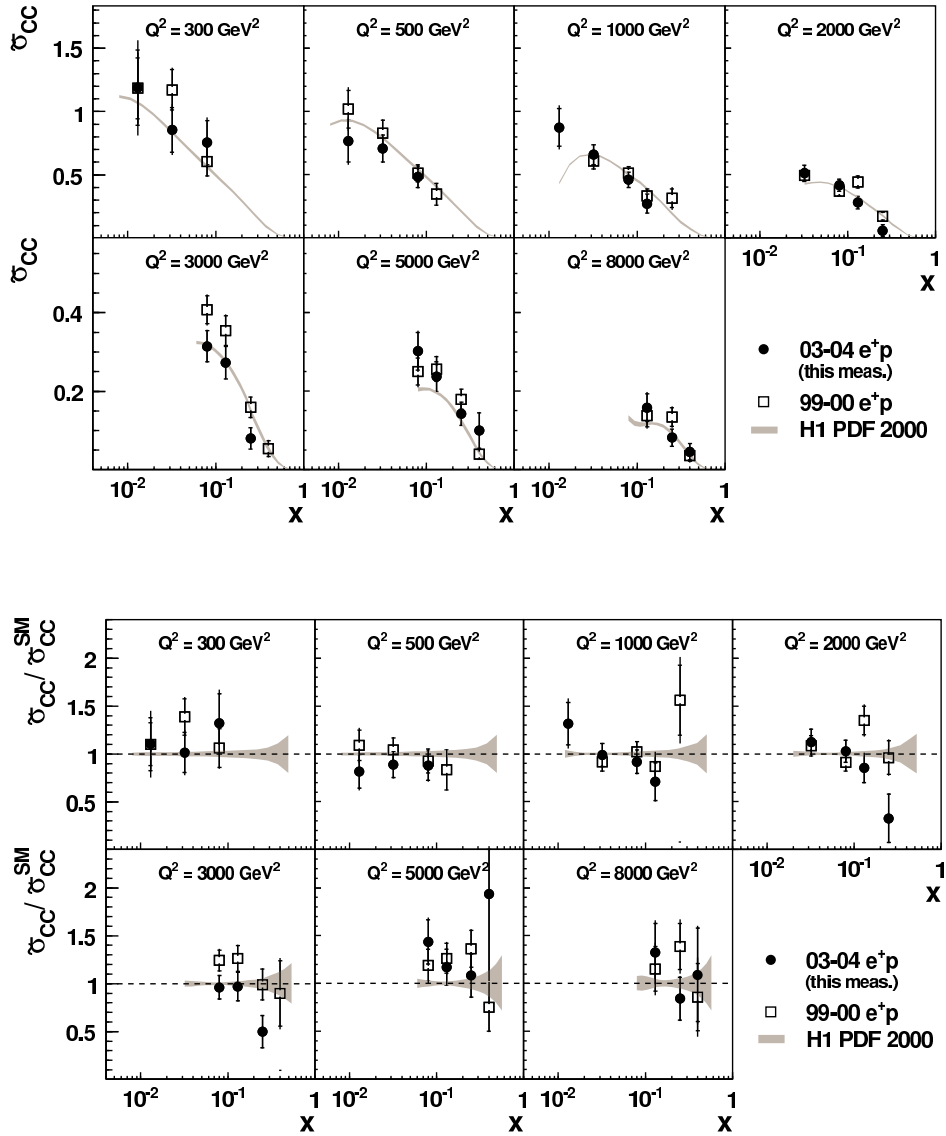


Figure 7.10: Reduced unpolarised  $e^+p$  charged current cross section  $\bar{\sigma}_{CC}$  of the present measurement (solid symbols) and previous H1 measurement published in [18] (open symbols) as function of  $x$  at different values of  $Q^2$ . The theory expectations based on the H1 PDF 2000 parton distribution functions are shown as bands (determined as explained in Figure 7.6).

### The Quark Distribution $x d$ at Large $x$

In the QPM, the  $e^+p$  CC reduced cross section  $\tilde{\sigma}_{CC}$  is a sum of quark distributions (see equation 1.44 in section 1.2.1):

$$\tilde{\sigma}_{CC} = x[\bar{u} + \bar{c}] + (1 - y)^2 x[d + s].$$

The various contributions of the quarks to the CC cross section can be calculated from the H1 PDF 2000 fit as described in [18, 132]. Figure 7.11 shows the reduced unpolarised CC cross section (from the beginning of this chapter) and the sum of all quark contributions (as predicted by the H1 PDF 2000 fit) as a band. As can be seen from Figure 7.11, the charged current cross section is dominated at large  $x$  by the  $d$  quark (its contribution is shown as the solid line). This provides a unique possibility to constrain the  $d$  quark distribution in a QCD fit, since the  $e^-p$  CC and  $e^\pm p$  NC cross sections are dominated at large  $x$  by the  $u$  quark distribution.

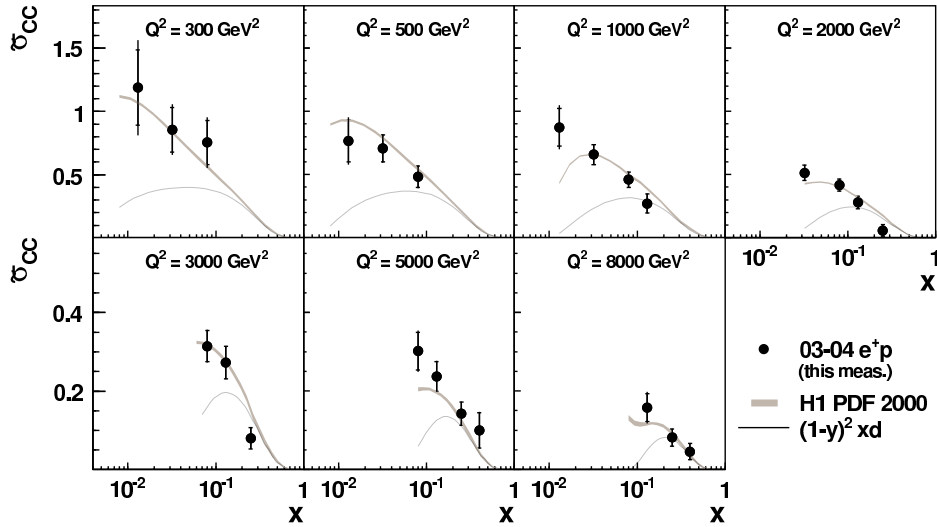


Figure 7.11: Unpolarised  $e^+p$  reduced charged current cross sections as function of  $x$  for various values of  $Q^2$  (same this analysis data as in Figure 7.9). Also shown are the expected contribution of the valence quark ( $xd$ ) indicated as a dark line. The model uncertainty (H1 PDF 2000) is shown as a shaded band.

## Chapter 8

# Summary and Outlook

Measurements of the  $e^+p$  deep inelastic charged current (CC) cross sections with the H1 detector at HERA have been presented in this thesis. The measurements are based on data taken in the years 2003-04 at a centre-of-mass energy  $\sqrt{s} = 319 \text{ GeV}$  with positrons of negative and positive longitudinal polarisation, corresponding to integrated luminosities of  $20.7 \text{ pb}^{-1}$  and  $26.9 \text{ pb}^{-1}$ , respectively. These are the first measurements of the polarisation dependence of the charged current cross sections at high four-momentum transfer squared  $Q^2$ .

The relevant aspects of the charged current analysis, especially the understanding of detector effects in the data and in the Monte Carlo simulations, have been developed in the thesis. To improve the triggering for the ongoing HERA running, the neural networks for the DIS event trigger rate reduction at the second H1 trigger level were provided.

The total and differential charged current cross sections,  $\sigma_{CC}^{tot}$ ,  $d\sigma/dQ^2$ ,  $d\sigma/dx$  and  $d^2\sigma/dxdQ^2$ , are measured in the kinematic region of  $Q^2 \geq 300 \text{ GeV}^2$  and inelasticity  $y \leq 0.9$ . The measured cross sections were compared with the theory expectations and found to be in agreement with the Standard Model (SM) prediction. The total charged current cross section extrapolated to  $P_e = -1$  was found to be consistent with zero, supporting the absence of the right handed charged currents in the electroweak sector of the SM.

Part of the results obtained with the present analysis were published by the H1 Collaboration as the first polarisation dependence of the total charged current cross section measurement at HERA [13].

The results of this analysis can be further used in the following aspects:

The  $d$  quark distribution in the valence region can be constrained which is possible especially from the  $e^+p$  CC interactions at HERA in the large  $Q^2$  region. The understanding of the proton structure is

essential for future studies in the field of particle physics, for example, in studies of  $pp$  collisions at the Large Hadron Collider (LHC);

Charged current cross sections can be used to determine the mass of heavy intermediate vector boson  $W$ . Although the mass of the  $W$  presently is known with high precision [24], the space-like domain of  $W$  exchange at HERA brings an additional quality to the boson mass determination;

Together with the data presently being collected at HERA II, precise tests of the electroweak SM section can be performed (the statistical error still dominates in the present analysis). New, precise measurements can be used to constrain the physics beyond the Standard Model.

# Appendix A

## Tables of Results

In this appendix the results of the single and double differential charged current  $e^+p$  cross section measurements are given. The results of the unpolarised cross section measurement, i.e. the combination of L and R data sets are presented first, then the results of polarised cross section measurements are given.

Abbreviations used in tables:

$\delta_{stat}$	the relative statistical error
$\delta_{sys}$	the relative systematical error
$\delta_{tot}$	the relative total error
$\delta_{unc}$	the uncorrelated part of the systematic error
$\delta_{unc}^h$	the contribution of the hadronic energy error to the uncorrelated systematic error
$\delta_{cor}$	the correlated part of the systematic error
$\delta_{cor}^{V+}$	the contribution from a positive variation of one standard deviation of the vertex requirement error
$\delta_{cor}^{h+}$	the contribution from a positive variation of one standard deviation of the hadronic energy error
$\delta_{cor}^{N+}$	the contribution from a positive variation of one standard deviation of the error due to noise subtraction

$Q^2$ ( $GeV^2$ )	$d\sigma_{CC}/dQ^2$ ( $pb/GeV^2$ )	$\delta_{stat}$ (%)	$\delta_{sys}$ (%)	$\delta_{tot}$ (%)	$\delta_{unc}$ (%)	$\delta_{unc}^h$ (%)	$\delta_{cor}$ (%)	$\delta_{cor}^{V+}$ (%)	$\delta_{cor}^{h+}$ (%)	$\delta_{cor}^{N+}$ (%)
300	3.352e-02	12.08	13.75	18.31	10.53	-3.42	8.84	7.84	-1.97	-0.56
500	1.732e-02	9.71	6.76	11.84	5.76	-1.58	3.54	2.84	-0.78	0.79
1000	1.094e-02	7.60	4.23	8.70	3.85	-1.01	1.73	0.76	-0.57	0.60
2000	5.009e-03	7.23	3.16	7.89	2.88	0.31	1.31	0.41	0.40	0.39
3000	2.287e-03	8.78	4.02	9.66	3.42	2.55	2.12	0.38	1.61	0.67
5000	1.182e-03	9.72	5.77	11.30	4.83	4.35	3.16	0.42	2.66	0.75
8000	2.842e-04	16.10	10.48	19.22	9.05	8.75	5.29	0.48	4.64	1.15
15000	3.409e-05	31.17	18.71	36.35	15.44	15.21	10.55	0.50	9.55	1.57

Table A.1: The unpolarised ( $P_e = 0$ ) cross section  $d\sigma_{CC}/dQ^2$  of the combined 2003-04  $e^+p$  CC measurement for  $y < 0.9$ . The luminosity uncertainty of 1.3% is not included in the errors.

$Q^2$ ( $GeV^2$ )	$d\sigma_{CC}/dQ^2$ ( $pb/GeV^2$ )	$\delta_{stat}$ (%)	$\delta_{sys}$ (%)	$\delta_{tot}$ (%)	$\delta_{unc}$ (%)	$\delta_{unc}^h$ (%)	$\delta_{cor}$ (%)	$\delta_{cor}^{V+}$ (%)	$\delta_{cor}^{h+}$ (%)	$\delta_{cor}^{N+}$ (%)
300	2.154e-02	23.94	14.74	28.12	10.52	-3.27	9.97	7.89	-1.87	-0.46
500	7.177e-03	24.21	7.50	25.34	5.82	-1.61	3.89	2.78	-0.79	0.75
1000	5.538e-03	16.72	5.11	17.48	3.83	-1.02	2.06	0.81	0.56	0.63
2000	3.027e-03	14.39	4.23	15.00	2.94	0.23	1.43	0.40	0.31	0.41
3000	1.295e-03	17.83	4.87	18.48	3.47	2.65	2.12	0.41	1.64	0.60
5000	7.139e-04	19.22	6.41	20.26	4.92	4.44	3.13	0.43	2.68	0.73
8000	1.460e-04	34.55	10.71	36.18	8.91	8.62	5.30	0.47	4.71	1.15

Table A.2: The polarised ( $P_e = -40.2\%$ ) cross section  $d\sigma_{CC}/dQ^2$  of the left handed (L) 2003-04  $e^+p$  CC measurement for  $y < 0.9$ . The luminosity uncertainty of 1.3% is not included in the errors.

$Q^2$ ( $GeV^2$ )	$d\sigma_{CC}/dQ^2$ ( $pb/GeV^2$ )	$\delta_{stat}$ (%)	$\delta_{sys}$ (%)	$\delta_{tot}$ (%)	$\delta_{unc}$ (%)	$\delta_{unc}^h$ (%)	$\delta_{cor}$ (%)	$\delta_{cor}^{V+}$ (%)	$\delta_{cor}^{h+}$ (%)	$\delta_{cor}^{N+}$ (%)
300	4.408e-02	14.02	13.77	19.65	10.50	-3.35	8.69	7.95	-1.92	-0.50
500	2.566e-02	10.60	6.99	12.69	5.77	-1.56	3.43	2.87	-0.76	0.75
1000	1.545e-02	8.53	4.61	9.70	3.85	-0.97	1.62	0.75	-0.55	0.63
2000	6.574e-03	8.37	3.62	9.11	2.78	0.28	1.25	0.41	0.38	0.44
3000	3.074e-03	10.08	4.53	11.05	3.51	2.67	2.10	0.41	1.65	0.59
5000	1.573e-03	11.26	6.00	12.76	4.76	4.28	3.09	0.42	2.62	0.77
8000	3.980e-04	18.21	10.65	21.09	9.04	8.74	5.29	0.47	4.68	1.15
15000	3.943e-05	39.10	18.46	43.24	15.23	14.99	10.26	0.50	9.30	1.52

Table A.3: The polarised ( $P_e = 33.6\%$ ) cross section  $d\sigma_{CC}/dQ^2$  of the right handed (R) 2003-04  $e^+p$  CC measurement for  $y < 0.9$ . The luminosity uncertainty of 1.3% is not included in the errors.

$x$	$d\sigma_{CC}/dx$ (pb)	$\delta_{stat}$ (%)	$\delta_{sys}$ (%)	$\delta_{tot}$ (%)	$\delta_{unc}$ (%)	$\delta_{unc}^h$ (%)	$\delta_{cor}$ (%)	$\delta_{cor}^{V+}$ (%)	$\delta_{cor}^{h+}$ (%)	$\delta_{cor}^{N+}$ (%)
0.032	1.570e+02	9.15	3.38	9.75	2.75	0.73	1.96	0.35	0.53	0.89
0.080	8.719e+01	7.03	3.05	7.66	2.68	1.46	1.47	0.39	0.70	0.71
0.130	5.097e+01	8.32	4.36	9.39	3.87	2.62	2.01	0.47	1.56	0.35
0.250	1.434e+01	13.12	7.01	14.87	6.09	5.32	3.47	0.51	2.91	0.66
0.400	4.530e+00	28.46	14.04	31.74	11.46	11.18	8.11	0.50	6.53	-1.85

Table A.4: The unpolarised ( $P_e = 0$ ) cross section  $d\sigma_{CC}/dx$  of the combined 2003-04  $e^+p$  CC measurement for  $y < 0.9$  and  $Q^2 > 1000 \text{ GeV}^2$ . The luminosity uncertainty of 1.3% is not included in the errors.

$x$	$d\sigma_{CC}/dx$ (pb)	$\delta_{stat}$ (%)	$\delta_{sys}$ (%)	$\delta_{tot}$ (%)	$\delta_{unc}$ (%)	$\delta_{unc}^h$ (%)	$\delta_{cor}$ (%)	$\delta_{cor}^{V+}$ (%)	$\delta_{cor}^{h+}$ (%)	$\delta_{cor}^{N+}$ (%)
0.032	1.044e+02	17.36	4.51	17.94	2.87	0.68	2.23	0.35	0.46	0.80
0.080	4.004e+01	15.97	4.10	16.49	2.71	1.53	1.50	0.41	0.76	0.74
0.130	3.783e+01	14.75	5.09	15.61	3.85	2.60	1.99	0.47	1.57	0.38
0.250	7.503e+00	28.04	7.49	29.02	6.06	5.29	3.49	0.51	2.94	0.61
0.400	3.012e+00	63.89	15.86	65.83	12.65	11.86	9.17	0.50	6.79	-2.71

Table A.5: The polarised ( $P_e = -40.2\%$ ) cross section  $d\sigma_{CC}/dx$  of the left handed (L) 2003-04  $e^+p$  CC measurement for  $y < 0.9$  and  $Q^2 > 1000 \text{ GeV}^2$ . The luminosity uncertainty of 1.3% is not included in the errors.

$x$	$d\sigma_{CC}/dx$ (pb)	$\delta_{stat}$ (%)	$\delta_{sys}$ (%)	$\delta_{tot}$ (%)	$\delta_{unc}$ (%)	$\delta_{unc}^h$ (%)	$\delta_{cor}$ (%)	$\delta_{cor}^{V+}$ (%)	$\delta_{cor}^{h+}$ (%)	$\delta_{cor}^{N+}$ (%)
0.032	1.982e+02	10.75	3.72	11.38	2.63	0.66	1.77	0.39	0.48	0.82
0.080	1.241e+02	7.83	3.61	8.62	2.67	1.50	1.45	0.41	0.72	0.72
0.130	6.210e+01	10.07	4.78	11.15	3.88	2.64	2.01	0.47	1.59	0.37
0.250	2.021e+01	14.85	7.25	16.52	6.08	5.32	3.44	0.51	2.94	0.64
0.400	6.588e+00	31.70	14.34	34.79	11.62	11.37	8.17	0.50	6.79	-1.75

Table A.6: The polarised ( $P_e = 33.6\%$ ) cross section  $d\sigma_{CC}/dx$  of the right handed (R) 2003-04  $e^+p$  CC measurement for  $y < 0.9$  and  $Q^2 > 1000 \text{ GeV}^2$ . The luminosity uncertainty of 1.3% is not included in the errors.

$Q^2$	$x$	$y$	$d^2\sigma_{CC}/dx dQ^2$ (pb/GeV <sup>2</sup> )	$\tilde{\sigma}_{CC}$	$\delta_{stat}$ (%)	$\delta_{sys}$ (%)	$\delta_{tot}$ (%)	$\delta_{unc}$ (%)	$\delta_{unc}^h$ (%)	$\delta_{cor}$ (%)	$\delta_{cor}^{V+}$ (%)	$\delta_{cor}^{h+}$ (%)	$\delta_{cor}^{N+}$ (%)
300	0.013	0.227	7.052e-01	1.187	25.03	19.46	31.71	13.76	-4.12	13.76	12.89	-2.69	-0.70
300	0.032	0.092	2.065e-01	0.856	20.65	10.65	23.24	8.02	-2.92	7.01	5.56	1.38	0.78
300	0.080	0.037	7.279e-02	0.754	23.27	12.67	26.50	11.25	-2.66	5.84	2.25	-1.83	-1.97
500	0.013	0.379	4.286e-01	0.765	21.64	11.54	24.52	8.19	-1.43	8.14	7.44	1.21	0.85
500	0.032	0.154	1.607e-01	0.706	15.06	5.54	16.04	4.31	-1.92	3.48	1.63	-1.21	1.09
500	0.080	0.062	4.397e-02	0.483	17.35	7.25	18.80	6.85	-1.56	2.38	0.52	-0.38	-0.49
1000	0.013	0.757	4.261e-01	0.874	16.89	10.44	19.85	7.72	-2.86	7.03	5.92	-2.64	-0.19
1000	0.032	0.308	1.303e-01	0.657	12.14	3.35	12.59	2.47	-0.79	2.27	-0.38	0.37	0.63
1000	0.080	0.123	3.641e-02	0.459	13.27	4.91	14.15	4.36	0.83	2.25	0.46	0.90	0.92
1000	0.130	0.076	1.323e-02	0.271	28.02	7.73	29.07	6.68	-0.95	3.89	0.50	-0.87	-2.14
2000	0.032	0.615	7.907e-02	0.513	11.84	3.66	12.39	2.90	-1.08	2.23	0.50	-0.52	0.80
2000	0.080	0.246	2.574e-02	0.418	11.25	2.98	11.64	2.21	0.78	2.00	0.34	0.89	0.72
2000	0.130	0.152	1.060e-02	0.280	17.79	5.67	18.67	5.06	1.57	2.54	0.48	0.98	-0.52
2000	0.250	0.079	1.147e-03	0.058	77.63	9.62	78.22	6.62	-0.65	6.97	0.50	-1.39	-3.40
3000	0.080	0.369	1.551e-02	0.315	12.73	4.18	13.40	3.24	2.61	2.65	0.46	1.82	0.69
3000	0.130	0.227	8.263e-03	0.272	15.22	3.33	15.58	2.41	1.48	2.30	0.45	0.72	0.73
3000	0.250	0.118	1.266e-03	0.080	33.58	6.92	34.28	5.72	3.47	3.90	0.50	1.61	-1.25
5000	0.080	0.615	1.013e-02	0.301	16.07	7.19	17.61	5.99	5.62	3.98	-0.52	2.78	1.10
5000	0.130	0.379	4.908e-03	0.237	15.92	5.15	16.73	3.73	3.28	3.55	0.50	2.54	0.93
5000	0.250	0.197	1.531e-03	0.142	20.96	5.87	21.76	4.29	3.86	4.01	0.51	2.64	0.42
5000	0.400	0.123	6.727e-04	0.100	44.85	13.92	46.96	9.72	8.93	9.97	0.50	3.84	-2.62
8000	0.130	0.606	2.048e-03	0.158	22.68	11.06	25.23	9.24	9.07	6.08	0.44	4.78	1.59
8000	0.250	0.315	5.498e-04	0.081	26.51	9.09	28.02	7.35	7.13	5.36	0.50	4.02	1.11
8000	0.400	0.197	1.932e-04	0.046	44.89	15.01	47.33	10.98	10.83	10.23	0.50	7.39	-1.22

Table A.7: The unpolarised ( $P_e = 0$ ) cross section  $d^2\sigma_{CC}/dx dQ^2$  and the reduced cross section  $\tilde{\sigma}_{CC}$  of the combined 2003-04  $e^+p$  CC measurement. The luminosity uncertainty of 1.3% is not included in the errors.



$Q^2$	$x$	$y$	$d^2\sigma_{CC}/dxdQ^2$ (pb/GeV <sup>2</sup> )	$\tilde{\sigma}_{CC}$	$\delta_{stat}$ (%)	$\delta_{sys}$ (%)	$\delta_{tot}$ (%)	$\delta_{unc}$ (%)	$\delta_{unc}^h$ (%)	$\delta_{cor}$ (%)	$\delta_{cor}^{V+}$ (%)	$\delta_{cor}^{h+}$ (%)	$\delta_{cor}^{N+}$ (%)
300	0.013	0.227	7.018e-01	1.181	38.69	20.08	43.59	13.64	-3.96	14.49	13.10	-2.38	-0.29
300	0.032	0.092	1.007e-01	0.417	48.03	11.71	49.43	7.85	-2.73	8.27	5.68	1.54	0.82
300	0.080	0.037	2.719e-02	0.282	63.14	13.77	64.62	11.33	-2.64	7.34	2.28	-1.63	-1.56
500	0.013	0.379	1.241e-01	0.222	67.73	11.90	68.76	8.08	-1.47	8.31	7.30	1.04	0.70
500	0.032	0.154	5.688e-02	0.250	41.36	6.54	41.87	4.36	-1.97	4.07	1.62	-1.06	1.00
500	0.080	0.062	2.506e-02	0.275	35.66	7.69	36.48	6.82	-1.50	2.32	0.57	-0.43	-0.49
1000	0.013	0.757	1.175e-01	0.241	53.25	10.40	54.25	6.99	-2.45	7.22	5.99	-2.32	0.13
1000	0.032	0.308	8.259e-02	0.417	23.76	4.65	24.21	2.58	-0.90	2.79	-0.37	0.48	0.71
1000	0.080	0.123	1.702e-02	0.215	29.98	5.53	30.49	4.33	0.62	2.15	0.48	0.84	0.87
1000	0.130	0.076	9.489e-03	0.195	50.76	8.14	51.41	6.71	-1.01	3.75	0.50	-0.82	-2.24
2000	0.032	0.615	5.399e-02	0.350	22.24	4.79	22.75	3.11	-0.93	2.46	0.48	-0.43	0.83
2000	0.080	0.246	1.327e-02	0.215	24.21	3.95	24.53	2.19	0.62	1.90	0.35	-0.79	0.76
2000	0.130	0.152	8.458e-03	0.223	30.40	6.08	31.00	4.96	1.20	2.29	0.49	0.75	-0.41
3000	0.080	0.369	7.079e-03	0.144	28.79	5.08	29.24	3.42	2.85	2.64	0.50	1.85	0.80
3000	0.130	0.227	5.644e-03	0.186	28.09	4.23	28.41	2.42	1.50	2.21	0.44	0.89	0.63
3000	0.250	0.118	6.479e-04	0.041	71.71	7.42	72.10	5.76	3.55	3.84	0.50	1.84	-1.39
5000	0.080	0.615	4.056e-03	0.121	39.39	7.44	40.09	5.78	5.40	3.85	-0.52	2.75	0.96
5000	0.130	0.379	4.592e-03	0.222	25.19	5.85	25.86	3.94	3.51	3.40	0.50	2.46	0.92
5000	0.250	0.197	6.209e-04	0.058	50.65	6.77	51.10	4.73	4.34	4.04	0.53	2.86	0.60
5000	0.400	0.123	3.163e-04	0.047	100.00	13.06	101.55	8.36	7.47	9.67	0.50	4.25	-2.95
8000	0.130	0.606	6.941e-04	0.053	60.15	11.40	61.22	9.30	9.13	6.04	0.43	4.90	1.49
8000	0.250	0.315	4.223e-04	0.063	46.30	8.99	47.16	6.93	6.69	5.07	0.50	3.82	0.96
8000	0.400	0.197	8.970e-05	0.021	100.00	15.73	102.04	11.62	11.47	10.26	0.50	7.90	-0.99

Table A.8: The polarised ( $P_e = -40.2\%$ ) cross section  $d^2\sigma_{CC}/dxdQ^2$  and the reduced cross section  $\tilde{\sigma}_{CC}$  of the left handed (L) 2003-04  $e^+p$  CC measurement. The luminosity uncertainty of 1.3% is not included in the errors.

$Q^2$	$x$	$y$	$d^2\sigma_{CC}/dx dQ^2$ (pb/GeV <sup>2</sup> )	$\tilde{\sigma}_{CC}$	$\delta_{stat}$ (%)	$\delta_{sys}$ (%)	$\delta_{tot}$ (%)	$\delta_{unc}$ (%)	$\delta_{unc}^h$ (%)	$\delta_{cor}$ (%)	$\delta_{cor}^{V+}$ (%)	$\delta_{cor}^{h+}$ (%)	$\delta_{cor}^{N+}$ (%)
300	0.008	0.369	2.167e+00	2.245	46.19	37.36	59.41	29.96	-5.77	22.23	21.23	-3.41	-0.69
300	0.013	0.227	7.254e-01	1.221	33.27	19.51	38.57	13.74	-4.13	13.71	13.00	-2.59	-0.52
300	0.032	0.092	2.993e-01	1.240	22.84	10.67	25.21	7.98	-2.61	6.81	5.71	1.30	0.62
300	0.080	0.037	1.115e-01	1.155	24.99	12.58	27.98	11.29	-2.82	5.19	2.22	-1.88	-1.45
500	0.008	0.615	1.219e+00	1.339	56.35	24.73	61.54	18.64	-1.10	16.13	15.25	-0.21	1.81
500	0.013	0.379	6.720e-01	1.199	22.77	11.66	25.58	8.46	-1.54	7.79	7.27	-0.86	0.50
500	0.032	0.154	2.453e-01	1.078	16.16	5.68	17.13	4.27	-1.81	3.20	1.67	-1.00	1.05
500	0.080	0.062	6.065e-02	0.666	19.84	7.48	21.20	6.84	-1.56	2.32	0.55	-0.48	-0.58
1000	0.013	0.757	6.889e-01	1.412	17.79	10.76	20.79	8.01	-2.28	6.92	6.03	-2.30	0.32
1000	0.032	0.308	1.704e-01	0.860	14.09	3.75	14.58	2.46	-0.91	2.05	-0.37	0.38	0.65
1000	0.080	0.123	5.231e-02	0.660	14.78	5.20	15.67	4.33	0.71	2.12	0.47	0.81	0.85
1000	0.130	0.076	1.656e-02	0.340	33.62	7.92	34.54	6.68	-1.02	3.78	0.50	-0.69	-2.20
2000	0.032	0.615	9.805e-02	0.636	13.96	3.85	14.48	2.60	-0.79	2.07	0.51	0.31	0.88
2000	0.080	0.246	3.561e-02	0.578	12.72	3.44	13.18	2.09	0.71	1.91	0.36	-0.77	0.79
2000	0.130	0.152	1.254e-02	0.330	21.94	5.85	22.71	4.99	1.17	2.35	0.49	0.76	-0.44
2000	0.250	0.079	2.401e-03	0.122	67.50	9.57	68.18	6.61	0.68	6.65	0.50	-1.37	-3.66
3000	0.080	0.369	2.197e-02	0.445	14.18	4.78	14.97	3.51	2.91	2.61	0.49	1.81	0.78
3000	0.130	0.227	1.036e-02	0.341	18.09	3.88	18.51	2.46	1.57	2.28	0.44	0.98	0.63
3000	0.250	0.118	1.807e-03	0.115	38.00	7.41	38.72	5.94	3.89	3.98	0.50	1.95	-1.40
5000	0.080	0.615	1.486e-02	0.442	17.60	7.07	18.97	5.58	5.20	3.89	-0.55	2.77	1.07
5000	0.130	0.379	5.262e-03	0.254	20.55	5.55	21.28	3.94	3.52	3.38	0.50	2.41	0.91
5000	0.250	0.197	2.303e-03	0.214	23.01	6.18	23.83	4.32	3.90	3.97	0.52	2.70	0.55
5000	0.400	0.123	1.037e-03	0.154	50.09	13.16	51.79	8.51	7.64	9.84	0.50	3.91	-2.97
8000	0.130	0.606	3.159e-03	0.243	24.47	11.45	27.02	9.50	9.33	6.09	0.42	4.94	1.46
8000	0.250	0.315	6.580e-04	0.097	32.38	9.01	33.61	7.15	6.92	5.12	0.50	3.87	1.03
8000	0.400	0.197	2.796e-04	0.066	50.14	15.40	52.45	11.37	11.21	10.21	0.50	7.66	-1.04

Table A.9: The polarised ( $P_e = 33.6\%$ ) cross section  $d^2\sigma_{CC}/dx dQ^2$  and the reduced cross section  $\tilde{\sigma}_{CC}$  of the right handed (R) 2003-04  $e^+p$  CC measurement. The luminosity uncertainty of 1.3% is not included in the errors.

## Appendix B

# Kinematic Extrapolation Factors

In this appendix the factors ( $k_{cor}$ ) are given which estimate the influence to the single differential CC cross sections caused by enlarging the kinematic region beyond the cuts used in the CC analysis. The factors  $k_{cor}$  were calculated using the H1 PDF 2000 parametrisation.

$Q^2(GeV^2)$	300	500	1000	2000	3000	5000	8000	15000
$k_{cor}$	1.397	1.175	1.042	1.026	1.030	1.035	1.047	1.064

Table B.1: The extrapolation factor  $k_{cor}$  estimating the influence to the differential cross section  $d\sigma_{CC}/dQ^2$  due to changes from the measurement kinematic cuts  $0.03 < y < 0.85$  and  $p_{T,miss} > 12 GeV$  to  $y < 0.9$ .

$x$	0.032	0.080	0.130	0.250	0.400
$k_{cor}$	1.053	1.017	1.008	1.002	1.061

Table B.2: The extrapolation factor  $k_{cor}$  estimating the influence to the differential cross section  $d\sigma_{CC}/dx$  due to changes from the measurement kinematic cuts  $0.03 < y < 0.85$  and  $p_{T,miss} > 12 GeV$  to  $y < 0.9$  for  $Q^2 > 1000 GeV^2$ .



# Bibliography

- [1] E. Rutherford. *The Scattering of  $\alpha$  and  $\beta$  Particles of Matter and the Structure of the Atom*, Phil. Mag., 21:669, 1911
- [2] E.D. Bloom. *Proceedings of the 6th International Symposium on Electron and Photon Interactions at High Energies*, edited by H. Rollnik and W. Pfeil, North Holland Publishing Co., Amsterdam, 227 p, 1974
- [3] E.D. Bloom et al. Phys. Rev. Lett. 23, 930, 1969
- [4] M. Breitenbach et al. Phys. Rev. Lett. 23, 935, 1969
- [5] J.D. Bjorken. Phys. Rev. 179, 1547, 1969
- [6] R.P. Feynman. Phys. Rev. 23, 1417, 1969
- [7] E. Fermi, *Attempt at a Theory of Beta-Rays*, Il Nuovo Cimento 11: 1-21 p, 1934
- [8] S.L. Glashow. Nucl. Phys. 22, 579, 1961
- [9] S. Weinberg. Phys. Rev. Lett. 19, 1264, 1967
- [10] A. Salam. *Elementary Particle Physics*, Proc. 8th Nobel Symp., eds. Stockholm, 367 p, 1968
- [11] UA1 Collaboration.  
G. Arnison et al., Phys. Lett. B 122, 103, 1983  
M. Banner et al., Phys. Lett. B 122, 476, 1983
- [12] UA1 Collaboration.  
G. Arnison et al., Phys. Lett. B 126, 398, 1983  
M. Banner et al., Phys. Lett. B 129, 130, 1983
- [13] H1 Collaboration. *First Measurement of Charged Current Cross Sections at HERA with Longitudinally Polarised Positrons*, Phys. Lett. B 634, 173-179 p, 2006
- [14] I.J.R. Aitchison and A.J.G. Hey. *Gauge Theories in Particle Physics*, Adam Hilger LTD, Bristol, 333 p, 1982

- [15] C.G. Callan and D. Gross. Phys. Rev. Lett. 22, 156, 1969
- [16] D. Griffiths. *Introduction to Elementary Particles*, Harper & Row Publishers, New York, 290-294 p, 1987
- [17] A. Bodek et al. Phys. Rev. D20, 1471, 1979
- [18] C. Adloff et al. *Measurement and QCD analysis of Neutral and Charged Current Cross Sections at HERA*, Eur. Phys. J. C 30, 2003
- [19] BCDMC Collaboration, A.C. Benvenuti et al. *A High Statistics Measurement of the Proton Structure Functions  $F_2^i(x, Q^2)$  and  $R$  from Deep Inelastic Muon Scattering at High  $Q^2$* , Phys. Lett. B 223, 485 p, 1989
- [20] NMC Collaboration, M. Arneodo et al. *Measurement of the Proton and the Deuteron Structure Functions  $F_2^p$  and  $F_2^d$* , Phys. Lett. B 364, 107-115 p, 1995
- [21] D.J. Gross and F. Wilczek. Phys. Rev. Lett. 30 (26), 1343, 1973
- [22] D.J. Gross and F. Wilczek. Phys. Rev. D8 (10), 3633, 1973
- [23] G. Altarelli, G. Parisi, Nucl. Phys. B126, 298 p, 1977  
Yu. L. Dokshitzer, Sov. Phys. JETP 46, 641 p, 1977  
L.N. Lipatov, Sov. J. Nucl. Phys. 20, 94 p, 1975  
V.N. Gribov, L.N. Lipatov, Sov. J. Nucl. Phys. 15, 438,675 p, 1972
- [24] <http://pdg.lbl.gov/>
- [25] C. Kiesling, *Tests of the Standard Theory of Electroweak Interactions*, Springer Tracts in Modern Physics, Springer-Verlag Berlin Heidelberg, 1988
- [26] T.D. Lee and C.N. Yang, *Question of Parity Conservation in Weak Interactions*, Phys. Rev. 104, 254 p, 1956
- [27] C.S. Wu et al. Phys. Rev. 105, 1413 p, 1957
- [28] R.P. Feynman and M. Gell-Mann, Phys. Rev. 109, 193 p, 1958
- [29] E.C.G. Sudarshan and R.E. Marshak, Phys. Rev. 109, 1860 p, 1958
- [30] N. Cabibbo, *Unitary Symmetry and Leptonic Decays* Phys. Rev. Lett. 10, 531 p, 1963
- [31] G. Backenstoss et al, Phys. Rev. Lett. 6, 415 p, 1961
- [32] G. Buchalla. *CP Violation in Neutral Kaon Decays*, SLAC-PUB-7520, 1997, [hep-ph/9705369]

- [33] H. Yukawa. Proc. Phys.-Math. Soc. Japan, 17, 48 p, 1935
- [34] S.A. Bludman. Nuovo Cimento 9, 443 p, 1958
- [35] F.J. Hasert and al. Phys. Lett. 46B, 138 p, 1973 and Nucl. Phys. B73, 1 p, 1973
- [36] P.W. Higgs. Phys. Rev. Lett. 12, 132 p, 1965 and Phys. Rev. 145, 1156 p, 1966
- [37] A. Arbuzov et al. Comput. Phys. Commun. 94, 128 p, 1996 [hep-ph/9511434]
- [38] M. Klein and T. Riemann. *Electroweak Interactions Probing the Nucleon Structure*, Z. Phys. C - Particles and Fields 24, 1551-155 p, 1984
- [39] H. Spiesberger et al. *Radiative Corrections at HERA*, In W. Buchmüller and G. Ingelman, Proceedings of the Workshop: Physics at HERA , volume 2, 798-839 p, DESY, 1992
- [40] B. Heinemann, S. Riess, H. Spiesberger. *Radiative Corrections for Charged Current Scattering: A Comparison of Computer Codes*, published in the Proceedings of the Workshop Monte Carlo Generators for HERA Physics, DESY, Hamburg 1998/99, MZ-TH/99-29.
- [41] D. Bardin, C. Burdick, C. Christova and T. Riemann, Z. Phys. C 44, 149 p, 1989
- [42] H. Spiesberger, Nucl. Phys. B 349, 109 p, 1991
- [43] A. M. Copper-Sarkar et al. in *Proc. 3rd UK Phenomenology Workshop on HERA Physics*, Durham, England, 20-25 Sep 1998
- [44] U. Baur, J.A. Vermaseren, D. Zeppenfeld. *Electroweak Vector Boson Production in High-Energy ep Collision*, Nucl. Phys. B 735, 3 p, 1992
- [45] S. Caron. *Jets in Photoproduction at HERA*, PhD thesis, RWTH Aachen, 2002
- [46] G. Gustafson. *Dual Description of a Confined Color Field*, Phys. Lett. B 453, 175 p, 1986
- [47] B. Andersson et al. *Parton Fragmentation and String Dynamics*, Phys. Rept. 31, 97 p, 1983
- [48] G.A. Schuler, H. Spilberger. Proceedings of the Workshop *Physics at HERA*, vol. 3, eds. W. Buchmüller, G. Ingelman. DESY, 1419, 1992
- [49] G. Ingelman. Proceedings of the Workshop *Physics at HERA*, vol. 3, eds. W. Buchmüller, G. Ingelman. DESY, 1366, 1992

- [50] A. Kwiatkowski, H. Spiesberger, H.-J. Möhring. *Comput. Phys. Commun.*, 69, 155 p, 1992
- [51] L. Lönnbald. *Comput. Phys. Commun.*, 71 15 p, 1992
- [52] T. Sjöstrand, M. Bengtsson. *Comput. Phys. Commun.*, 43, 367 p, 1987
- [53] A.D. Martin, W.J. Stirling, R.G. Roberts. *Phys. Lett. B* 306, 145 p, 1993
- [54] T. Sjöstrand. *Comput. Phys. Commun.*, 82, 74 p, 1994
- [55] H.L. Lai et al. [CTEQ Collaboration], *Eur. Phys. J. C* 12, 375 p, 2000
- [56] M. Glück, E. Reya, A. Vogt. *Phys. Rev. D* 46, 1973 p, 1992
- [57] T. Abe. *Comput. Phys. Commun.*, 136, 126 p, 2001
- [58] M. Peters, *Die Parametrisierte Simulation Elektromagnetischer Schauer*, Dissertation, MPI München, 1992
- [59] J. Meyer, *Guide for the H1 Simulation Program H1SIM*, Internal Software-Note 03-11/89, DESY, 1989
- [60] R. Brun et al. *GEANT3 User's Guid*, CERN-DD/EE-84-1, 1987
- [61] I. Abt et al. *The Tracking, Calorimeter and Muon Detectors of the H1 Experiment at HERA*, *Nucl. Instr. Meth. A* 386, 348-396 p, 1997
- [62] The ZEUS Detector, *Status Report (1993)*, DESY 1993
- [63] HERMES collaboration, *HERMES technical design report*. DESY-PRC-93-06, 1993
- [64] E. Hartouni et al. *An Experiment to Study CP Violation in the B System Using an Internal Target at the HERA Proton Ring*, Design report. DESY-PRC-95-01, 1995
- [65] A.A. Sokolov, I.M. Ternov, V.V. Mikhailin. *Izv. Vuz. Fiz.* 4, 7 p, 1976
- [66] G.Z.M. Berglund. *Spin-Orbit Maps and Electron Spin Dynamics for the Luminosity Upgrade Project at HERA*, Ph.D. Thesis, Alfvén Laboratory, Stockholm, 2001
- [67] D.P. Barber, H. Mais, G. Ripken, R. Rossmanith. *DESY Report* 85-044, 1985
- [68] D.P. Barber et al. *Nucl. Instr. Meth. A* 338, 166 p, 1994



- [69] F. Zomer. *A High Power Fabry-Pérot Resonator for Compton Polarimetry with the Longitudinally Polarised Lepton Beams at HERA*, Ph.D. Thesis, Orsay, 2003
- [70] H.A. Tolhoek. *Rev. Mod. Phys.* 28, 277 p, 1956
- [71] J. Böhme. *Precision Measurement with the Transverse Polarimeter at HERA II*, *Eur. Phys. J. C.* 33, s1067-s1069 p, 2004
- [72] M. Beckmann et al. *The Longitudinal Polarimeter at HERA*, *Nucl. Instr. Meth. A* 479, 334 p, 2002 [arXiv:physics/0009047]
- [73] Z. Zhang. *Electron Polarisation Measurement Using a Fabry-Pérot Cavity at HERA*, *Proceedings the 2001 HEP*, [hep-ex/0201033]
- [74] W. Lorenzon [HERMES Collaboration]. *7th International Workshop on Polarized Gas Targets and Polarized Beams*, DESY-HERMES-97-68, Urbana, IL, 18-22 p, 1997;  
F. Crriveau et al. [TPOL Polarimeter Group]. *A Calibration of the HERA Transverse Polarimeter for the 2003/2004 Data*, available at <http://www.desy.de/pol2000/documents/documents.html>.
- [75] M. Beckmann et al. *The Longitudinal Polarimeter at HERA*, *Nucl.Instrum.Meth. A* 479, 334-348 p, 2002
- [76] I. Abt et al. *The H1 Detector at Hera*, *Nucl. Instr. Meth., A* 386, 310 p, 1997
- [77] L. Favart et al. *Proposal for Installation of a Very Forward Proton Spectrometer in H1 after 2000*, H1-internal note H1-05/00-582, 2000
- [78] P. Van Eshch et al. *The H1 Forward Proton Spectrometer at HERA*, *Nucl. Instr. Meth., A* 446, 409 p, 2000
- [79] B. List. *Diffraktive J/Psi Produktion in Elektron-Proton-Stößen am Speicherring HERA*, H1-internal note H1-10/93-319, 1993
- [80] W. Brueckner et al. *Upgrade of the H1 Forward Neutron Calorimeter*, H1-internal note H1-11/99-578, 1999
- [81] S. Lueders. *CST/CIP<sub>2000</sub> Stand-Alone Tracking and Vertexing*, H1-internal note H1-04/99-570, 1999
- [82] H1 Collaboration, *Proposal to Upgrade the H1 Forward Track Detector*, Proposal 750, March 1998
- [83] D. Pitzl et al. *The H1 silicon vertex detector*, *Nucl. Instrum. Meth. A* 454, 334-349 p, 2000

- [84] H. Abramowich et al. Nucl. Instrum. Meth. A 180, 429p, 1981
- [85] B. Andrieu et al. *Beam Tests and Calibration of the H1 Liquid Argon Calorimeter with Electrons*, Nucl. Instrum. Meth. A 350, 57-72 p, 1994
- [86] B. Andrieu et al. *Results from Pion Calibration Runs for the H1 Liquid Argon Calorimeter and Comparisons with Simulations*, Nucl. Instrum. Meth. A 336, 499-509 p, 1993
- [87] T. Carli, T. Jansen, C. Kiesling, J.H. Köhne, H. Rick, K. Rueter. *Performance of the H1 Lar Trigger in 1994*, H1-internal note H1-07/95-445
- [88] B. Reisert. *Elektron-Proton-Streuung bei hohen Impulsüberträgen am H1-Experiment bei HERA*, Dissertation. LMU München, 2000
- [89] M. Peez, B. Pothault and E. Sauvan. *An Energy Flow Algorithm for Hadronic Reconstruction in OO: Hadroo2*, H1-internal note H1-01/05-616, 2005
- [90] R.-D. Appuhn et al. *The H1 Lead/Scintillating-Fibre Calorimeter*, Technical report DESY-96-171, DESY, 1996
- [91] D. Reyna, *Modifications to SpaCal for H1 High Luminosity Operation and the Effect on Acceptance*, H1-internal note H1-11/98-555, 1998
- [92] H. Bethe and W. Heitler. *On the Stopping of Fast Particles and on the Creation of Positive Electrons*, Proc. Roy. Soc. Lond. A 146, 83-112 p, 1934
- [93] L. Favart and R. Maraček, *H1 1994 Integrated Luminosity Measurement Using Bremsstrahlung Overlapping Events and Quasi-Real Compton Events*, H1-internal note H1-11/96-503, 1996
- [94] Ch. Wissing et al. *The H1 ToF System in 1996 and 1997*, H1-internal note H1-01/98-533, 1998
- [95] S.A. Baird et al. *Addendum to the Proposal "A Fast Track Trigger with High Resolution for H1"*, H1-internal note H1-09/99-576, 1999
- [96] S.A. Baird et al. *A Fast Track Trigger with High Resolution for H1*, H1-internal note H1-06/99-573, 1999
- [97] M. Ch. Urban, *The new CIP2k z-Vertex Trigger for the H1 Experiment at HERA*, Dissertation, Zürich 2004
- [98] M. Nedden, B. Reisert and T. Schörner, *H1 Liquid Argon Trigger: Overview, Simulation and Performance*, H1-internal note H1-04/01-592, 2001

- [99] C. Kiesling et al. *The H1 Neural Network Trigger*, Preprints submitted to Elsevier Preprint, AIHENP 99, Crete, Greece.
- [100] C. Beigbeder et al. *Level 2 Topological Trigger (L2TT) Hardware*, H1-internal note H1-07/98-547, 1998
- [101] K. Müller, R. Beyer. *1996 L4 Filter Farm Selection Algorithm*, H1-internal note H1-10/96-499, 1996
- [102] L. Janaushek. *Elastic Photoproduction of J/psi Vector Mesons at High Photon-Proton Centre-of-Mass Energy at the H1 Experiment at HERA*, Ph.D. Thesis, LMU München, 2004
- [103] J. Zimmermann. *Statistical Learning in High Energy and Astrophysics*, Ph.D. Thesis, LMU München, 2005
- [104] M. Caudill and C. Butler. *Naturally intelligent systems*, Cambridge, Mass. MIT Press, 1990.
- [105] D.E. Rumelhart et al. *Learning Representations by the Back-Propagating Errors*, Nature, 323:533, 1986
- [106] CNAPS Release Notes 2.0, Adaptive Solutions, Inc., Beaverton Or., 1993
- [107] R. Hecht-Nielsen. *Kolmogorov's mapping neural network existence theorem*, In IEEE, First Annual Int. Conf. on Neural Networks, pages paper III, 11, 1987.
- [108] J. Fent et al. *A Neural Network Second Level Trigger for the H1-Experiment at HERA*, H1-internal note H1-10/95-457, 1995
- [109] J.A.M. Vermaseren. Nucl. Phys. B 229, 347 p, 1983
- [110] T. Kon, T. Kobayashi and S. Kitamura. Phys. Lett. B 376, 227 p, 1996 [hep-ph/9601338]
- [111] H. Fritzsche and D. Holtmannspötter. Phys. Lett. B 457, 186 p, 1999 [hep-ph/9901411]
- [112] A. Blondel and F. Jacquet. Proc. of the *Study of an ep Facility for Europe*, U. Amaldi, DESY 79/48, 391 p, 1971
- [113] U. Bassler and G. Bernardi. Nucl. Instr. and Meth. A361, 197 p, 1995.
- [114] A. Dubak, *Measurement of the  $e^+p$  Neutral Current DIS Cross Sections and  $F_2$ ,  $F_L$ ,  $xF_3$  Structure Functions in the H1 Experiment at HERA*, Ph.D. Thesis, LMU München, 2003

- [115] A. Nikiforov. Ph.D. Thesis (in preparation), LMU München, 2006
- [116] M. Jacquet, Z. Zhang et al. *Absolute Hadronic Jet Calibration of the H1 Liquid Argon Calorimeter*, H1-internal note H1-04/99-571, 1999
- [117] F. Keil. *Dijet Production in Charged and Neutral Current  $e^+p$  Interactions at High  $Q^2$  at HERA*, Ph.D. Thesis, Heidelberg, 2001
- [118] K. Rüter. *Untersuchung des Schwachen Geladenen Stroms in Tiefeinelastischen Positron-Proton Kollisionen mit dem H1-Detektor am HERA-Speicherring*, Dissertation, LMU München, 1996
- [119] C. Adloff et al. *Measurement and QCD analysis of Neutral and Charged Current Cross Sections in Positron-Proton Collisions at Large Momentum Transfer*, Eur. Phys. J. C 13, 2000
- [120] A. Aktas. *Messung von Polarisierten Wirkungsquerschnitten des Geladenen Stromes bei HERA*, Dissertation, Universität Hamburg, 2005
- [121] P. Bruel. *Recherche d'interactions au-dela du Modele Standard a HERA*, Ph.D. Thesis, Univ. Paris XI, 1998
- [122] The H1 OO Group. *The H1 OO Physics Analysis Project*, Version 2.8.13, 2005. <https://www-h1.desy.de/icas/oop/current/oo/>
- [123] I. Negri et al. *A Minimal Comprehensive set of Muon Background Topological Finders for High  $p_t$  Physics Analysis*, H1-internal note H1-10/96-498, 1996
- [124] E. Chabert et al. *Qbgfmar: An Updated Phan Package for Cosmic and Halo Muon Topological Rejection in High  $p_t$  Physics Analysis*, H1-internal note H1-11/98-556, 1998
- [125] Ch. Veelken. *H1 non-ep Background Finder - Rejection of Cosmic Muon and Beam-Halo Events in the H1OO Framework*, H1-internal note H1-09/02-603, 2003
- [126] B. Heinemann. *Measurement of Charged Current and Neutral Current Cross Sections in Positron-Proton Collisions at  $\sqrt{s} \simeq 300$  GeV*, Ph.D. Thesis, Hamburg, 1999
- [127] <https://h1web01.desy.de/icgi-h1wiki/moin.cgi/GerhardBrandt/LarTiming>
- [128] H1 Collab., A. Aktas et al. *A General Search for New Phenomena in ep Scattering at HERA*, Phys. Lett. B 602, 14-30 p, 2004
- [129] B. Portheault, Z. Zhang. *Radiative Corrections for Charged Current Process at HERA Revisited*, H1-internal note H1-11/04-614, 2004

- 
- [130] G.J. Feldman and R.D. Cousins. Phys. Rev. D 57, 3873, 1998 [physics/9711021]
- [131] ZEUS Collaboration. *Measurement of High- $Q^2$  Deep Inelastic Scattering Cross Sections with a Longitudinally Polarised Positron Beam at HERA*, DESY-06-015, 2006, [hep-ex/0602026]
- [132] B. Reiser, *H1 Inclusive Cross-Section Measurements and an Extraction of Parton Distribution Functions*, Mod. Phys. Lett. A20, 21, 1557-1571 p, 2005



# Acknowledgements

The work presented in this thesis is the result of collaborative efforts of many people I am thankful to. Particularly I would like to thank following people:

My supervisor Prof. Dr. Christian Kiesling, who has encouraged me and gave the possibility to work in the H1 group at the Max-Planck-Institut für Physik. I'm very thankful to him for many hours of patient teaching and advising in various physics questions, for the optimistic atmosphere and his concern of students regarding physics and non physics topics;

Vladimir Chekelian for continuous interest, professional experience and helpfulness in solving many analysis problems. I am sincerely grateful to him for help in settling the "vertex problem", for careful reading and making very important comments to this thesis;

Eram Rizvi, Zhiqing Zhang, Emmanuel Sauvan and other members of the ELAN group for advice and discussions of various analysis aspects;

Adil Aktas for sharing with me the knowledge in both analysis and programming skills;

I would like to express my sympathies to all other members of the H1 MPI group:

Biljana Antunović, Juraj Bracinik (thanks for the excellent tea), Ana Dubak, Günter Grindhammer, Ludger Janauschek, Andrej Liptaj, Andrei Nikiforov, Bob Olivier, Manuel Paz Arribas, Zuzana Rurikova and Jens Zimmermann. Special thanks go to Biljana for discussions, jokes and many other things we shared (including the office) in the last three years and during the most stressful PhD phases;

I am also indebted to Burkard Reisert for his support, help in treating PDF's, reading this thesis and for his useful comments;

I am owing special thanks to my best friends:

Alesia, with whom I shared all troubles and good times in the past years, inestimable friendship and for constant trials to involve me in other activities besides work;

Andrei for continuous help, for teaching me useful programming "tricks", patience, encourage and much more than that.

Aš labai dekinga savo tėvams, broliams ir draugams už palaikymą bei supratimą.